12-2020

Numerical Simulations of Directed Self-Assembly Methods in Di-block Copolymer Films for Efficient Manufacturing of Nanoscale Patterns with Long-Range Order

Joseph Hill
University of Arkansas, Fayetteville

Numerical Simulations of Directed Self-Assembly Methods in Di-block Copolymer Films for
Efficient Manufacturing of Nanoscale Patterns with Long-Range Order

A dissertation submitted in partial fullfillment
of the requirements for the degree of
Doctor of Philosophy in Engineering

by

Joseph Hill
Brigham Young University–Idaho
Bachelor of Science in Physics, 2013

December 2020
University of Arkansas

This dissertation is approved for recommendation to the Graduate Council.

_____
Paul Millett, PhD
Dissertation Director

_____
Min Zou, PhD
Committee Member

_____
Jim Leylek, PhD
Committee Member

_____
Arun Nair, PhD
Committee Member

_____
Brian Berry, PhD
Ex Officio Committee Member

Abstract

Directed self-assembly (DSA) of block copolymers (BCPs) has been shown as a viable method to achieve bulk fabrication of surface patterns with feature sizes smaller than those available through traditional photolithography. Under appropriate thermodynamic conditions, BCPs will self-assemble into ordered micro-domain morphologies, a desirable feature for many applications. One of the primary interests in this field of research is the application of thin-film BCPs to existing photolithography techniques. This "bottom-up" approach utilizes the self-assembled BCP nanostructures as a sacrificial templating layer in the lithographic process.

While self-assembly occurs spontaneously, extending orientational uniformity over centimeter-length scales remains a critical challenge. A number of DSA techniques have been developed to enhance the long range order in an evolving BCP system during micro-phase separation. Of primary interest to this dissertation is the synergistic behavior between chemoepitaxial templating and cold-zone annealing. The first method involves pre-treating a substrate with chemical boundaries that will attract or repel one of the monomer blocks before application of the thin-film via spin-coating. The second method applies a mobile, thermal gradient to induce micro-phase separation in a narrow region within the homogeneous thin-film .

Parametric studies have been performed to characterize the extent of long range order and defect densities obtained by applying various thermal zone velocities and template patterns. These simulations are performed by utilizing a Time-Dependent Ginzburg-Landau (TDGL) model and an optimized phase field (OPF) model. Parallel processing is implemented to allow large-scale simulations to be performed within a reasonable time period.

Acknowledgements

This dissertation has become a reality only through the support of many people who have stood beside and behind me throughout the process. I would like to personally thank each and every person who has supported me, but the list is extensive and I wish to keep these comments brief.

I want to thank my wife, Meagan, for her endless support, sleepless nights, sacrifices, and encouragement. This chapter of our journey together has been both difficult and rewarding, and I look forward to the next one. To our children Rowan, John, and Allie, I want to thank you for your love, support, and understanding.

I would also like to thank my advisor, Dr. Paul Millett for his support and for working with me to make this project happen.

Contents

Appendix

Supplemental Information for Paper 1: Numerical Simulations of Directed Self-Assembly in Diblock Copolymer Films using Zone Annealing and Pattern Templating

List of Published Papers

CHAPTER 4: Joseph D Hill and Paul C Millett. Numerical simulations of directed self-assembly in diblock copolymer films using zone annealing and pattern templating. *Scientific Reports*, 7(1):5250, 2017.

CHAPTER 5: Joseph D Hill and Paul C Millett. Directed self-assembly in diblock copolymer thin films for uniform hemisphere pattern formation. *Macromolecules*, 52(24):9495-9503, 2019.

Chapter 1

Introduction

1.1 Motivation

The fabrication of semiconductors has been dominated by the process of optical lithography for over 50 years [1]. This process involves passing light through a pre-patterned mask and focusing it with a series of lenses to reduce feature sizes in order to expose a photosensitive material, called a photoresist, as a means of creating an etchable surface pattern in preparation for deposition of a new material to be patterned. Over the life-span of optical lithography, the basic process has remained the same while technologies and applications have evolved to reduce costs, processing time, and feature sizes. Over the past decade, the semiconductor industry has come closer and closer to reaching the physical limits of optical lithography.

The primary limitation in the resolution depends on the wavelength of light, the materials, and the lens design used in the process. Together these limitations determine the minimum feature width attainable, also known as the critical dimension, CD, which is ideally minimized.

$$CD \approx \frac{k_1 \lambda}{NA} \qquad (1.1)$$

The process dependent parameter, k_1, describes the ability of the photoresist to accurately develop when exposed to light. Theoretically, k_1 has a lower limit of 0.25 [2, 3], in practice however, k_1 has a practical range of $0.3 < k_1 < 1$ [1]. The wavelength of the light source, λ has two limitations; the photoresist must be receptive to the light it is exposed to, and the wavelength must be small enough that diffraction does not obfuscate the pattern as light passes through the mask. Traditional lithography methods are currently limited to wavelengths of $\lambda = 193nm$ and larger [4]. The numerical aperture, NA, is a dimensionless number that characterizes the viable angles where light can be accepted by the lens system

used. This value is determined by

$$NA = n \cdot sin(\mu) \tag{1.2}$$

where n is the index of refraction for the imaging medium, which is typically air with $n = 1.0003$ though some systems require a vacuum. The angle μ is one-half the angular aperture whose maximum value is 90°, though in practice is usually limited to $\mu \approx 80°$ or less.

The three factors in the critical dimension have all been pushed to their theoretical limits. In order to keep up with the ever-increasing industry needs for reduced costs, smaller feature resolution, and faster processing times, new methods have emerged to either modify or replace optical lithography [5]. Methods currently in use or under development include extreme ultraviolet lithography, nano-imprinting, mask-less lithography, and directed self-assembly (DSA) of block copolymers (BCPs) [6–11]. Extreme ultraviolet lithography [4, 12, 13] is similar to traditional photolithography where functional photoresists for wavelengths of $\lambda = 13nm$ have been achieved. Nanoimprinting [14–16] creates nanoscale patterns by mechanical deformation of a resist surface by pressing it with an engraved surface. Mask-less lithography [17–20] (sometimes referred to as Laser Direct Imaging or as e-Beam Lithography) employs methods which transfer pattern information directly to a photoresist without utilizing a static mask. This is accomplished through use of a focused beam (typically laser or electron-beam) which exposes the photoresist in either a raster scan manner or by a vector drawing method. Directed self-assembly is the enhancement of optical lithography by the application of self-assembling BCP materials. This enrichment extends manufacturing control down to the molecular scale and relies on the resolution of the self-assembling materials rather than the resolution capabilities of the lithography tools [21–24].

Block copolymers are a distinct type of copolymer system where chains of distinct monomers are bonded together to form a single chain of segregated monomer types. Dur-

ing annealing, polymer chains shift and reorganize with respect to one another in order to minimize the free energy of the system. For BCPs consisting of immiscible polymer types, enthalpic contributions to the free energy are significant enough to result in phase separation where the free energy is minimized as polymer blocks are allowed to separate into distinct polymer phases. Due to the covalent bonding between the blocks, the phase separation distance is significantly limited to micro-scale dimensions. This restricted separation, referred to as micro-phase separation, will cause a number of possible morphologies to spontaneously form within the BCP system. Most commonly studied are linear diblock copolymers which consist of two distinct monomer types arranged in a linear block-formation. Depending on the ratio of chain lengths, potential morphologies include alternating lamella (thin layers) of type A and type B, gyroids consisting of an infinitely interconnected minority polymer surface surrounded by the majority monomer, cylinders of the minority polymer surrounded by the majority monomer, and minority type spheres surrounded by the majority monomer type. These predictable nanoscale morphologies are the basis for copolymer lithography.

Experimental and theoretical studies have been used to extensively characterize BCP systems. The micro-phase separation of BCP thin films has been broadly studied and shown to be useful for surface patterning and membrane applications [25]. These formations, while periodic, are prone to defects such as grain boundaries, dislocations, and disclinations shown in two dimensions in Fig. 1.1 that detract from their utility in some applications. A variety of

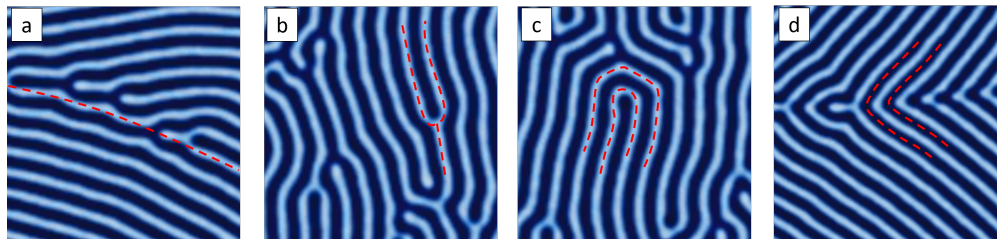Figure 1.1: Defects in phase separated morphology can detract from the intended applications. Common defects include: (a) Grain boundaries, where orientation is misaligned on either side of the boundary, (b) dislocations, where a single stripe terminates or bifurcates, and disclinations, where a single stripe (c) terminates or (d) bifurcates causing all other stripes nearby to curve around the defect

strategies have been developed to extend defect-free uniformity during self-assembly including solvent annealing [26], shear alignment [27], epitaxial templating [28–31], zone casting [32], and field alignment [33–37]. While these methods have been well studied experimentally, there is room for optimization of these techniques through parametric computational studies.

Block copolymers are an ideal system for fundamental research associated with molecular self-assembly. As such, numerical modeling has contributed significantly to the current understanding of BCP behavior. A variety of methods are used in computational studies. Atomistic simulations [38] track the position of individual atoms or monomers but are limited in length and time scales by availability of computational power. The most commonly implemented models include self-consistent field theory [39–41] (SCFT) and phase field models. A number of different phase field models have been developed for BCP research. These models include dynamic density functional theory [42] (DDFT), time-dependent Ginzburg-Landau [43, 44] (TDGL) theory, and Ohta-Kawasaki [45] (OK) theory. These phase field models use a Cahn-Hilliard equation to model diffusive phase separation of a binary system and assume a functional free-energy which approximates the behavior of a phase-separating BCP system. This approximation of free-energy allows for fast simulation times compared to atomistic simulations. SCFT uses a field-theoretic Hamiltonian derived from equilibrium properties modeled by Monte Carlo or Complex Langevin simulations [46]. While SCFT is highly accurate, it is also computationally expensive.

The primary interest of this dissertation is to computationally study a combination of chemoepitaxial templating and cold-zone annealing DSA methods applied to BCP thin films for pattern formation.

1.2 Dissertation Objectives

The objective of this dissertation is to numerically study and predict the behaviors of linear diblock copolymer systems using large scale numerical modeling. Multiple phase field methods are used to simulate these systems. Directed self-assembly techniques are

implemented within the simulations to elucidate the enhanced behavior of these copolymer systems under various conditions. Post-processing analysis algorithms have been developed and applied to simulation results in order to quantify defect density and long-range ordering within processed results. The specific research objectives are:

1. Predict the orientation of lamellae forming BCPs as a function of CZA zone velocity.

2. Predict the defect density of lamellae forming BCPs as a function of CZA zone velocity.

3. Determine how effective the addition of epitaxial templating is at improving the results from objectives 1 and 2.

4. Determine how the sharpness of the thermal gradient will affect the results from objectives 1 and 2.

5. Predict the behavior of sphere forming BCPs in 3-dimensional thin films where hemisphere formation occurs at the upper and lower surfaces.

6. Determine ideal film thickness for BCP films from objective 5.

7. Predict thin-film evolution behavior for BCP films from objective 6 after application of chemoepitaxial templating on the lower substrate.

8. Predict thin-film evolution behavior for BCP films from objective 6 during application of CZA throughout the film.

9. Predict the long-range behavior of BCP thin-films from objective 6 using a combination of chemoepitaxial templating and CZA methods.

1.3 Dissertation Structure

This dissertation is separated into six chapters and one appendix. Chapter 2 contains a literature review and background information related to block-copolymer materials, their application to photolighography, and directed self-assembly techniques applied to the lithography process. Chapter 3 details the computational methods used in this research. Chapters 4 and 5 are published articles which discuss the phase-separation of block-copolymers under directed self-assembly methods including topographical templating and cold-zone annealing. Chapter 6 discusses the key results and conclusions of this work as well as some potential future work based on these results. Appendix 1 contains published supplemental information for the published work in Chapter 4. The first article (Chapter 4), titled "Numerical Simulations of Directed Self-Assembly in Diblock Copolymer Films using Zone Annealing and Pattern Templating" was published in *Scientific Reports* in 2017. The second article (Chapter 5), titled "Directed Self-Assembly in Diblock Copolymer Thin Films for Uniform Hemisphere Pattern Formation" was published in *Macromolecules* in 2019.

Bibliography

[1] John H Bruning. Optical lithography: 40 years and holding. In *Optical Microlithography XX*, volume 6520, page 652004. International Society for Optics and Photonics, 2007.

[2] S Sivakumar. Lithography challenges for 32nm technologies and beyond. In *2006 International Electron Devices Meeting*, pages 1–4. IEEE, 2006.

[3] R Fabian Pease and Stephen Y Chou. Lithography and other patterning techniques for future electronics. *Proceedings of the IEEE*, 96(2):248–270, 2008.

[4] David B Miller, Adam M Jones, and Robert R McLeod. Super-resolution critical dimension limits of positive tone i-line photoresists. In *Advanced Fabrication Technologies for Micro/Nano Optics and Photonics XI*, volume 10544, page 105440N. International Society for Optics and Photonics, 2018.

[5] Mark Neisser. Patterning roadmap: 2017 prospects. *Advanced Optical Technologies*, 6 (3-4):143–148, 2017.

[6] Wai-kin Li and Sam Yang. Creation of sub-20-nm contact using diblock copolymer on a 300 mm wafer for complementary metal oxide semiconductor applications. *Journal of Vacuum Science & Technology B: Microelectronics and Nanometer Structures Processing, Measurement, and Phenomena*, 25(6):1982–1984, 2007.

[7] Hui Joon Park, Myung-Gyu Kang, and L Jay Guo. Large area high density sub-20 nm sio2 nanostructures fabricated by block copolymer template for nanoimprint lithography. *ACS Nano*, 3(9):2601–2608, 2009.

[8] Christopher Harrison, Miri Park, Paul M Chaikin, Richard A Register, and Douglas H Adamson. Lithography with a pattern of block copolymer microdomains as a positive or negative resist. In *ACS Symposium Series*, volume 706, pages 2–11. American Chemical Society, 1998.

[9] Mathieu Salaun, Marc Zelsmann, Sophie Archambault, Dipu Borah, Nikolaos Kehagias, Claudia Simao, Olivier Lorret, Matthew T Shaw, Clivia M Sotomayor Torres, and Mickael A Morris. Fabrication of highly ordered sub-20 nm silicon nanopillars by block copolymer lithography combined with resist design. *Journal of Materials Chemistry C*, 1(22):3544–3550, 2013.

[10] Mark P Stoykovich, Huiman Kang, Kostas Ch Daoulas, Guoliang Liu, Chi-Chun Liu, Juan J de Pablo, Marcus Müller, and Paul F Nealey. Directed self-assembly of block copolymers for nanolithography: fabrication of isolated features and essential integrated circuit geometries. *ACS Nano*, 1(3):168–175, 2007.

[11] Thomas Thurn-Albrecht, Rachel Steiner, Jason DeRouchey, Christopher M Stafford, Elbert Huang, Mustafa Bal, Mark Tuominen, Craig J Hawker, Thomas P Russell, et al.

Nanoscopic templates from oriented block copolymer films. *Advanced Materials*, 12(11): 787–791, 2000.

[12] Charles W Gwyn, R Stulen, D Sweeney, and D Attwood. Extreme ultraviolet lithography. *Journal of Vacuum Science & Technology B: Microelectronics and Nanometer Structures Processing, Measurement, and Phenomena*, 16(6):3142–3149, 1998.

[13] Xu Ma, Zhiqiang Wang, Xuanbo Chen, Yanqiu Li, and Gonzalo R Arce. Gradient-based source mask optimization for extreme ultraviolet lithography. *IEEE Transactions on Computational Imaging*, 5(1):120–135, 2019.

[14] Stephen Y Chou, Peter R Krauss, and Preston J Renstrom. Nanoimprint lithography. *Journal of Vacuum Science & Technology B: Microelectronics and Nanometer Structures Processing, Measurement, and Phenomena*, 14(6):4129–4133, 1996.

[15] Nazrin Kooy, Khairudin Mohamed, Lee Tze Pin, and Ooi Su Guan. A review of roll-to-roll nanoimprint lithography. *Nanoscale Research Letters*, 9(1):320, 2014.

[16] Ashish Pandey, Sivan Tzadka, Dor Yehuda, and Mark Schvartzman. Soft thermal nanoimprint with a 10 nm feature size. *Soft Matter*, 2019.

[17] Rajesh Menon, Amil Patel, Dario Gil, and Henry I Smith. Maskless lithography. *Materials Today*, 8(2):26–33, 2005.

[18] J Koch, E Fadeeva, M Engelbrecht, C Ruffert, HH Gatzen, A Ostendorf, and BN Chichkov. Maskless nonlinear lithography with femtosecond laser pulses. *Applied Physics A*, 82(1):23–26, 2006.

[19] TR Groves and RA Kendall. Distributed, multiple variable shaped electron beam column for high throughput maskless lithography. *Journal of Vacuum Science & Technology B: Microelectronics and Nanometer Structures Processing, Measurement, and Phenomena*, 16(6):3168–3173, 1998.

[20] Sommawan Khumpuang and Shiro Hara. A mosfet fabrication using a maskless lithography system in clean-localized environment of minimal fab. *IEEE Transactions on Semiconductor Manufacturing*, 28(3):393–398, 2015.

[21] Ricardo Ruiz, Huiman Kang, François A Detcheverry, Elizabeth Dobisz, Dan S Kercher, Thomas R Albrecht, Juan J de Pablo, and Paul F Nealey. Density multiplication and improved lithography by directed block copolymer assembly. *Science*, 321(5891):936–939, 2008.

[22] Hanqiong Hu, Manesh Gopinadhan, and Chinedum O Osuji. Directed self-assembly of block copolymers: a tutorial review of strategies for enabling nanotechnology with soft matter. *Soft Matter*, 10(22):3867–3889, 2014.

[23] Jae-Byum Chang, Hong Kyoon Choi, Adam F Hannon, Alfredo Alexander-Katz, Car-

oline A Ross, and Karl K Berggren. Design rules for self-assembled block copolymer patterns using tiled templates. *Nature Communications*, 5:3305, 2014.

[24] KG Tavakkoli, Samuel M Nicaise, Adam F Hannon, Kevin W Gotrik, Alfredo Alexander-Katz, Caroline A Ross, Karl K Berggren, et al. Sacrificial-post templating method for block copolymer self-assembly. *Small*, 10(3):493–499, 2014.

[25] Haizhou Yu, Xiaoyan Qiu, Suzana P Nunes, and Klaus-Viktor Peinemann. Self-assembled isoporous block copolymer membranes with tuned pore sizes. *Angewandte Chemie International Edition*, 53(38):10072–10076, 2014.

[26] Chiang-Jui Chu, Pei-Yun Chung, Mu-Huan Chi, Yi-Huei Kao, and Jiun-Tai Chen. Three-dimensional block copolymer nanostructures by the solvent-annealing-induced wetting in anodic aluminum oxide templates. *Macromolecular Rapid Communications*, 35(18):1598–1605, 2014.

[27] Gurpreet Singh, Kevin G Yager, Brian Berry, Ho-Cheol Kim, and Alamgir Karim. Dynamic thermal field-induced gradient soft-shear for highly oriented block copolymer thin films. *ACS Nano*, 6(11):10335–10342, 2012.

[28] Qiang Wang, Shyamal K Nath, Michael D Graham, Paul F Nealey, and Juan J de Pablo. Symmetric diblock copolymer thin films confined between homogeneous and patterned surfaces: Simulations and theory. *The Journal of Chemical Physics*, 112(22):9996–10010, 2000.

[29] Amitabha Chakrabarti and Hao Chen. Block copolymer films on patterned surfaces. *Journal of Polymer Science Part B: Polymer Physics*, 36(17):3127–3136, 1998.

[30] Christopher Harrison, Paul M Chaikin, David A Huse, Richard A Register, Douglas H Adamson, Abishai Daniel, E Huang, P Mansky, TP Russell, Craig J Hawker, et al. Reducing substrate pinning of block copolymer microdomains with a buffer layer of polymer brushes. *Macromolecules*, 33(3):857–865, 2000.

[31] Ion Bita, Joel KW Yang, Yeon Sik Jung, Caroline A Ross, Edwin L Thomas, and Karl K Berggren. Graphoepitaxy of self-assembled block copolymers on two-dimensional periodic patterned templates. *Science*, 321(5891):939–943, 2008.

[32] Claudia M Duffy, Jens W Andreasen, Dag W Breiby, Martin M Nielsen, Masahiko Ando, Takashi Minakata, and Henning Sirringhaus. High-mobility aligned pentacene films grown by zone-casting. *Chemistry of Materials*, 20(23):7252–7259, 2008.

[33] Karl Amundson, Eugene Helfand, Don D Davis, Xina Quan, Sanjay S Patel, and Steven D Smith. Effect of an electric field on block copolymer microstructure. *Macromolecules*, 24(24):6546–6548, 1991.

[34] Karl Amundson, Eugene Helfand, XN Quan, Steven D Hudson, Steven D Smith, et al.

Alignment of lamellar block-copolymer microstructure in an electric-field. 2. mechanisms of alignment. *Macromolecules*, 27(22):6559–6570, 1994.

[35] TL Morkved, M Lu, AM Urbas, EE Ehrichs, et al. Local control of microdomain orientation in diblock copolymer thin films with electric fields. *Science*, 273(5277):931, 1996.

[36] T Thurn-Albrecht, J DeRouchey, TP Russell, and HM Jaeger. Overcoming interfacial interactions with electric fields. *Macromolecules*, 33(9):3250–3253, 2000.

[37] F Ferrarese Lupi, TJ Giammaria, M Ceresoli, G Seguini, K Sparnacci, D Antonioli, V Gianotti, M Laus, and M Perego. Rapid thermal processing of self-assembling block copolymer thin films. *Nanotechnology*, 24(31):315601, 2013.

[38] Olga A Gus'kova, Pavel G Khalatur, Peter Bäuerle, and Alexei R Khokhlov. Silk-inspired 'molecular chimeras': Atomistic simulation of nanoarchitectures based on thiophene–peptide copolymers. *Chemical Physics Letters*, 461(1-3):64–70, 2008.

[39] François Drolet and Glenn H Fredrickson. Combinatorial screening of complex block copolymer assembly with self-consistent field theory. *Physical Review Letters*, 83(21): 4317, 1999.

[40] Yuliang Yang, Feng Qiu, Ping Tang, and Hongdong Zhang. Applications of self-consistent field theory in polymer systems. *Science in China Series B*, 49(1):21–43, 2006.

[41] Zhinan Cong, Liangshun Zhang, Liquan Wang, and Jiaping Lin. Understanding the ordering mechanisms of self-assembled nanostructures of block copolymers during zone annealing. *The Journal of chemical physics*, 144(11):114901, 2016.

[42] GJA Sevink and Andrei V Zvelindovsky. Block copolymers confined in a nanopore: Pathfinding in a curving and frustrating flatland. *The Journal of chemical physics*, 128 (8):084901, 2008.

[43] Takeji Hashimoto. Time-dependent ginzburg-landau approach for microphase-separation kinetics of block polymers. *Macromolecules*, 20(2):465–468, 1987.

[44] Paul C Millett. Time-dependent ginzburg-landau model for nonfrustrated linear a b c triblock terpolymers. *Physical Review E*, 92(2):022602, 2015.

[45] Takao Ohta and Kyozi Kawasaki. Equilibrium morphology of block copolymer melts. *Macromolecules*, 19(10):2621–2632, 1986.

[46] Marcus Müller and Juan J de Pablo. Computational approaches for the dynamics of structure formation in self-assembling polymeric materials. *Annual Review of Materials Research*, 43:1–34, 2013.

Chapter 2

Scientific Background

2.1 Block Copolymers

A monomer is a basic molecular unit which is able to bond with other like-kind monomers to form long chemical chains called polymers. For example, the monomer styrene can be polymerized with other styrene monomers to form the polymer poly-styrene as shown in Fig. 2.1(a,b). It is also possible to combine two or more monomer species through polymerization to create a bipolymer, tripolymer, quaterpolymer, etc. though the term typically used for polymers consisting of two or more monomers is simply copolymer. If the monomers within a single chain copolymer are segregated into blocks of unique monomer types, the resulting polymer is called a block copolymer(BCP) due to the unique blocks within the chain as shown in Fig. 2.1(c). Linear BCPs have a wide variety of applications, and are used commonly in patterning research and applications, although there are a number of other chain architectures also being explored [1–3].

2.2 Spinodal Decomposition

When two thermodynamically immiscible elements are mixed together, their chemical incompatability will cause them to separate as a means of lowering the overall chemical energy of the system, this diffusion process is known as spinodal decomposition. The driving force behind spinodal decomposition is a balance between the enthalpic, ΔH_{mix}, and entropic, $T\Delta S_{mix}$, energy terms in the Gibbs free energy of mixing

$$\Delta G_{mix} = \Delta H_{mix} - T\Delta S_{mix} \tag{2.1}$$

If ΔG_{mix} is negative, the materials are able to spontaneously mix. However, when ΔG_{mix} is positive, such as the case of immiscible fluids, enthalpy causes the mixture to spontaneously

separate in order to reduce the energy state of the system.

Consider a simple case of oil and water in a container. When mixed, the fluids will form one homogeneous liquid which rapidly separate back into unique phases of oil and water with minimum contact between phases. This process is also common in glasses [4, 5], metal alloys [6], and polymers [7]. Under proper thermodynamic conditions, immiscible polymer chains will separate into distinct phases of the different polymers, as in Fig. 2.2(a). Similar to mixtures of immiscible polymers, BCPs will spontaneously phase separate. However, due to the bonding between polymer blocks, phase separation can only occur on the molecular scale, shown in Fig. 2.2(b). During this "micro-"phase separation BCPs will self-assemble into nanoscale periodic domains. The shape of these domains are dependant mainly on the volume fraction of monomer types and can form a variety of stable structures as depicted in Fig.2.2(c,d).

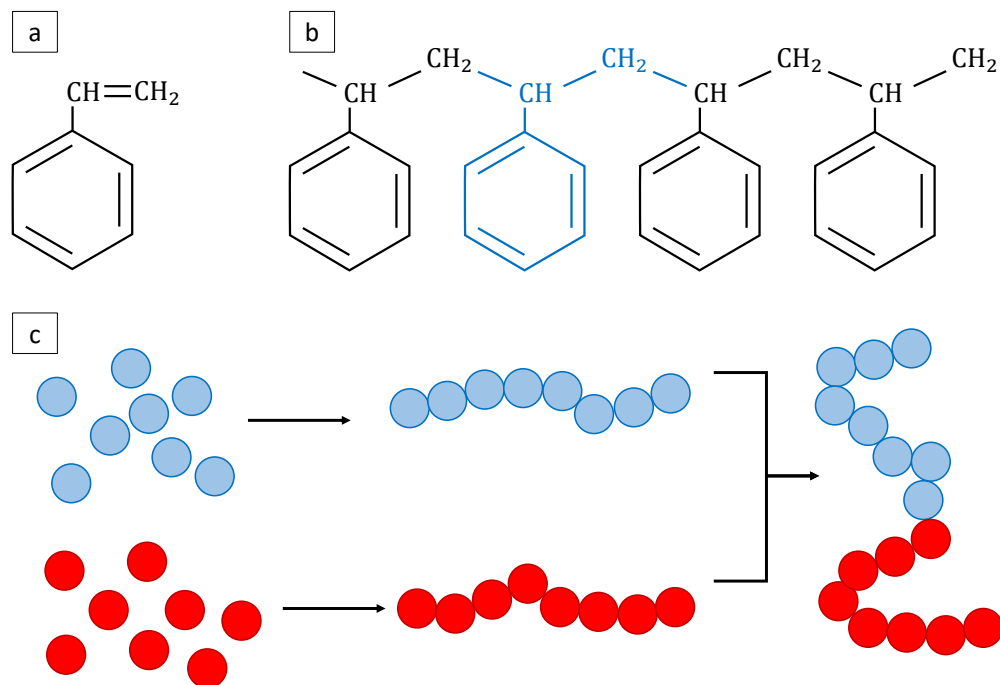Figure 2.1: Example of a polymer. (a) A common monomer, styrene. (b) Polymerized styrene, known as polystyrene, consists of a long chain of repeated styrene monomers. (c) (left)Two distinct monomers, represented as individual particles rather than by their molecular structure. (center) Distinct polymers. (right) A linear block copolymer consisting of two distinct monomers which are segregated into distinct blocks.

2.3 Phase-Separated Morphology

Phase separated morphologies in linear BCPs are dependent on three key factors: the interaction parameter, degree of polymerization, and the volume fraction. The interaction parameter, χ, also called the Flory-Huggins parameter, indicates how incompatible two polymer species are and can be used to determine whether or not the polymer species are miscible. The degree of polymerization, N, describes the average number of monomers
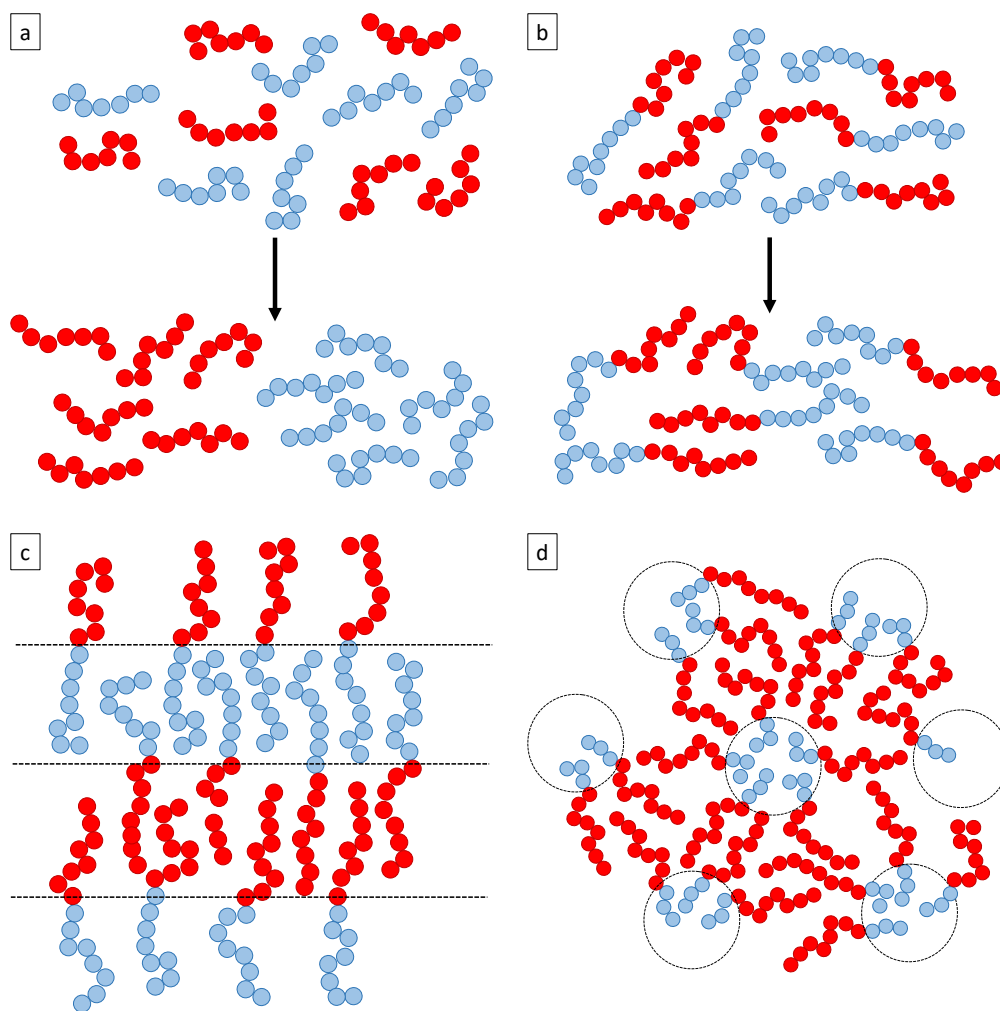
Figure 2.2: Example of phase separation. (a) An immiscible polymer blend will phase separate into distinct phases of each polymer type. (b) Due to bonding between blocks, block-copolymers consisting of immiscible polymers cannot phase separate on a macroscopic scale. Periodic domains are formed which depend on a number of factors including the ratio of block lengths. (c) Blocks which are relatively similar in length will tend to separate into lamella, or layered structures. (d) A possible structure for blocks which are dissimilar in length is hexagonally packed cylinders.

found within a single polymer chain. For BCP's, the volume fraction, f, is a ratio of a block length compared to the total length of the molecule. Shown in Fig. 2.3, stable and meta-stable phase-separated morphologies of linear diblock copolymers (BCPs with two distinct monomers) include ordered spheres, cylinders, lamellae, and gyroid structures [8–13]. The phase diagram of di-BCPs is a function of two parameters: the volume fraction of the A block, f, and the A-B interaction term χN. The variety, regularity, and size of these structures make BCPs a highly attractive option for many nano-manufacturing applications.

Though separated into unique phases, these materials do not typically fully separate at the boundaries, but have a diffuse interface as depicted in Fig. 2.4

2.4 Directed Self-Assembly

Using DSA techniques, the micro-phase separated BCP can replicate template patterns and offer a significant increase in feature resolution over current photolithography capabilities (ie. decrease producible feature sizes) [14–16]. One of the most attractive advantages
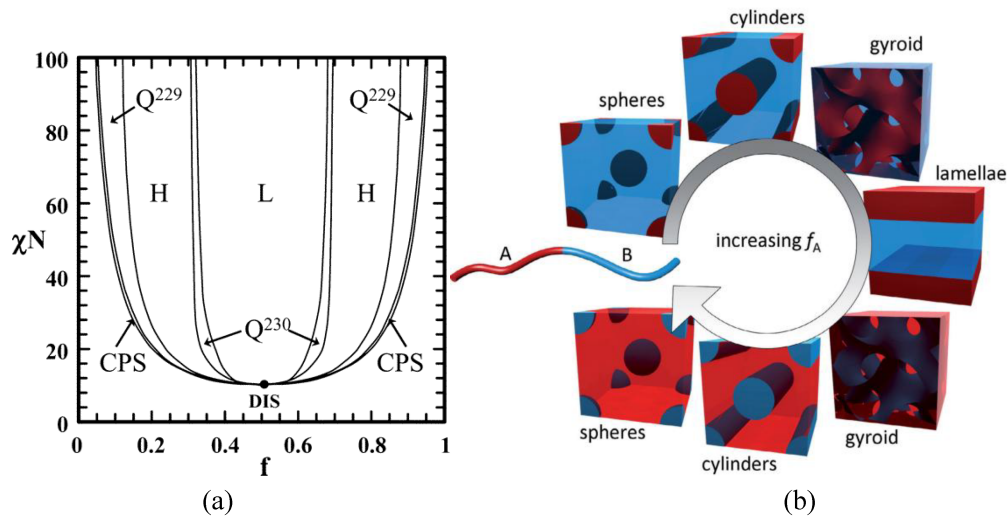
Figure 2.3: (a) Typical phase diagram of an A-B diblock copolymer. f: Volume fraction of one block. χ: Flory-Huggins interaction parameter. N: degree of polymerization. L: lamellae. H: hexagonally-packed cylinders. Q230: double-gyroid phase. Q229: body-centered spheres. CPS: closed-packed spheres. DIS: disordered. (b) Representative stable morphologies shown by their dependance on increasing values of f_A, the volume fraction of block A. Figure by Tseng and Darling [8].
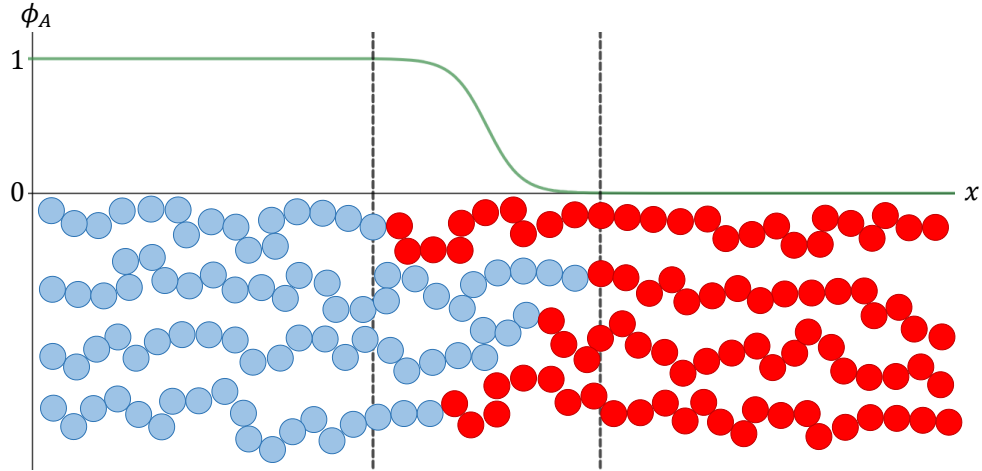
Figure 2.4: Diffuse interface between monomer A (blue) and monomer B(red) within a phase-separated block copolymer system. Interfaces between phases are not always sharp, but are often diffuse, a property which must be captured by the simulation.

offered by DSA of BPCs is the potential for high-volume cost-effective manufacturing at sub-20nm length scales with no need for advancements in the top-down approach of established lithography methods. Figure 2.5 shows SEM images of structures formed using block copolymer lithography. The domain sizes in a BCP matrix correspond with the molecular lengths of each section of the copolymer chain and can be tailored as small as 5nm.

2.5 Zone Annealing

During DSA, BCP films are initially formed in a disordered state. Phase separation can only occur above a minimum temperature termed the glass transition temperature, T_G, above

Figure 2.5: Plan view and cross-sectional SEM images of cobalt surface patterns formed from using a PS-b-PDMS block copolymer pattern transfer [17]. Morphology is largely determined by the volume fraction, f, of the blocks. (a) Spheres (b) Cylinders

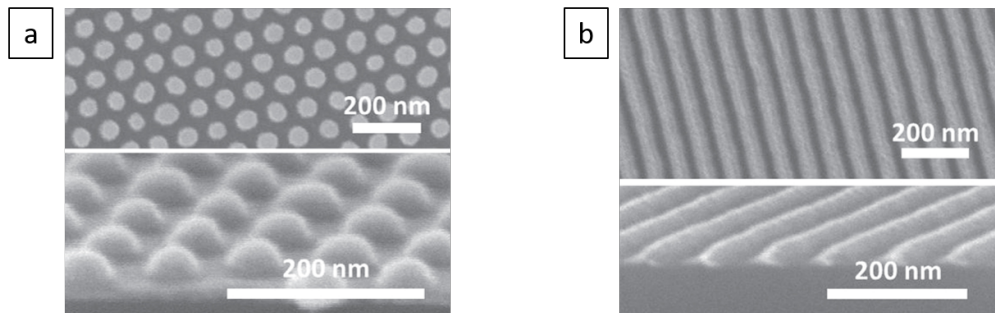which, the polymer transitions from a hard, glassy material to a softer, rubbery material where polymer chains are able to reorient via diffusion. An upper temperature limit exists called the order-disorder transition temperature, T_{OD}, above which the BCP remains in an amorphous and homogeneous state. Studies of domain morphologies have shown that directional quenching and/or annealing of a BCP film can considerably enhance the order within the system, whereby the orientation of the periodic structures is dependent on the direction and the velocity of a moving thermal gradient field [18]. This approach, termed zone annealing, involves passing a BCP film through a series of hot and cold temperature fields to impose a moving thermal gradient within the film.

The earliest implementation of zone annealing utilized temperatures in the hot zone above the T_{OD} of the BCP film [19], now designated as hot zone annealing (HZA). Subsequent efforts applied lower temperatures in the hot zone in the range of $T_G < T < T_{OD}$. This approach is designated cold-zone annealing (CZA) [20–24]. In HZA, new microdomains form and become aligned in the cooling edge of the zone, as opposed to CZA whereby new microdomains form in a narrow range on the heating edge of the zone once the temperature exceeds T_G. A somewhat related, yet distinctly different approach known as zone casting [25] involves injecting a BCP solution at an elevated temperature onto a substrate as the substrate is withdrawn perpendicular to the injection. The injection rate and withdrawal velocity are carefully controlled to maintain film thicknesses between $100nm$ and a few micrometers. It has been observed that orientation of ordered lamellae are affected by the casting temperature and withdrawal rate. Notably, both CZA and zone casting methods have shown essentially defect-free microdomain patterns when the thermal gradient velocity (or, the withdrawal velocity for zone casting) is kept below ~ 5 μm/s. Furthermore, the sharpness of the thermal gradient has been shown to affect the periodic domain orientation. A sharp thermal gradient ($\nabla T \sim 45$ K/mm) [21] in CZA has been shown to produce vertical orientation (i.e. in the z-direction of the film), while broader thermal gradients ($\nabla T \sim 17$ K/mm) result in parallel alignment for similar velocities.

Bibliography

[1] Dong-Po Song, Ying Lin, Yue Gai, Nicholas S Colella, Cheng Li, Xiao-Hui Liu, Samuel Gido, and James J Watkins. Controlled supramolecular self-assembly of large nanoparticles in amphiphilic brush block copolymers. *Journal of the American Chemical Society*, 137(11):3771–3774, 2015.

[2] Huibin Qiu, Zachary M Hudson, Mitchell A Winnik, and Ian Manners. Multidimensional hierarchical self-assembly of amphiphilic cylindrical block comicelles. *Science*, 347(6228):1329–1332, 2015.

[3] Frank S Bates, Marc A Hillmyer, Timothy P Lodge, Christopher M Bates, Kris T Delaney, and Glenn H Fredrickson. Multiblock polymers: panacea or pandora's box? *Science*, 336(6080):434–440, 2012.

[4] John W Cahn. Phase separation by spinodal decomposition in isotropic systems. *The Journal of Chemical Physics*, 42(1):93–99, 1965.

[5] Norbert Mattern, G Goerigk, U Vainio, MK Miller, T Gemming, and J Eckert. Spinodal decomposition of ni–nb–y metallic glasses. *Acta Materialia*, 57(3):903–908, 2009.

[6] A Kwiatkowski Da Silva, Dirk Ponge, Zirong Peng, Gerhard Inden, Y Lu, A Breen, Baptiste Gault, and Dierk Raabe. Phase nucleation through confined spinodal fluctuations at crystal defects evidenced in fe-mn alloys. *Nature Communications*, 9(1):1137, 2018.

[7] Pierre-Gilles de Gennes. Dynamics of fluctuations and spinodal decomposition in polymer blends. *The Journal of Chemical Physics*, 72(9):4756–4763, 1980.

[8] Yu-Chih Tseng and Seth B Darling. Block copolymer nanostructures for technology. *Polymers*, 2(4):470–489, 2010.

[9] Ludwik Leibler. Theory of microphase separation in block copolymers. *Macromolecules*, 13(6):1602–1617, 1980.

[10] AN Semenov. Contribution to the theory of microphase layering in block-copolymer melts. *Zh. Eksp. Teor. Fiz*, 88(4):1242–1256, 1985.

[11] Mark W Matsen and Michael Schick. Stable and unstable phases of a diblock copolymer melt. *Physical Review Letters*, 72(16):2660, 1994.

[12] EL Thomas, RL Lescanec, FC Frank, JS Higgins, A Klug, and IW Hamley. Phase morphology in block copolymer systems [and discussion]. *Philosophical Transactions of the Royal Society of London A: Mathematical, Physical and Engineering Sciences*, 348 (1686):149–166, 1994.

[13] Marc Hillmyer. Block copolymer synthesis. *Current Opinion in Solid State and Materials*

Science, 4(6):559–564, 1999.

[14] Ricardo Ruiz, Huiman Kang, François A Detcheverry, Elizabeth Dobisz, Dan S Kercher, Thomas R Albrecht, Juan J de Pablo, and Paul F Nealey. Density multiplication and improved lithography by directed block copolymer assembly. *Science*, 321(5891):936–939, 2008.

[15] Rachel A Segalman. Patterning with block copolymer thin films. *Materials Science and Engineering: R: Reports*, 48(6):191–226, 2005.

[16] Ion Bita, Joel KW Yang, Yeon Sik Jung, Caroline A Ross, Edwin L Thomas, and Karl K Berggren. Graphoepitaxy of self-assembled block copolymers on two-dimensional periodic patterned templates. *Science*, 321(5891):939–943, 2008.

[17] Kun-Hua Tu, Wubin Bai, George Liontos, Konstantinos Ntetsikas, Apostolos Avgeropoulos, and Caroline A Ross. Universal pattern transfer methods for metal nanostructures by block copolymer lithography. *Nanotechnology*, 26(37):375301, 2015.

[18] Hongdong Zhang, Jianwen Zhang, Yuliang Yang, and Xuedong Zhou. Microphase separation of diblock copolymer induced by directional quenching. *The Journal of Chemical Physics*, 106(2):784–792, 1997.

[19] Jeffrey Bodycomb, Yoshinori Funaki, Kohtaro Kimishima, and Takeji Hashimoto. Single-grain lamellar microdomain from a diblock copolymer. *Macromolecules*, 32(6): 2075–2077, 1999.

[20] Brian C Berry, August W Bosse, Jack F Douglas, Ronald L Jones, and Alamgir Karim. Orientational order in block copolymer films zone annealed below the order- disorder transition temperature. *Nano Letters*, 7(9):2789–2794, 2007.

[21] Gurpreet Singh, Kevin G Yager, Detlef-M Smilgies, Manish M Kulkarni, David G Bucknall, and Alamgir Karim. Tuning molecular relaxation for vertical orientation in cylindrical block copolymer films via sharp dynamic zone annealing. *Macromolecules*, 45 (17):7107–7117, 2012.

[22] Kevin G Yager, Nathaniel J Fredin, Xiaohua Zhang, Brian C Berry, Alamgir Karim, and Ronald L Jones. Evolution of block-copolymer order through a moving thermal zone. *Soft Matter*, 6(1):92–99, 2010.

[23] August W Bosse, Jack F Douglas, Brian C Berry, Ronald L Jones, and Alamgir Karim. Block-copolymer ordering with a spatiotemporally heterogeneous mobility. *Physical Review Letters*, 99(21):216101, 2007.

[24] Changhuai Ye, Yan Sun, Alamgir Karim, and Bryan D Vogt. Extending dynamic range of block copolymer ordering with rotational cold zone annealing (rcza) and ionic liquids. *Macromolecules*, 48(20):7567–7573, 2015.

[25] Chuanbing Tang, Wei Wu, Detlef-M Smilgies, Krzysztof Matyjaszewski, and Tomasz Kowalewski. Robust control of microdomain orientation in thin films of block copolymers by zone casting. *Journal of the American Chemical Society*, 133(30):11802–11809, 2011.

Chapter 3

Computational Methods

While the published papers in Chapters 4 and 5 offer sufficient details to reproduce the computational methods used, this chapter will offer more in-depth details of the computational models and algorithms used to produce and analyze data.

3.1 Time Dependant Ginzburg Landau Model

This section details the computational model used to simulate 2-D lamella forming generic BCPs of immiscible monomer types found in Chapter 4.

To model the behavior of spinodal decomposition, a Cahn-Hilliard-Cook (CHC) equation is used which describes the morphological evolution by spatially and temporally updating an order parameter representing the local polymer concentration. Because it is assumed that $\phi_A + \phi_B = 1$, it is only necessary to track one of these concentrations, i.e. only ϕ_A is calculated. For these simulations, the CHC equation of the form

$$\frac{\partial \phi_A}{\partial t} = \nabla \cdot \left(M_A \nabla \frac{\delta F(\phi_A)}{\delta \phi_A} \right) + \xi(\mathbf{r}, t), \tag{3.1}$$

is used. In the CHC equation, M_A represents monomer species mobility, $F(\phi_A)$ is a free energy functional, and $\xi(\mathbf{r}, t)$ represents thermal noise. Derived from conservation laws [1, 2], eqn. 3.1 ensures global conservation of ϕ_A.

3.1.1 Species Mobility

Polymer mobility is highly temperature-dependent, particularly as the system transitions from below to above the glass transition temperature [3]. Therefore, in this model, mobility and temperature are directly linked. Under cold-zone annealing conditions, mobility is modeled by prescribing a spatially- and temporally-dependent species mobility, M_A, by applying

a smooth functional form

$$M_A = \frac{1}{2}\left[1 - tanh\left(\frac{6(x_i - (t \cdot v_{zone} - 0.5w_{zone}))}{w_{zone}}\right)\right] \qquad (3.2)$$

where x_i is the local x-position within the domain, t is the current simulation time calculated by $N_{step} \cdot \Delta t$, w_{zone} is the width of the temperature transition zone, and v_{zone} is the velocity of the temperature transition zone. Isothermally annealed results are modeled with a constant mobility having a value of $M_A = 1$.

3.1.2 Free Energy

Phase separation is induced by a free energy functional $F(\phi_A)$, which consists of both short- and long-range terms

$$F(\phi_A) = F_S(\phi_A) + F_L(\phi_A), \qquad (3.3)$$

where the short-range chemical mixing energy is defined in the TGDL model by a polynomial expression combined with a gradient term

$$F_S(\phi_A) = \int [\psi\phi_A^2(1 - \phi_A)^2 + \kappa|\nabla\phi_A|^2]d\mathbf{r}, \qquad (3.4)$$

The first term creates a double-well potential curve that produces a miscibility gap by penalizing volume fractions between $\phi_A = 0$ and $\phi_A = 1$. A polynomial expression such as this is routinely substituted for a Flory-Huggins model [4], as it provides better numerical efficiency while still qualitatively describing an immiscible mixture. It should be noted, however, that this substitution makes the results generic and not material-specific. A material-specific free energy potential can be included at the cost of computational speed. The gradient term in eqn. 3.4 penalizes gradients in ϕ_A that occur at A-B interfaces. The scaling parameters ψ and κ together influence the mixing energy, thus relating to the Flory-Huggins factor χN as well as the diffuse width of the A-B interface. The long-range term in eqn. 3.3 introduces a

domain growth restriction due to the chain length of the A and B chains, and is defined by

$$F_L(\phi_A) = \frac{\alpha}{2} \int d\mathbf{r} \int d\mathbf{r}' G(\mathbf{r} - \mathbf{r}') \phi_A(\mathbf{r}) \phi_A(\mathbf{r}') \tag{3.5}$$

where the Green function $G(\mathbf{r} - \mathbf{r}')$ satisfies $\nabla^2 G(\mathbf{r} - \mathbf{r}') = -\delta(\mathbf{r} - \mathbf{r}')$ and the coefficient α is proportional to $(Nf(1 - f))^{-2}$ where N is the total degree of polymerization and f is the volume fraction of monomer A [5].

3.1.3 Thermal Noise

The final term in eqn. 3.1 introduces thermal noise which is applied directly as random variations in local concentration. Without the application of thermal noise, the CHC equation is essentially a mean-field theory which approximates interaction between neighbor nodes by mean values which may predict dynamic behavior of the system incorrectly [1]. To ensure that mass is conserved, this term is applied globally and normalized so that the spatial average is zero.

3.1.4 Chemoepitaxial Templating

The TDGL model utilizes a free energy functional where the short-range chemical energy in Eqn. 3.4 is defined by a polynomial of the form

$$\phi_A^2(1 - \phi_A)^2 \tag{3.6}$$

This double-well potential curve penalizes polymer concentrations between 0 and 1 which induces the phase separation behavior by driving concentration toward one or the other. Depicted in Fig. 3.1, this free energy functional is modified to the form

$$\phi_A^2(1 - \phi_A)^2 + \eta \phi_A^2 \tag{3.7}$$

for simulations where templating is applied. In this equation, η is a boolean variable used to change the double-well potential into a single-well which penalizes concentrations that
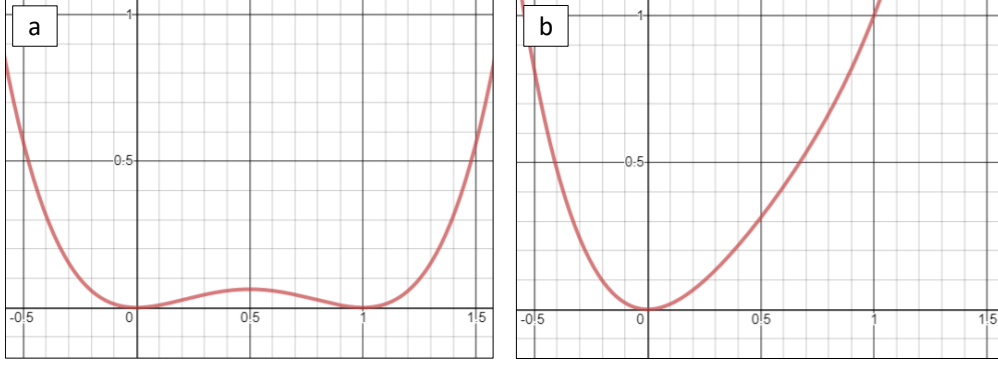
Figure 3.1: a) Short-range chemical energy under general conditions. b) Short-range chemical energy in templated regions.

are non-zero. This enforces templated regions by driving concentration towards $\phi_A = 0$, corresponding to the B-rich phase.

3.2 Concentration Gradient Orientation Mapping

The analysis algorithm used to create false color maps shown in Chapter 4 was developed to quickly analyze 2-D lamella patterns and calculate the local pattern orientation based on the gradient between nearest neighbor nodes. Gradients on node (i, j) of ϕ_A are calculated by

$$\nabla X = \frac{\phi_{i-1,j} - \phi_{i+1,j}}{2} \tag{3.8}$$

$$\nabla Y = \frac{\phi_{i,j-1} - \phi_{i,j+1}}{2} \tag{3.9}$$

and orientation is calculated as

$$\theta = \left(tan^{-1} \left(\frac{\nabla Y}{\nabla X} \right) + \frac{\pi}{2} \right) \cdot \frac{180}{\pi} \tag{3.10}$$

resulting in orientation values between $\theta = 0°$ and $\theta = 180°$. Near maxima and minima, the gradient can be overly sensitive to small changes. The magnitude of each gradient is calculated by

$$\nabla = \left(\nabla X^2 + \nabla Y^2 \right)^{\frac{1}{2}} \tag{3.11}$$

and normalized to values between $\nabla = 0$ and $\nabla = 1$. To prevent erroneous orientation calculations, a threshold of 0.2 is established and the orientation of nodes where $\nabla < 0.2$ are eliminated. This process is depicted in Fig. 3.2. After orientation is calculated, data is
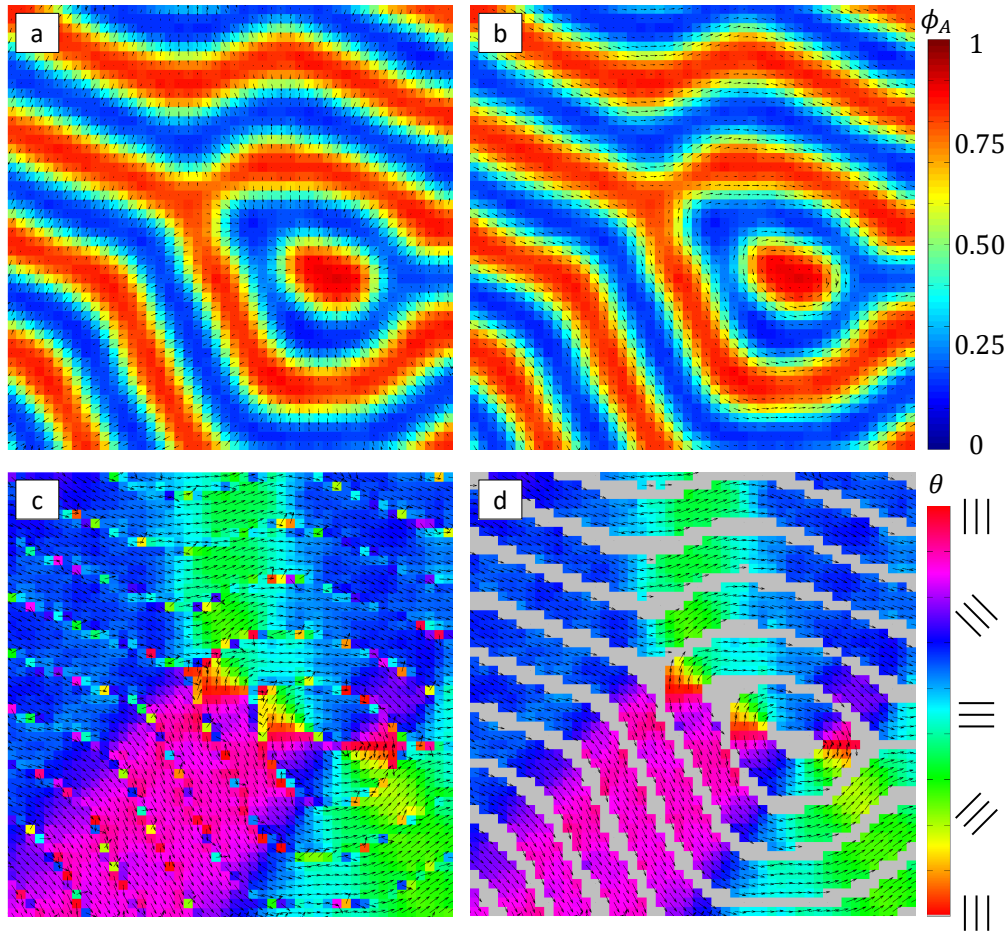
Figure 3.2: a) Concentration field with relative gradients shown. b) Concentration field with orientation scaled by gradient magnitude. c) Orientation color map is applied, non-scaled orientation arrows are shown. d) Erroneous orientation near concentration maxima and minima are removed and color map is grayed out for emphasis.

returned and analyzed. The degree to which the field is oriented parallel or perpendicular to the direction of zone annealing within some tolerance is of key interest. Results presented in Chapter 4 are calculated with a tolerance of $\pm 30°$.

3.3 Optimized Phase Field Model

This section details the computational model used to generate 3-D sphere forming PS-b-PMMA BCPs use in Chapter 5. Like the TDGL model described in Section 3.1, the optimized phase field (OPF) method uses the Cahn-Hilliard-Cook equation, Eqn. 3.1 to describe changing morphological behavior and ensure conservation of mass.

3.3.1 Species Mobility

Mobility of polymer species is calculated according to Eqn. 3.2. However, in this model local temperature is calculated explicitly through

$$T_i = T_g + M_i(T_{max} - T_g) \qquad (3.12)$$

describing the linear relationship between temperature and mobility as temperature increases from T_g to T_{max}. This local temperature is used to calculate local χ values throughout the simulation. Unlike the TDGL model, the OPF model does not approximate the phase separation energy as broadly and therefore presents results which are more accurate and are tied to specific materials through the experimentally derived entropic and enthalpic contributions to the temperature dependant Flory-Huggins parameter [6]

$$\chi(T) = \beta + \frac{\alpha}{T} \qquad (3.13)$$

where α and β represent these contributions respectively.

3.3.2 Free Energy

The free energy functional used in the OPF model was developed by Liu et al. [7–9]. This free energy, $F(\phi_A)$, consists of long- and short-range terms as in Eqn. 3.3 which represent local and bulk effects of the free energy landscape. In this model, the polynomial expression representing short-range chemical mixing is

$$F_S(\phi_A) = \int [c_2(\delta\phi_A)^2 + c_3(\delta\phi_A)^3 + c_4(\delta\phi_A)^4 + c_5|\nabla\phi_A|^2]d\mathbf{r} \qquad (3.14)$$

25

where $\delta\phi_A = \phi_A - 0.5$. The first three terms in Eqn. 3.14 describe a double well potential curve producing a miscibility gap between $\phi_A = 0$ and $\phi_A = 1$ and the fourth term restricts the concentration gradient of ϕ_A at the interface between distinct polymer phases. The coefficients can be calculated using Table 3.1 and

$$c_2 = -\sum_{j=0}^{2}\sum_{k=0}^{2} b_{jk}^{(2)} x^j g^{2k} \tag{3.15}$$

$$c_3 = -\sum_{j=0}^{2}\sum_{k=0}^{2} b_{jk}^{(3)} x^j g^{2k+1} \tag{3.16}$$

$$c_4 = \sum_{j=0}^{2}\sum_{k=0}^{2} b_{jk}^{(4)} x^j g^{2k} \tag{3.17}$$

$$c_5 = \frac{\sum_{k=0}^{2}(b_{0k}^{(5)} + b_{1k}^{(5)} x)g^{2k}}{1 + \sum_{k=0}^{2} b_{2k}^{(5)} x g^{2k}} \tag{3.18}$$

where $g = 0.5 - f$ and $x = \chi N - \chi N_s$. Here, χN is the Flory-Huggins parameter calculated in Eqn. 3.13 times the degree of polymerization, N. The value χN_s represents the random phase approximation (RPA) [10], an estimated curve below which phase separation is not predicted to occur. Values for χN_s are shown in Table 3.2. A polynomial fit to these points is used to determine a minimum value for χN below which simulation results are not considered valid.

The long range term in the free energy functional reflects the physical restriction of phase separation due to polymer chain length and is calculated by

$$F_L(\phi_A) = c_6 \int d\mathbf{r} \int d\mathbf{r}' G(\mathbf{r} - \mathbf{r}')\phi_A(\mathbf{r})\phi_A(\mathbf{r}') \tag{3.19}$$

where, as with the TDGL model, $\nabla^2 G(\mathbf{r}-\mathbf{r}') = -\delta(\mathbf{r}-\mathbf{r}')$ satisfies the Green function $G(\mathbf{r}-\mathbf{r}')$. The coefficient c_6 is calculated using Table 3.1 and

		$k=0$	$k=1$	$k=2$
$b_{jk}^{(2)}$	$j=0$	5.920	-14.31	-398.5
	$j=1$	2.025	-4.285	39.47
	$j=2$	0.005522	-0.1915	-1.003
$b_{jk}^{(3)}$	$j=0$	9.741	-39.46	-999.0
	$j=1$	9.224	14.69	-510.3
	$j=2$	0.06433	-1.281	15.70
$b_{jk}^{(4)}$	$j=0$	9.686	53.00	-1775.0
	$j=1$	3.6	0.0	0.0
	$j=2$	0.02068	-0.2385	-0.4559
$b_{jk}^{(5)}$	$j=0$	0.7885	-5.654	-16.22
	$j=1$	0.2119	-1.170	3.659
	$j=2$	0.1178	-0.7423	5.481
$b_{jk}^{(6)}$	$j=0$	0.5	0.0	0.0
	$j=1$	0.2230	-1.956	7.147
	$j=2$	0.0006666	-0.02858	0.05316

Table 3.1: OPF Model Parameters

$|g|$	χN_s
0.00	10.495
0.05	10.698
0.10	11.344
0.15	12.562
0.20	14.635
0.25	18.172
0.30	24.613
0.35	38.038

Table 3.2: Random Phase Approximation values

$$c_6 = \frac{-c_2}{\sum_{j=0}^{2} \sum_{k=0}^{2} b_{jk}^{(6)} x^j g^{2k}} \tag{3.20}$$

This approach, while computationally more intensive than the TDGL model, yields results that are in better agreement with self-consistent field theory models that are significantly more computationally intensive. Simulation results show that this model is capable of producing self-assembled morphologies including sphere, cylinder, gyroid, and lamellar morphologies for different input volume fractions as shown in Fig. 3.3.
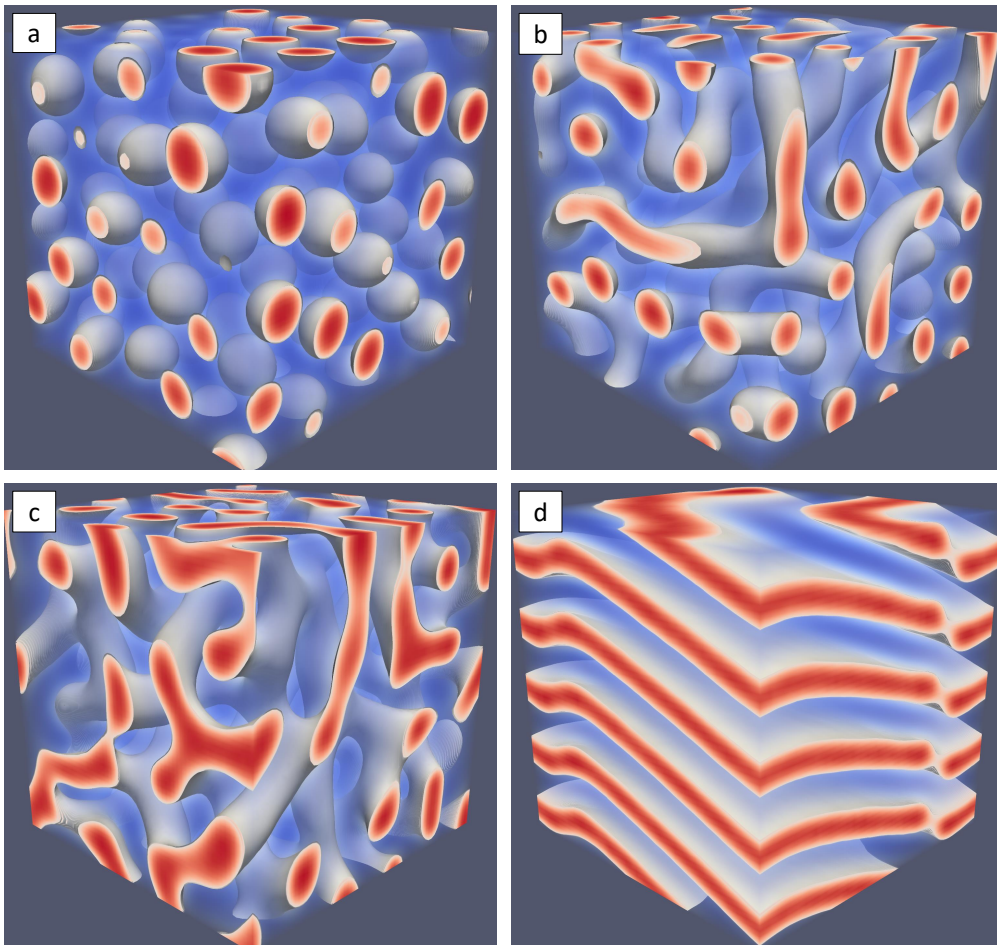

Figure 3.3: Representative morphologies generated by the OPF model. The minority polymer A (red) is solid while the majority polymer B (blue) is semitransparent. The diffuse interface (white) is ehnanced to show where separation occurs. a) $c_0 \approx 0.32$, Sphere forming minority polymer. b) $c_0 \approx 0.36$, Cylindrical minority polymer structures. c) $c_0 \approx 0.4$, Double Gyroid. Both polymer types form a pattern of interconnected branched structures. d) $c_0 \approx 0.5$, Lamellar structures composed of alternating layers of polymer types are formed.

A large-scale parametric study has been performed where f and N are varied and χ is held constant by implementing a constant temperature. Due to the symmetric nature of the diagram, only values where $f \leq 0.5$ are considered. Representative morphologies for sphere, cylinder, gyroid, and lamella forming BCPs are shown in Fig. 3.3. Morphologies are highly dependent on f and moderately dependent on χN, especially near the separation limit, χN_s. Figure 3.4 shows the resulting phase diagram which appears as expected in comparison with Fig. 2.3(a).

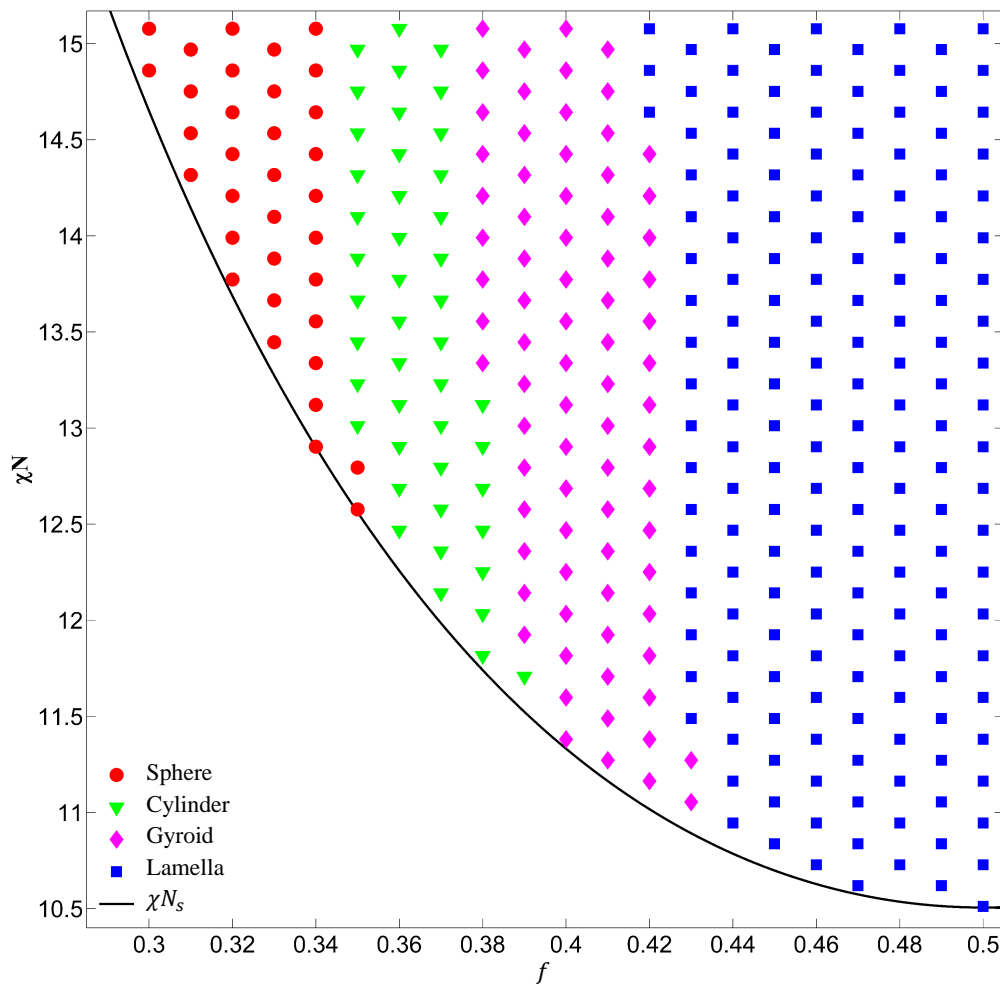Figure 3.4: A phase diagram for the OPF model. Data points represent individual simulations of a phase separating BCP where $nx = ny = nz = 64$. Bulk simulations are evaluated for the dominant phase present after reaching a meta-stable state. States found consist of sphere, cylinder, gyroid, and lamella morphologies. The line χN_s shows the minimum phase separation limit below which accuracy is not endorsed for the OPF model.

3.3.3 Chemoepitaxial Templating

Three dimensional simulations for this study are designed to use a 3-D grid of discrete points to represent locations within the bulk BCP, an additional layer of discretized points are added to all outer edges of the simulation space and are used to enforce boundary conditions within the simulation space. The application of chemoepitaxial templating for 3-D simulations occurs within this boundary layer on the lower substrate. The desired template spacing is calculated and locations where the templating is to exist are determined. From these calculated points, a circle within the 2-dimensional layer is placed and all boundary layer points within the circle are maked as template points with a fixed value of $\phi_A = 1$. All non-templated points are left free to apply the prescribed boundary conditions.

3.4 Concentration Maxima Cell-Orientation Mapping

This is the analysis algorithm used to calculate orientation information for 3-D sphere-forming PS-b-PMMA results found in Chapter 5. While these simulations are carried out in 3-D, they are designed so that results can be analyzed in 2-D. The simulations replicate a sphere-forming BCP thin-film where hemispheres form on the upper and lower surfaces of the film. Chemoepitaxial templating is applied to the lower substrate to induce order at the lower surface of the thin-film. Orientation analysis is calculated at the upper surface so that templating does not directly affect the analysis.

Data from only the upper surface of the simulation is considered. Concentration is normalized to values between $\phi_A = 0$ and $\phi_A = 1$. Data below a set threshold are removed. For this work, the threshold was set to $\phi_{A_{min}} = 0.85$ which reveals concentration clusters near the center of each upper hemisphere. Each cluster is analyzed to identify the local maxima which are recorded as grid points. To ensure that multiple clusters are not grouped together, the local maxima search is limited to a diameter equal to the BCP separation distance L_0. Delaunay triangulation [11, 12] is performed on the set of points to determine nearest neighbors. Finally, each set of Delaunay neighbors are treated as a unit cell and

the largest distance across the cell is calculated. This distance vector is compared to the direction of zone velocity and the angle between is calculated and assigned as θ to the node at the center of each cell where θ has values between $\theta = 0°$ and $\theta = 180°$. For visualization purposes, orientation is interpolated across the simulation space to create an orientation map using periodic bounds for θ. This process is depicted in Fig. 3.5.

3.5 Length and Time Scales

Length and time scales in the results presented in Chapters 4 & 5 are given in terms of $\tilde{l}$ and $\tilde{t}$ respectively. These units refer to the spatial and temporal steps taken within the model and can not be directly extracted. These values can be extrapolated indirectly for Chapter 5 by considering the physical properties that were modeled in the published work. The degree of polymerization used is $N = 385$. At T_{MAX}, $\chi = 0.038$, and the average domain spacing is $L_0 = 15.18\tilde{l}$. For PS-b-PMMA, the domain spacing can be calculated as $L_0 \approx \chi^{1/6} N^{2/3} nm$ [13] yielding a result of $L_0 \approx 34.95 nm$. This translates into $\tilde{l} \approx 2.302 nm$. The time scale can be found by the temperature dependent diffusivity constant for PS-b-PMMA, δ, where $\delta = \frac{\tilde{l}^2}{\tilde{t}}$, therefore, $\tilde{t} \approx \frac{(2.302nm)^2}{\delta}$. The diffusivity of PS-b-PMMA near T_{max} is estimated to be $\delta \approx 0.75 nm^2/s$ [14], yielding a time scale of $\tilde{t} \approx 7.066 s$.
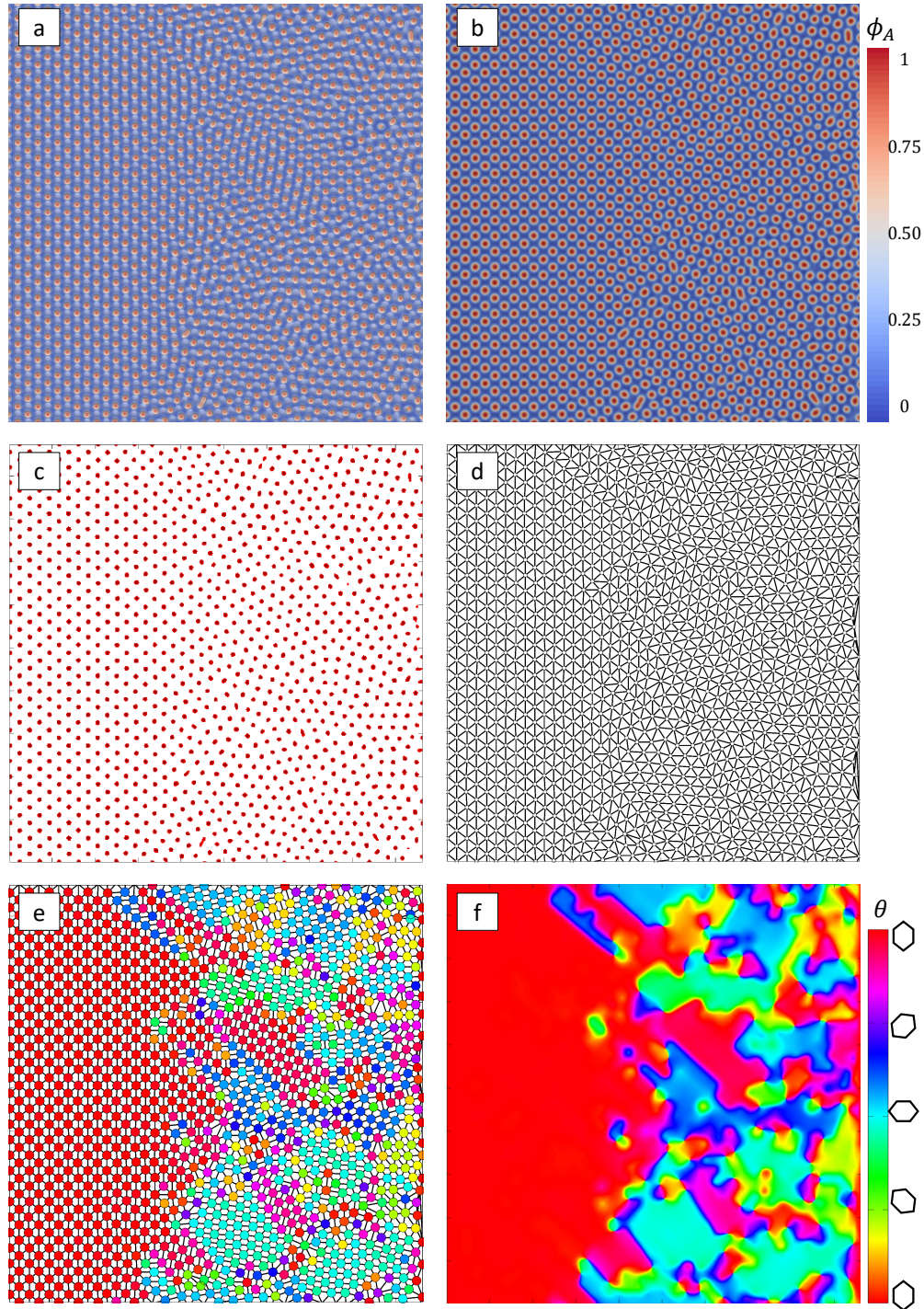
Figure 3.5: a) Simulation results in 3-dimensions. b) Upper surface to be analyzed for orientation. Concentration values are normalized between 0 and 1. c) Concentration values below a threshold of 0.85 are removed showing local concentration clusters. d) Local clusters are analyzed for maxima and Delaunay triangulation is performed on the resulting points. e) Orientation of Delaunay cells are calculated and assigned to the center node of each cell. f) Local orientation is interpolated across simulation area to generate an orientation map.

Bibliography

[1] Kenneth A Hawick and Daniel P Playne. Modelling and visualizing the cahn-hilliard-cook equation. In *MSV*, pages 149–155, 2008.

[2] A. Ziya Akcasu. Microscopic derivation and extension of the cahn-hilliard-cook theory in polymer blends. *Macromolecules*, 22(9):3682–3689, 1989.

[3] August W Bosse, Jack F Douglas, Brian C Berry, Ronald L Jones, and Alamgir Karim. Block-copolymer ordering with a spatiotemporally heterogeneous mobility. *Physical Review Letters*, 99(21):216101, 2007.

[4] Travis H Russell, Brian J Edwards, and Bamin Khomami. Characterization of the flory-huggins interaction parameter of polymer thermodynamics. *EPL (Europhysics Letters)*, 108(6):66003, 2015.

[5] Ian W Hamley. Cell dynamics simulations of block copolymers. *Macromolecular Theory and Simulations*, 9(7):363–380, 2000.

[6] Thomas P Russell, Rex P Hjelm Jr, and Phil A Seeger. Temperature dependence of the interaction parameter of polystyrene and poly (methyl methacrylate). *Macromolecules*, 23(3):890–893, 1990.

[7] Jimmy Liu, Kris T Delaney, and Glenn H Fredrickson. Phase field mapping for accurate, ultrafast simulations of directed self-assembly. In *Advances in Patterning Materials and Processes XXXIII*, volume 9779, page 977920. International Society for Optics and Photonics, 2016.

[8] Jimmy Liu, Kris T Delaney, and Glenn H Fredrickson. Optimized phase field models in confinement: fast and accurate simulations of directed self-assembly. In *Advances in Patterning Materials and Processes XXXIV*, volume 10146, page 101460Z. International Society for Optics and Photonics, 2017.

[9] Jimmy V Liu, Carlos J García-Cervera, Kris T Delaney, and Glenn H Fredrickson. Optimized phase field model for diblock copolymer melts. *Macromolecules*, 52(7):2878–2888, 2019.

[10] Ludwik Leibler. Theory of microphase separation in block copolymers. *Macromolecules*, 13(6):1602–1617, 1980.

[11] Der-Tsai Lee and Arthur K Lin. Generalized delaunay triangulation for planar graphs. *Discrete & Computational Geometry*, 1(3):201–217, 1986.

[12] Karim R Gadelrab, Yi Ding, Ricardo Pablo-Pedro, Hsieh Chen, Kevin W Gotrik, David G Tempel, Caroline A Ross, and Alfredo Alexander-Katz. Limits of directed self-assembly in block copolymers. *Nano Letters*, 18(6):3766–3772, 2018.

[13] Thomas Bennett. Self-assembly and structure-property behaviour of block copolymer/ionic liquid composites. 2016.

[14] Adam M Welander, Huiman Kang, Karl O Stuen, Harun H Solak, Marcus Müller, Juan J de Pablo, and Paul F Nealey. Rapid directed assembly of block copolymer films at elevated temperatures. *Macromolecules*, 41(8):2759–2761, 2008.

Chapter 4

Paper 1: Numerical Simulations of Directed Self-Assembly in Diblock Copolymer Films using Zone Annealing and Pattern Templating

Co-Author: Paul C. Millett

4.1 Abstract

Bulk fabrication of surface patterns with sub-20 nm feature sizes is immensely desirable for many existing and emerging technologies. Directed self-assembly (DSA) of block copolymers (BCPs) has been a recently demonstrated approach to achieve such feature resolution over large-scale areas with minimal defect populations. However, much work remains to understand and optimize DSA methods in order to move this field forward. This paper presents large-scale numerical simulations of zone annealing and chemo-epitaxy processing of BCP films to achieve long-range orientational order. The simulations utilize a Time-Dependent Ginzburg-Landau model and parallel processing to elucidate relationships between the magnitude and velocity of a moving thermal gradient and the resulting BCP domain orientations and defect densities. Additional simulations have been conducted to study to what degree orientational order can be further improved by combining zone annealing and chemo-epitaxy techniques. It is found that these two DSA methods do synergistically enhance long-range order with a particular relationship between thermal gradient velocity and chemical template spacing.

4.2 Introduction

The ability to accurately produce nanoscale surface patterns has become a driving factor for research in many fields. As the need for nanoscale manufacturing increases, new processing technologies must be developed in order to meet industry needs. A number of different patterning methods have shown progress in decreasing feature size beyond the capabilities of traditional lithography [1]. These methods include extreme ultraviolet lithography, nanoim-

printing, maskless lithography, and directed self-assembly (DSA) of block copolymers (BCP) [2–7]. BCPs can form very monodisperse periodic domains with domain sizes that can be tailored as small as 5 nm. The domain sizes in a microphase separated BCP matrix correspond with the molecular lengths of each section of the copolymer chain [8]. Linear BCPs are commonly used for patterning research and applications, although other chain architectures are also being explored [9–11]. The phase-separated morphologies of linear BCPs are dependent on the interaction parameter χ, degree of polymerization N, and the ratio of the length of each block f. Stable and meta-stable morphologies include ordered spheres, cylinders, lamellae, and gyroid structures [12–16]. The variety, regularity, and small size of these structures make BCPs highly attractive for many nano-manufacturing applications.

The microphase separation of BCP thin films has been broadly studied and shown to be useful for surface patterning and membrane applications [17]. These formations, while periodic, are prone to defects such as dislocations and grain boundaries that detract from their utility in some applications. A variety of strategies have been developed to extend defect-free uniformity during self-assembly including solvent annealing [18], shear alignment [19], epitaxy [20–23], zone casting [24], and field alignment [25–29]. Studies of domain morphologies have shown that directional quenching and/or annealing of a BCP film can considerably enhance the order within the system, whereby the orientation of the periodic structures is dependent on the direction and the velocity of a moving thermal gradient field [30]. This approach, termed zone annealing, involves passing a BCP film through a series of hot and cold temperature fields to impose a moving thermal gradient within the film.

The earliest implementation of zone annealing utilized temperatures in the hot zone above the order-disorder temperature (T_{ODT}) of the BCP film [31], now designated as hot zone annealing (HZA). Subsequent efforts applied lower temperatures in the hot zone in the range of $T_G < T < T_{ODT}$ where T_G is the glass transition temperature, and this approach is designated cold zone annealing (CZA) [32–36]. In HZA, new microdomains form and become aligned in the cooling edge of the zone, as opposed to CZA whereby new microdomains form

in a narrow range on the heating edge of the zone once the temperature exceeds T_G. A somewhat related, yet distinct, approach known as zone casting [37] involves injecting a BCP solution at an elevated temperature onto a colder substrate as the substrate is withdrawn perpendicular to the injection. The injection rate and withdrawal velocity are carefully controlled to maintain film thicknesses between $100nm$ and a few micrometers. It has been observed that orientation of ordered lamellae are affected by the casting temperature and withdrawal rate. Remarkably, both CZA and zone casting methods have shown essentially defect-free microdomain patterns when the thermal gradient velocity (or, the withdrawal velocity for zone casting) is kept below $\sim 5~\mu$m/s. Furthermore, the sharpness of the thermal gradient has been shown to affect the periodic domain orientation. A sharp thermal gradient ($\nabla T \sim 45$ K/mm) [33] in CZA has been shown to produce vertical orientation (i.e. in the z-direction of the film) while broader thermal gradients ($\nabla T \sim 17$ K/mm) result in parallel alignment for similar velocities.

Computational studies including both atomistic and mesoscale simulations have expanded our understanding of many different DSA approaches to control BCP morphology [8, 35, 38–41]. In particular, mesoscopic methods including self-consistent field theory and time-dependent Ginzburg-Landau (TDGL) models offer the required spatial resolution to represent the BCP domain structure while also allowing the computational efficiency to analyze fairly large sections of a BCP matrix. With regards to DSA, numerical simulations have been used to study BCP defect behavior in topologically and/or chemically patterned substrates [42, 43], magnetic- and electric-field alignment with and without nanoparticle loading [44–46], as well as a few studies of thermal gradient zone annealing alignment [30, 35, 47].

In this work, we present large-scale TDGL simulations to analyze the degree of BCP microdomain orientation and the defect populations during the CZA process. We systematically vary both the magnitude and the velocity of a moving thermal gradient translating across an initially disordered BCP film. Results illustrate direct relationships between these two parameters and the resultant microdomain orientations that emerge. Furthermore, we

investigate how a combination of CZA and chemical template alignment patterns can syner-gistically enhance each other to further improve long-range order within a film. The addition of templating patterns effectively allows increased CZA velocities while maintaining defect-free domains.

4.3 Methods

In the current work, we consider an idealized AB diblock copolymer film with equal vol-ume fractions of the A and B monomers, ϕ_A and ϕ_B. We strive to replicate CZA experiments [32], in which a film is spin-coated as a dense, disordered layer that is largely devoid of a solvent. Hence, this binary system – if assumed to be incompressible – should reasonably obey the condition $\phi_A + \phi_B = 1$, and we therefore can consider one independent volume fraction, e.g. ϕ_A. We utilize the coarse-grained TDGL model commonly invoked to simu-late relatively large regions of a block copolymer phase-separated microstructure [37, 48]. A Cahn-Hilliard equation describes the kinetic morphology change by spatially and temporally updating an order parameter, here corresponding to ϕ_A:

$$\frac{\partial \phi_A}{\partial t} = \nabla \cdot \left(M_A \nabla \frac{\delta F(\phi_A)}{\delta \phi_A} \right) + \xi(\mathbf{r}, t), \tag{4.1}$$

where M_A represents the of monomer A (assumed to be equal to M_B), $F(\phi_A)$ is a free energy functional representing the short- and long-range chemical energy of mixing between the monomer species, and $\xi(\mathbf{r}, t)$ is a normalized random noise term spatially averaging zero. Equation (1) ensures global conservation of ϕ_A.

Micro-phase separation is induced by the proper definition of $F(\phi_A)$, which consists of both short- and long-range terms:

$$F(\phi_A) = F_S(\phi_A) + F_L(\phi_A), \tag{4.2}$$

where the short-range chemical mixing energy is defined by a simple polynomial expression

38

combined with a gradient term:

$$F_S(\phi_A) = \int [\psi \phi_A^2 (1 - \phi_A)^2 + \kappa |\nabla \phi_A|^2] d\mathbf{r}, \tag{4.3}$$

where the first term represents a double-well curve that produces a miscibility gap by penalizing volume fractions between $\phi_A = 0$ and $\phi_A = 1$. A polynomial expression such as this is routinely substituted for a Flory-Huggins model [49], as it provides better numerical efficiency while still qualitatively describing an immiscible mixture. The second term penalizes gradients in ϕ_A that occur at A-B interfaces. The scaling parameters ψ and κ together influence the mixing energy, thus relating to the Flory-Huggins factor χN as well as the diffuse width of the A-B interface. The long-range term penalizes domain growth due to the physical attachment of the A and B chains, and is defined by:

$$F_L(\phi_A) = \frac{\alpha}{2} \int d\mathbf{r} \int d\mathbf{r}' G(\mathbf{r} - \mathbf{r}') \phi_A(\mathbf{r}) \phi_A(\mathbf{r}') \tag{4.4}$$

where the Green function $G(\mathbf{r} - \mathbf{r}')$ satisfies $\nabla^2 G(\mathbf{r} - \mathbf{r}') = -\delta(\mathbf{r} - \mathbf{r}')$ and the coefficient α is proportional to $(Nf(1 - f))^{-2}$ where N is the total degree of polymerization and f is the fraction of A monomers on the chain. For all simulations herein, we assign $f = 0.5$ corresponding to lamellae morphologies on the BCP phase diagram. While this form of the Green function was developed to describe bulk BCP systems, it has been shown that significant deviation is not introduced near solid walls [50].

It is known that the Flory-Huggins parameter χ exhibits an inverse dependence on temperature, which could be incorporated in the simulation model. However, because CZA experiments maintain temperatures well below T_c, variations in χ are relatively unimportant compared with the highly temperature-dependent polymer mobility, particularly as the system transitions from below to above the glass transition temperature [35]. Therefore, in our simulations, the directional annealing front is modeled by prescribing a spatially- and temporally-dependent species mobility, M_A. Shown in Fig. 4.1, we utilize a smooth

functional form:

$$M_A = \frac{1}{2}\left[1 - tanh\left(\frac{6(x_i - x_f)}{w_{zone}}\right)\right] \quad (4.5)$$

where x_i is any x-position in the domain, w_{zone} is the width of the temperature transition zone, and $x_f = t \cdot \Delta t \cdot v_{zone} - 0.5 w_{zone}$ is the time-dependent x-position of the temperature transition zone (with t, Δt, and v_{zone} being the current time step, the time step size, and the zone velocity in the x-direction, respectively). The results presented below use a variety of values for v_{zone} and w_{zone}. Isothermally annealed results are modeled with a constant mobility having a value of $M_A = 1$.
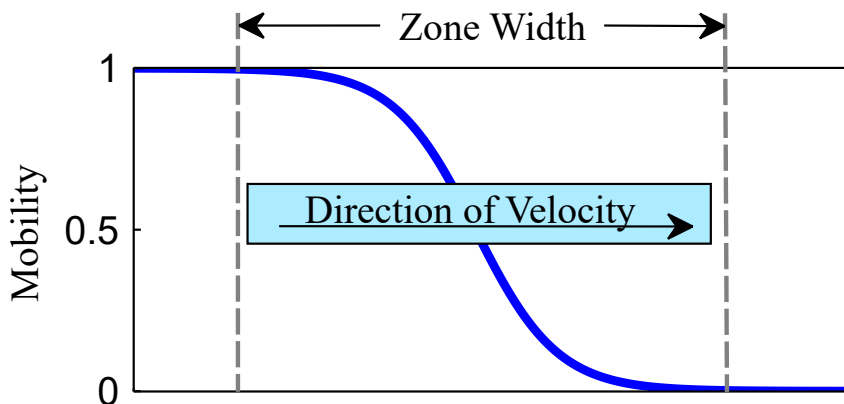

Figure 4.1: Simulations of zone annealing are performed with a spatiotemporal block copolymer mobility expressed in Eq. (5). As the thermal zone moves across the sample, the local mobility increases from values of zero to one.

We furthermore investigate how epitaxial templating and CZA together may synergistically enhance long-range order in block copolymer films. We introduce template stripes in the domains with a chemically favorable interaction with the B monomer. It should be noted that the preferential strength of chemical templating is key to the efficiency of chemo-epitaxy. For this work, templating is enforced for a very narrow stripe, much smaller than the lamellar period, such that attraction of polymer B is guaranteed in templated areas. This is modeled with a simple alteration of the short-range free energy functional that transforms

a double-well curve into a single-well curve:

$$F_S(\phi_A) = \psi \left[\phi_A^2(1 - \phi_A)^2 + \eta\phi_A^2\right] + \kappa|\Delta\phi_A|^2 \tag{4.6}$$

where η is a field variable that represents the locations of epitaxial alignment patterns ($\eta = 1$ inside a stripe pattern and $\eta = 0$ elsewhere).

We numerically solve Eq. (1) with a straightforward explicit finite difference scheme using a forward Euler time derivative and central difference approximations for spatial derivatives. The calculations utilized reduced units of length ($\tilde{l}$) and time ($\tilde{t}$). All simulations were conducted with two-dimensional grids with a uniform grid spacing of $\Delta x = \Delta y = 1\ \tilde{l}$. The time step size was kept fixed at $\Delta t = 0.03\ \tilde{t}$. The dimensions of the grids vary somewhat: for untemplated simulations a grid size of 2000×1000 was used, whereas for simulations with epitaxial stripe spacings of $L^T = 6\ L_0$ and $L^T = 7\ L_0$ grids of 1980×1020 and 2030×980 were used, respectively. Here, L_0 is the lamellar period length for the block copolymer measured to be $L_0 = 10\ \tilde{l}$ for energy parameters of $\psi = 1$, $\kappa = 1$, and $\alpha = 0.1$. Periodic boundary conditions are used in the y-direction and no-flux boundary conditions are enforced in the x-direction. Furthermore, the walls on the x-direction boundaries are chemically neutral with regards to the A- and B-blocks of the copolymer. Multiple zone velocities and zone widths were simulated, and the data points for each condition represent averages of 10 simulations with error bars indicating the standard error of the mean. Simulations are initialized independently as homogeneous solutions. The simulations were executed with parallel computing to enable large grid sizes and the large parameter space explored. Due to the nature of 2-dimensional simulations, the simulations presented here are effectively portraying a mono-layer thin-film which precludes the inclusion of out-of-plane defects and treats chemical striping as a through thickness alignment field as opposed to a local alignment field at the lower surface of the polymer melt.

In order to analyze how the zone velocity affects the final orientation of the BCP mi-

41

crodomains, we run each sample through a false color orientation algorithm that calculates the orientation of each sample between 0 and 180 degrees, which can be easily visualized as shown in Fig. 4.2. Orientation directions at grid points within the discretized system are calculated based on the gradient of ϕ_A at each point. The percent orientation of each sample to within ± 30 degrees of parallel and ± 30 degrees of perpendicular to the direction of the zone velocity (i.e. the x-direction) is then calculated.
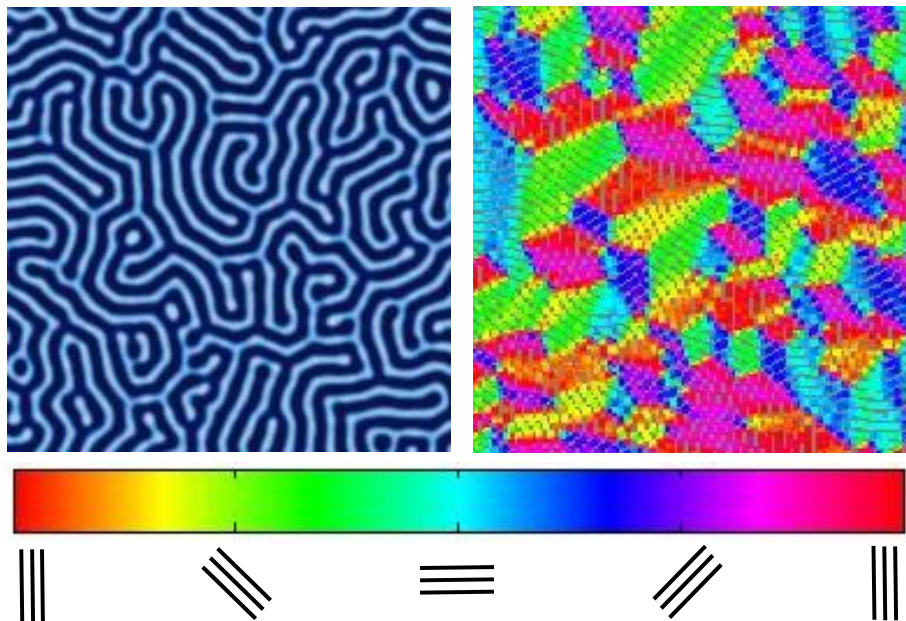

Figure 4.2: False-color imaging is used to show local lamellae orientation. The image here is obtained from an isothermally annealed simulation.

4.4 Results

4.4.1 CZA Simulation Results

Characteristic results for zone velocities in the range of $v_{zone} = 0.01 - 2.0$ (with units of $\tilde{l}/\tilde{t}$ which will hereto forth be omitted) and a fixed zone width $w_{zone} = 80 \ \tilde{l}$ are shown in Figs. 4.3 - 4.6 with the corresponding false color orientation fields. Orientation analysis of the simulation results shows behavior trends of the system as a function of zone velocity. Orientation percentages are plotted in Fig. 4.7 versus zone velocity, where velocity is plotted on a logarithmic scale. Considering the regions on the plot where one orientation (either

parallel or perpendicular) is above 97% alignment (see Supplemental Information – Section 1 for additional details), four distinct regions present themselves within the data. The mean orientation values are plotted and the standard error of the mean is represented by the shaded areas around each line.
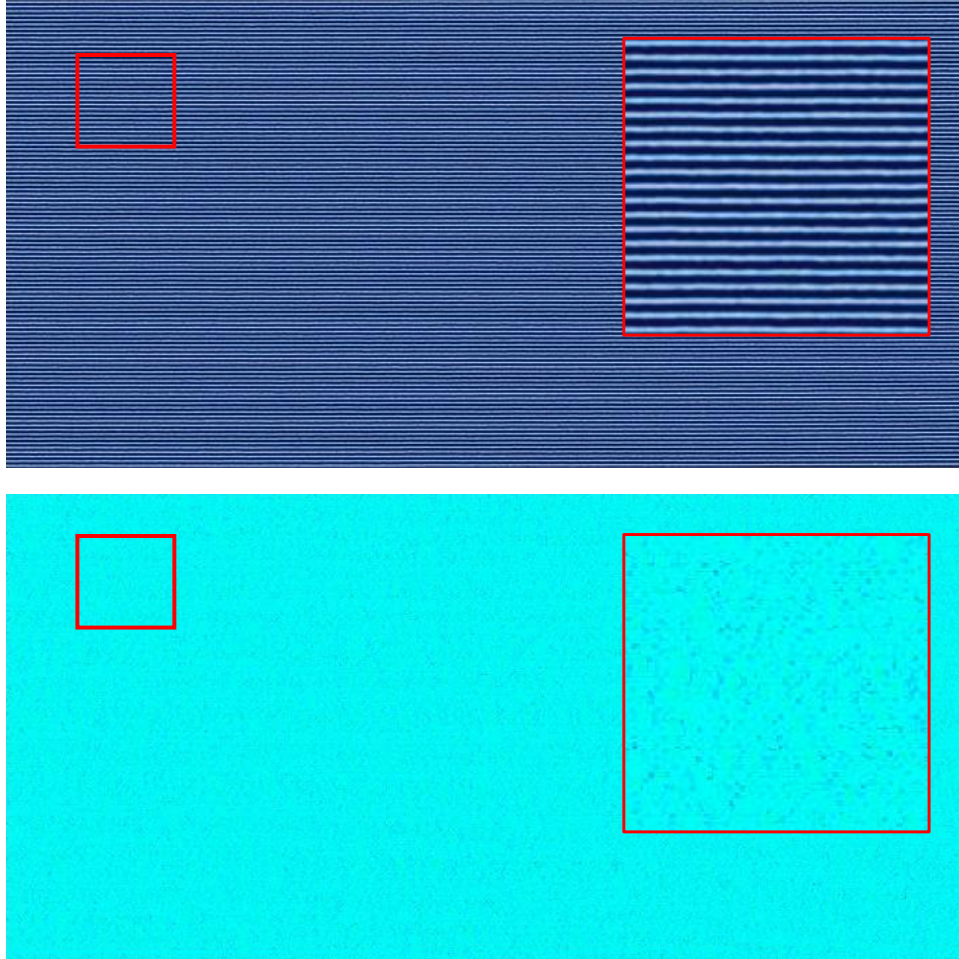

Figure 4.3: Snapshots of horizontally aligned lamellae obtained with a zone velocity of $v_{zone} = 0.0233$ and a zone width of $w_{zone} = 80 \ \tilde{l}$ without templating. The inhomogeneous mobility field moves from left to right across the domain – this image corresponds to the end of the simulation when the zone has moved across the entire sample. This sample contains no topological defects.

Region I is found at low velocities (see Fig. 4.7). In this region, the lamellae microdomains show a strong tendency to orient themselves parallel to the direction of the zone velocity. Simulation results in this region show little to no defects with minimal variability in the resultant structures. This parallel alignment was observed in CZA experiments at low zone
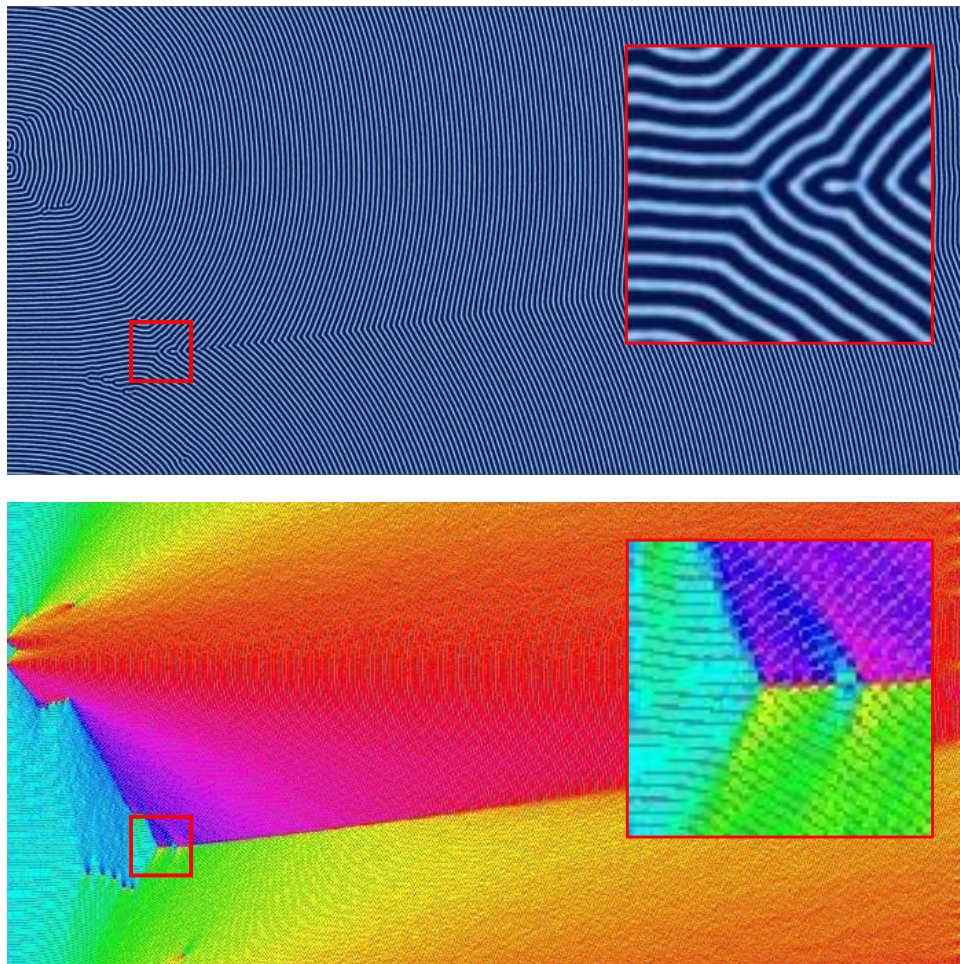
Figure 4.4: Same as Fig. 3 with a higher zone velocity of $v_{zone} = 0.0645$. Extended defects similar to grain boundaries emerge and generally extend from left to right in the direction of the zone translation.

velocities [32]. It is expected that further decreasing the zone velocity below the lower bound of our range will not produce noticeably different results. From a processing perspective, decreasing zone velocity is undesirable as it will increase annealing times. As zone velocity increases, we observe an interesting transition, whereby the BCP orientations shift from a parallel alignment to a perpendicular alignment with respect to the zone annealing direction. We designate this as Region II. In Region II, the transition appears to be steady on average, however with some variability as evidenced by the width of the error shading. With further increased zone velocity, the BCP alignment transitions to a nearly 100% perpendicular orientation, designated as Region III. For zone velocities in this region, it is only the far left
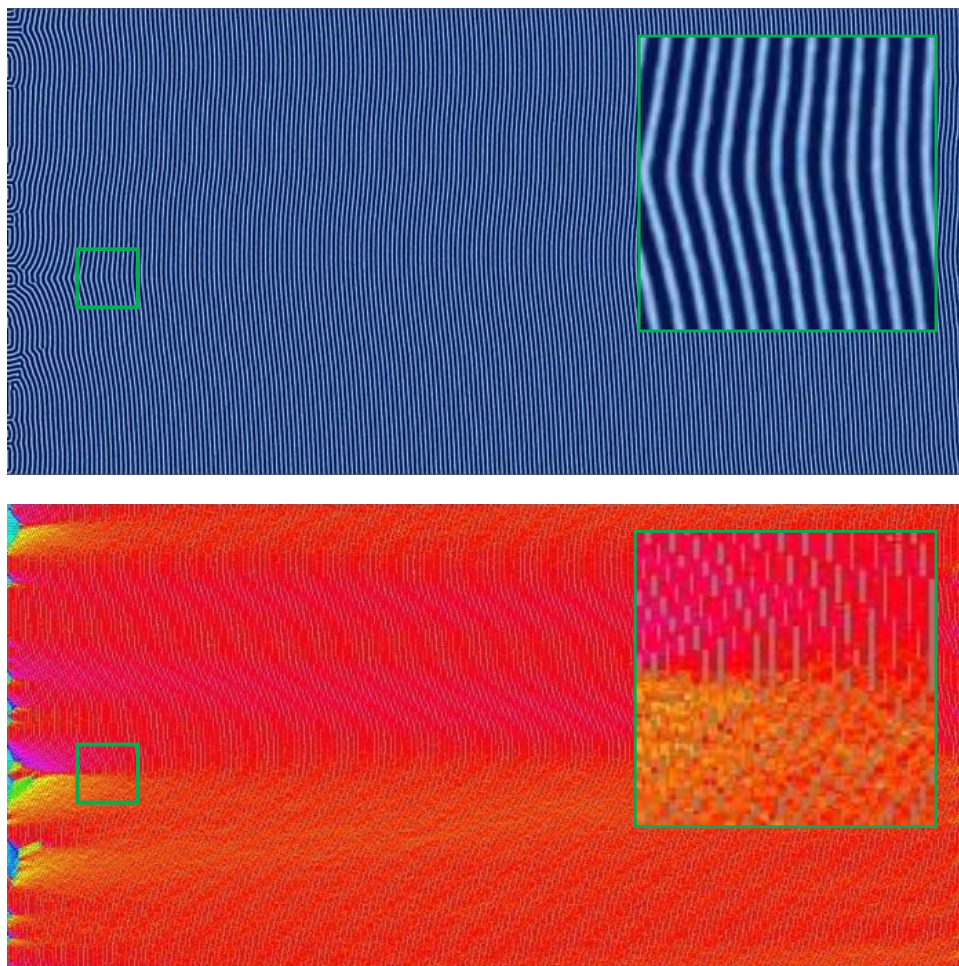
44

Figure 4.5: Same as Fig. 3 with a zone velocity of $v_{zone} = 0.2301$. A predominately perpendicular alignment has formed with the minor exception of the left boundary where the thermal zone enters the domain.

boundary of the computational domain, where the temperature zone first enters the domain, that exhibits some variation in alignment (see Fig. 5). However, in a very short distance, the BCP alignment becomes uniformly perpendicular as can be seen in the orientation plot of Fig. 5. With further increases in the zone velocity, the system exhibits decreased global alignment, as shown in Region IV, where the percent perpendicular and percent parallel alignment curves both approach 33%, which corresponds to their portion of the 180 degree range. In this region, the thermal front of the zone moves across the sample rapidly, and the results converge to those associated with isothermal annealing, and therefore the zone annealing process becomes ineffective as a directed self-assembly method.
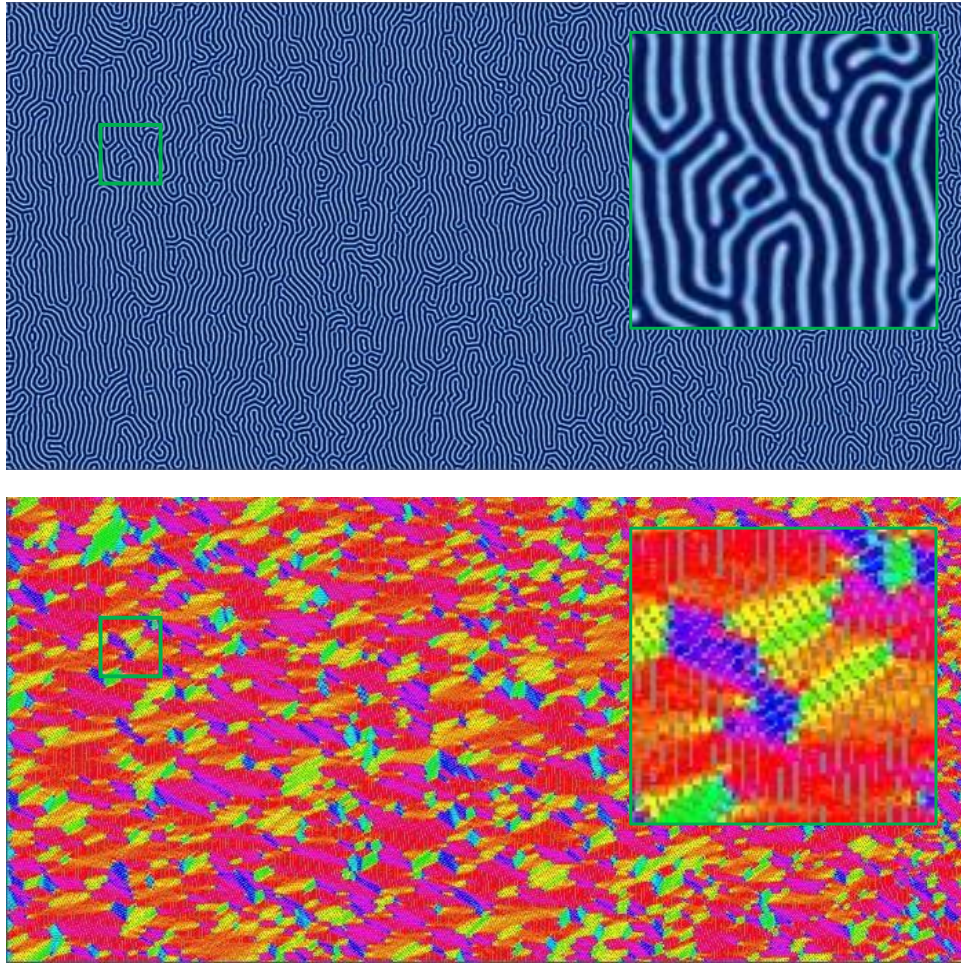
Figure 4.6: Same as Fig. 3 with a zone velocity of $v_{zone} = 0.6366$. Although the system contains some preference for perpendicular alignment, a significant quantity of defects exists at this velocity.
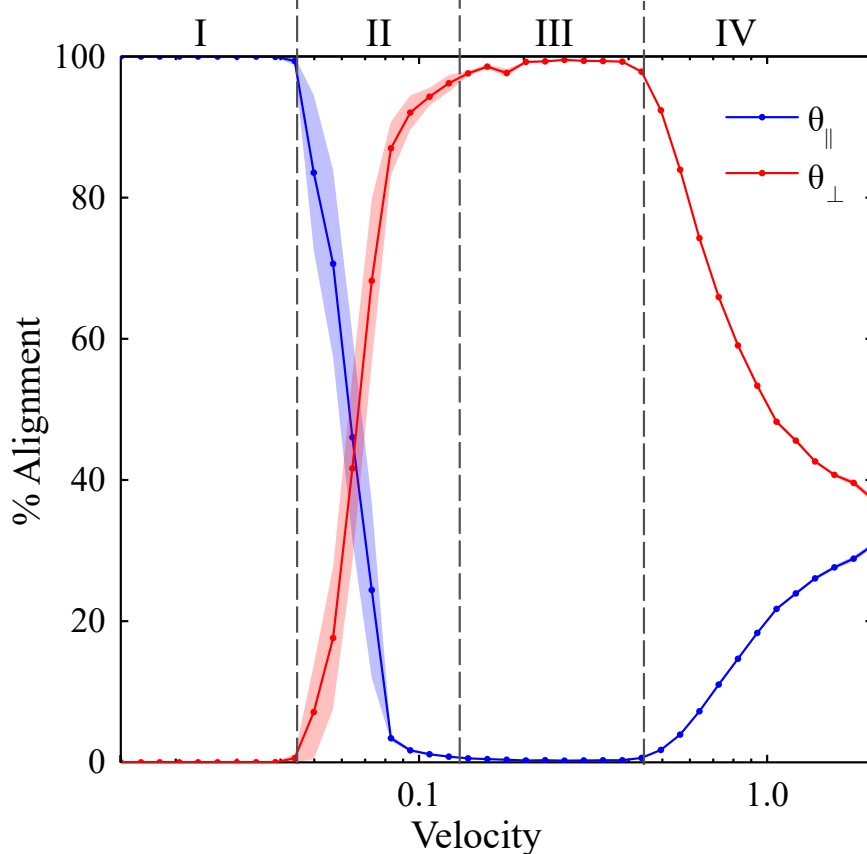
Figure 4.7: The percent alignment of lamellae to within ± 30 degrees of the directions parallel and perpendicular to the direction of zone velocity. The zone width is $w_{zone} = 80 \; \tilde{l}$. Four distinct regions emerge as a function of zone velocity: (I) parallel orientation, (II) transition from parallel to perpendicular orientation, (III) perpendicular orientation, and (IV) transition to unaligned orientations.

The surprising result in Fig. 4.7 is the range of velocities associated with Region III whereby a perpendicular alignment is strongly favored. This region was not directly reported in the CZA experiments of Berry et al. [32], although in personal correspondence Berry stated that some CZA experiments did result in a predominantly perpendicular alignment. On the other hand, the computational studies of Zhang et al. [30], Bosse et al. [35], and Cong et al. [47] all observed parallel as well as perpendicular alignment depending on the zone velocity. However, those studies only chose a limited number of velocities and a general trend was not obtained. The zone-casting experiments of Tang et al. [37] also revealed a tendency for either parallel or perpendicular lamella alignment depending on the casting temperature.

Interestingly, this phenomenon of phase alignment during directional phase separation is perhaps broader than BCP systems. In particular, theoretical [51] and experimental [52] studies show that binary polymer mixtures undergoing directional phase separation also exhibit phase alignment either parallel or perpendicular to direction of the moving thermal gradient. Furukawa [51] has proposed a convincing explanation stating that the concentration fluctuations in the early stage of phase separation may (or may not) be matched by the velocity of the thermal gradient that can lead to either parallel or perpendicular domains. It is remarkable that the patterns observed by Furukawa are so similar to the patterns observed here despite the fact that he simulated polymer-polymer phase separation (rather than BCP microphase separation) and he induced a moving quench boundary whereas we induce a moving mobility/annealing boundary.

It is necessary to consider how the zone width (and therefore the thermal gradient) plays a role in the alignment of the BCP system. For data shown in Fig. 4.7, a single zone width ($w_{zone} = 80 \ \tilde{l} = 8 \ L_0$) was used. In comparison to experimental testing, this represents a very sharp, perhaps unrealistic, thermal gradient. Taking this into consideration, simulations were repeated using larger zone widths of $w_{zone} = 160, 240, 500,$ and $1000 \ \tilde{l}$ in order to verify that the same trends appear with larger zone widths. Results for five simulations at each velocity are averaged and the transition velocities are compared in Fig. 4.8 (see Supplemental Information – Section 2 for additional details). For each of the zone widths explored, the same trend can be seen where increasing zone velocity induces a transition from parallel alignment to perpendicular alignment and then a transition to zero alignment. Increased zone width also necessitates longer simulation times as the simulations begin and end with the thermal zone entirely outside of the simulated sample. As seen in Fig. 4.8, as zone width increases, transition velocities decrease slightly; however, in all cases the system exhibited parallel orientations at low velocities, perpendicular orientations at intermediate velocities, and unaligned orientations for high velocities.
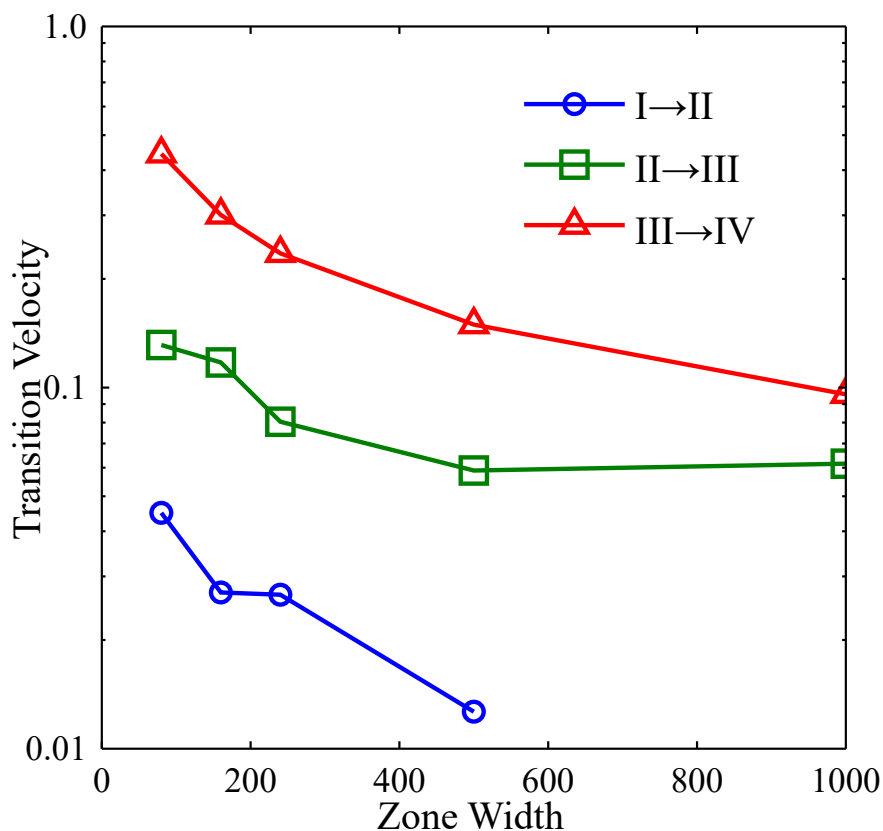
Figure 4.8: Transition velocities for Regions I-II, II-III, and III-IV as a function of the zone width, w_{zone}. The full data and a description of the approach to calculate these transitions is provided in the Supplemental Information.

4.4.2 Templated CZA Simulation Results

In order to explore the possible synergy between CZA and chemical templating, we performed additional simulations that combine the effects of both techniques to determine the extent to which templating will allow increases in the zone velocity while maintaining a negligible quantity of defects. A range of zone velocities were tested in systems that contained either horizontally- or vertically-aligned straight-line templates with template spacing ranging between 5 - 7 lamellar periods (or 50 - 70 $\tilde{l}$). Horizontal template stripes are parallel to the zone velocity, and their spacing is designated as $L_{\parallel}$, whereas vertical template spacing is designated as $L_{\perp}$. Data was collected by averaging five simulations at each of the twenty-five zone velocities tested. For simplicity, the domain size at each template spacing was adjusted

to fit both horizontal and vertical template patterns (i.e., the grid size must be an integer multiple of the template spacing).
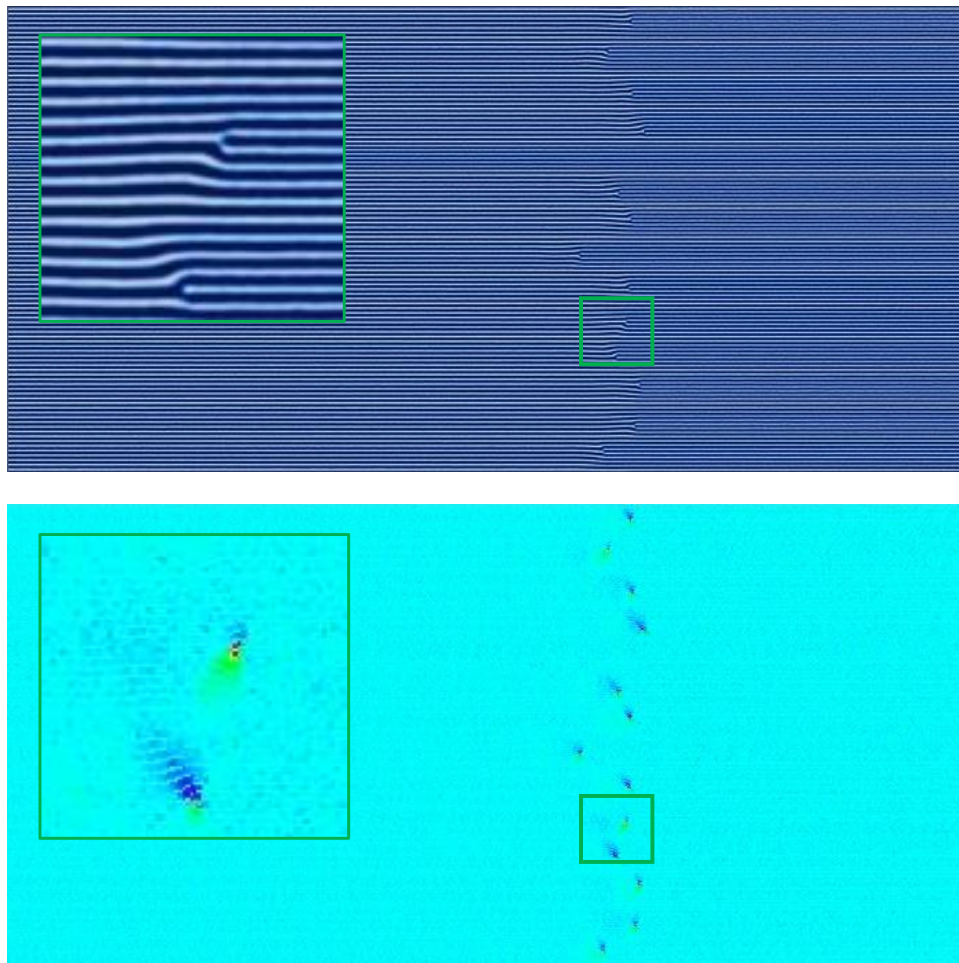

Figure 4.9: Simulation results for CZA with horizontal templating with a template spacing of $L_{\parallel} = 7\,L_o$ at a zone velocity of $v_{zone} = 0.103$. At this velocity, the alignment is predominantly parallel with a few dislocation-type defects.

For both horizontal and vertical templating patterns, we observed that the BCP morphology between adjacent template stripes was relatively unaffected by the morphology in the adjacent region. For domains with horizontal templating (i.e., parallel to the direction of the zone velocity), each of the regions of BCP orientation (i.e., Regions I, II, III, and IV) shift to higher velocities for each template spacing considered. In other words, faster velocities could be used to achieve the same percent alignment. Sample images of morphology from Regions I through III are shown respectively in Figs. 4.9 − 4.11 for a template spacing
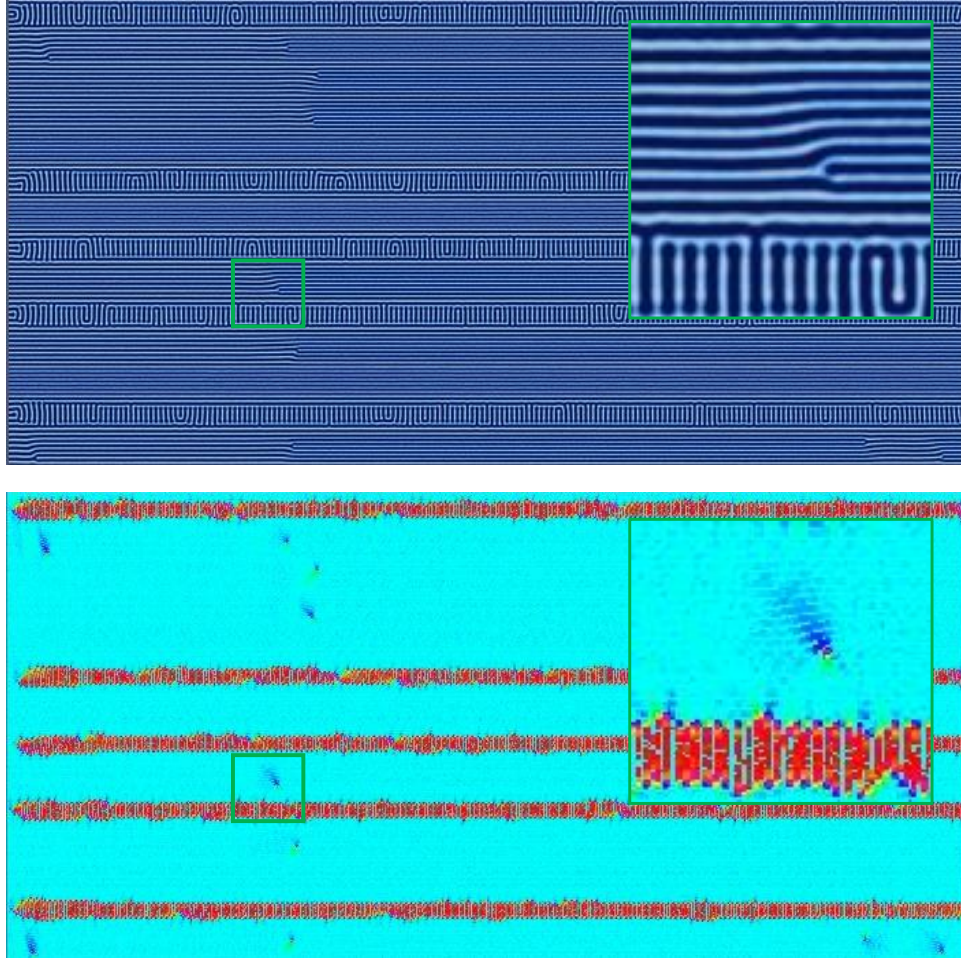
Figure 4.10: Same as Fig. 9 but with a zone velocity of $v_{zone} = 0.215$. At this velocity, the lamellae prefer a perpendicular orientation, which is restricted somewhat by the template pattern. A few bands of perpendicular lamellae develop between the template stripes.

of $L_{\parallel} = 7\ L_0$. In Fig. 4.9, the zone velocity is $v_{zone} = 0.103$, which in the untemplated simulations corresponded with Region III, however here the alignment is predominately parallel, although with several dislocation-type defects. When v_{zone} is increased to 0.215 (Fig. 4.10), the system enters a regime where the BCP formation strongly favors perpendicular alignment, but is frustrated by the parallel template pattern. We observe certain regions between template stripes forming perpendicular lamellae and others forming parallel lamellae. These horizontal 'bands' do not seem to be affected by neighboring 'bands'. These results are similar to those shown experimentally by Berry et al. [53] where periodic templating aligned parallel to zone velocity via graphoepitaxy is used to affect orientation. A further increase in
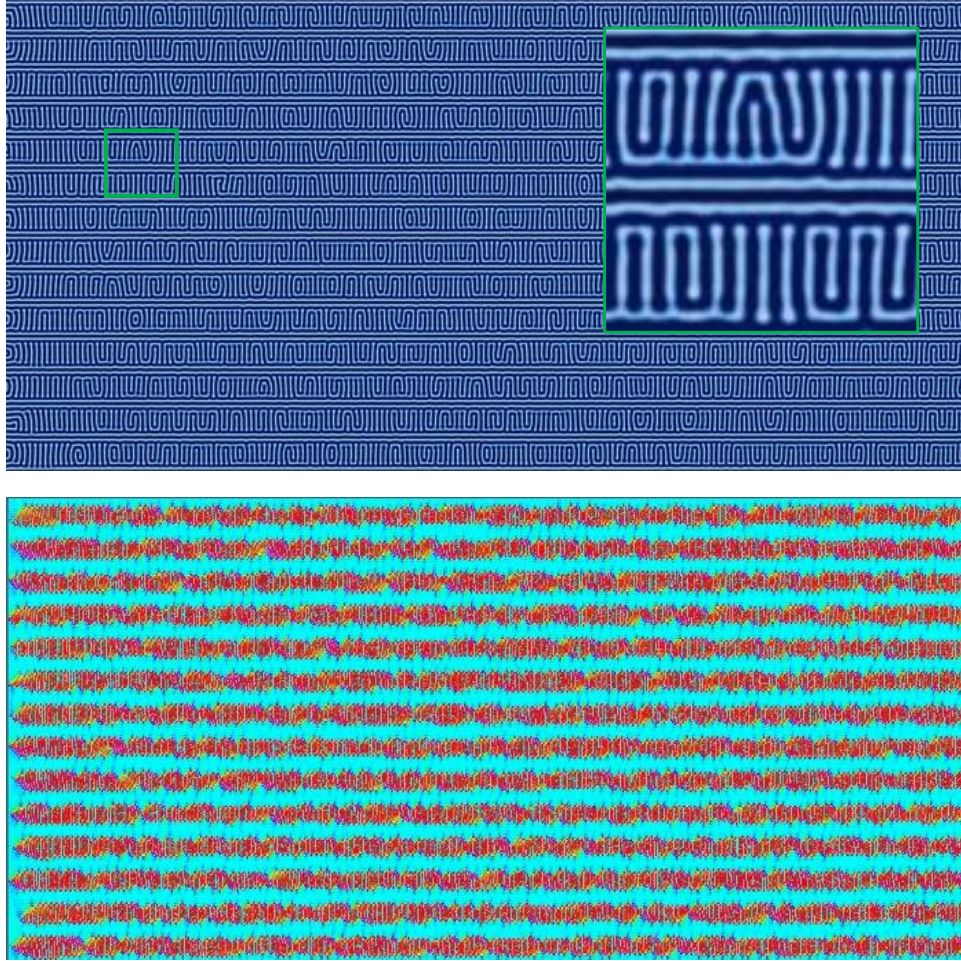
Figure 4.11: Same as Fig. 9 but with a zone velocity of $v_{zone} = 0.310$. At this velocity, the lamellae strongly prefer a perpendicular orientation, and all regions between the horizontal template patterns develop perpendicular lamellae bounded by parallel lamellae.

velocity to $v_{zone} = 0.310$ (Fig. 4.11) results in all regions between template stripes forming perpendicular alignment, separated by parallel lamellae directly overlapping the template stripes. Figure 4.12 plots the percent alignment data versus zone velocity for various values of $L_{\parallel}$. Of note, there is an increase in the velocity associated with a transition from parallel to perpendicular alignment.

Due to the observation that untemplated zone annealing favors perpendicular alignment over parallel alignment at intermediate-to-high velocities, it seems plausible that perhaps a perpendicular template pattern may be best for enabling increased zone velocities. We executed the same set of simulations with a perpendicular template pattern, which starts at
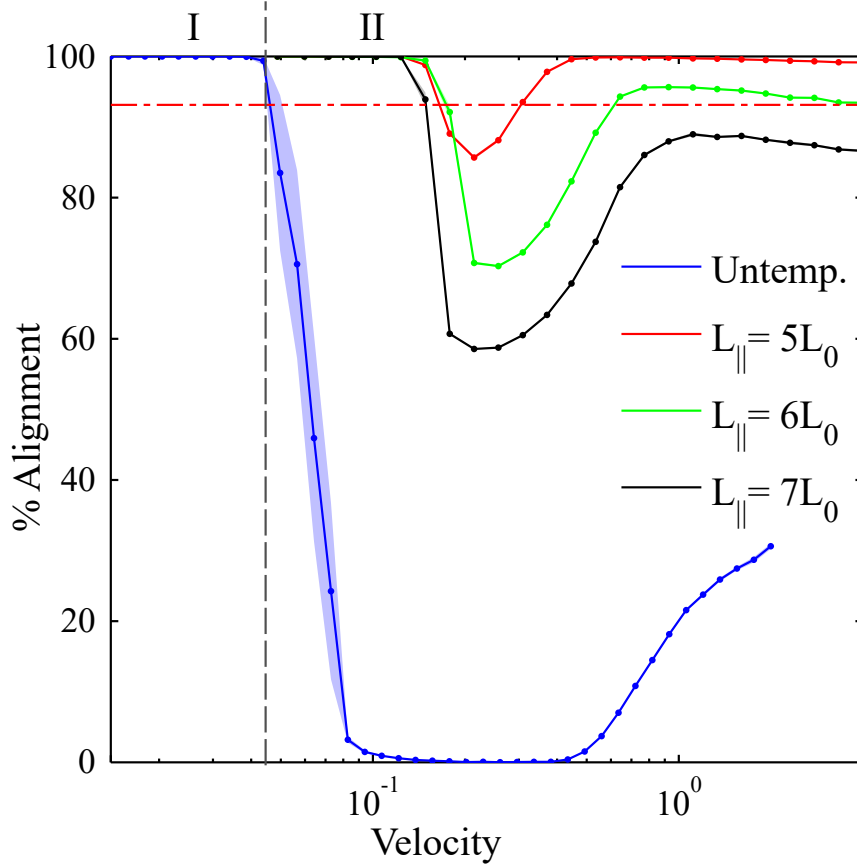
Figure 4.12: The percent alignment to within $\pm$ 30 degrees of the direction parallel to the zone velocity for samples with parallel (horizontal) template stripes. The zone width is w_{zone} = 80 $\tilde{l}$. A shift in the transition velocity from Regions I to II is observed due to the presence of the template stripes. For comparison, the horizontal line shows average alignment of isothermally annealed samples with templating at $L_{||} = 5L_0$ with annealing times equivalent to lowest velocity annealing times. Inset: template alignment (blue) is parallel to zone velocity (red).

the left boundary of the domain, where the temperature front enters the domain. As a result of this positioning, perpendicular orientation is strongly encouraged near the leading edge and the parallel orientations associated with Regions I and II do not emerge within the range of velocities tested (i.e., even with very low velocities, the alignment was perpendicular). Figure 4.13 shows the percent alignment for various values of perpendicular template spacing ($L_{\perp}$ = 5, 6, and 7 L_0). Region III appears to have its upper and lower limits extended to notably higher velocities, showing a larger range of velocities where perpendicular alignment occurs. The transition from Region III to Region IV occurs at the highest velocities for all cases
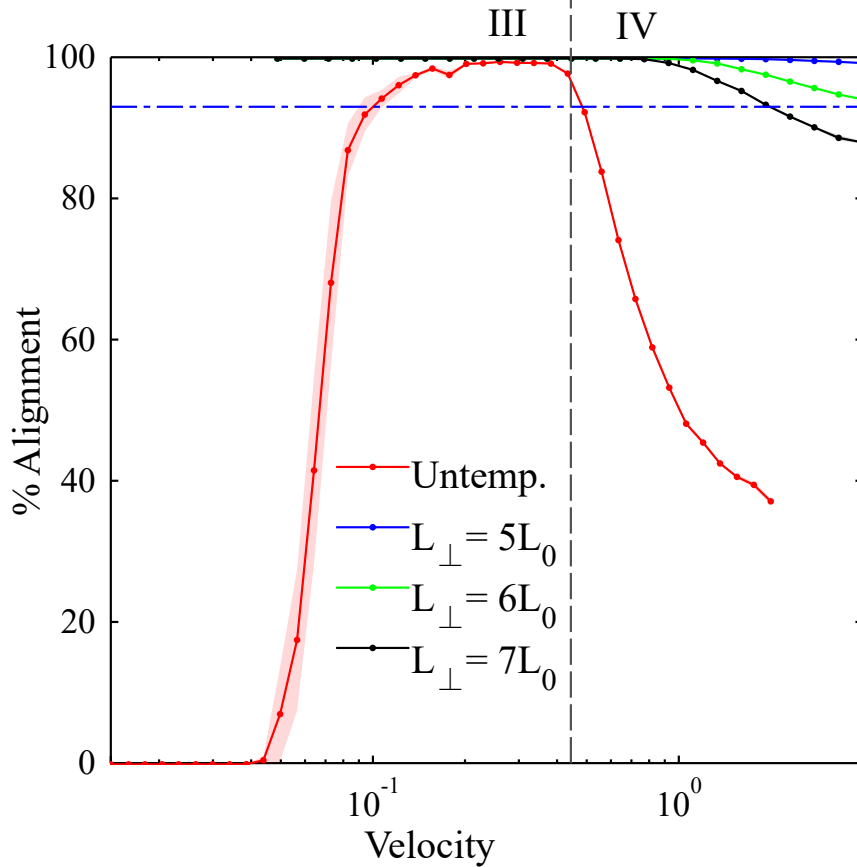
Figure 4.13: The percent alignment to within ± 30 degrees of the direction perpendicular to the zone velocity for samples with perpendicular (vertical) template stripes. The zone width is $w_{zone} = 80 \; \tilde{l}$. Perpendicular template stripes provide the greatest shift in zone velocities for defect-free lamellae morphologies. For comparison, the horizontal line shows average alignment of isothermally annealed samples with templating at $L_{\parallel} = 5L_0$ with annealing times equivalent to lowest velocity annealing times.Inset: template alignment (blue) is perpendicular to zone velocity (red).

tested here, with transition velocities exceeding $v_{zone} = 1.0$ which is several times higher than untemplated results. This therefore suggests that templating with periodic stripes oriented perpendicular to the direction of zone velocity is optimal for enhancing CZA alignment of BCP films. For comparison, figs. 4.12 and 4.13 show the average orientation for isothermally annealed samples with template spacing of $L_{\parallel} = 5L_0$. Annealing times for these samples are equivalent to the annealing time of lowest velocity samples annealed using CZA. Longer isothermal annealing times are expected to yield better alignment. While it is outside the scope of this work, it should be noted that for large samples, isothermal annealing may yield

equivalent results with equivalent processing times as CZA times are dependent on the zone velocity and dimension of the sample in the direction of zone annealing.

4.5 Conclusions

Large-scale numerical simulations have been performed to improve our understanding of CZA as a directed self-assembly strategy for BCP thin films. The orientation of lamellae is found to be highly dependent on the zone velocity, with subsequent transitions from parallel to perpendicular to unaligned orientations with increasing velocity. The width of the temperature zone, associated with the thermal gradient of the zone, was also studied and found to only slightly shift the transition regions, however with no qualitative change in the observed morphologies. We do point out that even our largest zone width is likely an order of magnitude below those formed in CZA experiments.

The combination of CZA and chemo-epitaxy can extend the range of velocities at which long-range orientational order can be achieved, a result that has implications for the efficient processing of nanopatterned surfaces. Here, we investigated linear stripe template patterns and found that template stripes oriented perpendicular to the zone velocity resulted in the greatest benefit for improving orientational order. This template orientation takes advantage of the natural tendency of the BCP microdomains to orient perpendicular to the zone velocity at intermediate-to-high velocities. We note that the two-dimensional domains employed in our simulations allowed larger sample regions, however, they prohibited the possibility of out-of-plane microdomain alignment.

Bibliography

[1] Mark Neisser and Stefan Wurm. Itrs lithography roadmap: 2015 challenges. *Advanced Optical Technologies*, 4(4):235–240, 2015.

[2] Wai-kin Li and Sam Yang. Creation of sub-20-nm contact using diblock copolymer on a 300 mm wafer for complementary metal oxide semiconductor applications.

[3] Hui Joon Park, Myung-Gyu Kang, and L Jay Guo. Large area high density sub-20 nm sio2 nanostructures fabricated by block copolymer template for nanoimprint lithography. *Acs Nano*, 3(9):2601–2608, 2009.

[4] Christopher Harrison, Miri Park, Paul M Chaikin, Richard A Register, and Douglas H Adamson. Lithography with a pattern of block copolymer microdomains as a positive or negative resist. ACS Publications, 1998.

[5] Mathieu Salaun, Marc Zelsmann, Sophie Archambault, Dipu Borah, Nikolaos Kehagias, Claudia Simao, Olivier Lorret, Matthew T Shaw, Clivia M Sotomayor Torres, and Mickael A Morris. Fabrication of highly ordered sub-20 nm silicon nanopillars by block copolymer lithography combined with resist design. *Journal of Materials Chemistry C*, 1(22):3544–3550, 2013.

[6] Mark P Stoykovich, Huiman Kang, Kostas Ch Daoulas, Guoliang Liu, Chi-Chun Liu, Juan J de Pablo, Marcus Müller, and Paul F Nealey. Directed self-assembly of block copolymers for nanolithography: fabrication of isolated features and essential integrated circuit geometries. *Acs Nano*, 1(3):168–175, 2007.

[7] Thomas Thurn-Albrecht, Rachel Steiner, Jason DeRouchey, Christopher M Stafford, Elbert Huang, Mustafa Bal, Mark Tuominen, Craig J Hawker, Thomas P Russell, et al. Nanoscopic templates from oriented block copolymer films. *Advanced Materials*, 12(11): 787–791, 2000.

[8] Michael J Fasolka and Anne M Mayes. Block copolymer thin films: physics and applications 1. *Annual Review of Materials Research*, 31(1):323–355, 2001.

[9] Dong-Po Song, Ying Lin, Yue Gai, Nicholas S Colella, Cheng Li, Xiao-Hui Liu, Samuel Gido, and James J Watkins. Controlled supramolecular self-assembly of large nanoparticles in amphiphilic brush block copolymers. *Journal of the American Chemical Society*, 137(11):3771–3774, 2015.

[10] Huibin Qiu, Zachary M Hudson, Mitchell A Winnik, and Ian Manners. Multidimensional hierarchical self-assembly of amphiphilic cylindrical block comicelles. *Science*, 347(6228):1329–1332, 2015.

[11] Frank S Bates, Marc A Hillmyer, Timothy P Lodge, Christopher M Bates, Kris T Delaney, and Glenn H Fredrickson. Multiblock polymers: panacea or pandora's box?

Science, 336(6080):434–440, 2012.

[12] Ludwik Leibler. Theory of microphase separation in block copolymers. *Macromolecules*, 13(6):1602–1617, 1980.

[13] AN Semenov. Contribution to the theory of microphase layering in block-copolymer melts. *Zh. Eksp. Teor. Fiz*, 88(4):1242–1256, 1985.

[14] Mark W Matsen and Michael Schick. Stable and unstable phases of a diblock copolymer melt. *Physical Review Letters*, 72(16):2660, 1994.

[15] EL Thomas, RL Lescanec, FC Frank, JS Higgins, A Klug, and IW Hamley. Phase morphology in block copolymer systems [and discussion]. *Philosophical Transactions of the Royal Society of London A: Mathematical, Physical and Engineering Sciences*, 348 (1686):149–166, 1994.

[16] Marc Hillmyer. Block copolymer synthesis. *Current Opinion in Solid State and Materials Science*, 4(6):559–564, 1999.

[17] Haizhou Yu, Xiaoyan Qiu, Suzana P Nunes, and Klaus-Viktor Peinemann. Self-assembled isoporous block copolymer membranes with tuned pore sizes. *Angewandte Chemie International Edition*, 53(38):10072–10076, 2014.

[18] Chiang-Jui Chu, Pei-Yun Chung, Mu-Huan Chi, Yi-Huei Kao, and Jiun-Tai Chen. Three-dimensional block copolymer nanostructures by the solvent-annealing-induced wetting in anodic aluminum oxide templates. *Macromolecular Rapid Communications*, 35(18):1598–1605, 2014.

[19] Gurpreet Singh, Kevin G Yager, Brian Berry, Ho-Cheol Kim, and Alamgir Karim. Dynamic thermal field-induced gradient soft-shear for highly oriented block copolymer thin films. *ACS Nano*, 6(11):10335–10342, 2012.

[20] Qiang Wang, Shyamal K Nath, Michael D Graham, Paul F Nealey, and Juan J de Pablo. Symmetric diblock copolymer thin films confined between homogeneous and patterned surfaces: Simulations and theory. *The Journal of Chemical Physics*, 112(22):9996–10010, 2000.

[21] Amitabha Chakrabarti and Hao Chen. Block copolymer films on patterned surfaces. *Journal of Polymer Science Part B: Polymer Physics*, 36(17):3127–3136, 1998.

[22] Christopher Harrison, Paul M Chaikin, David A Huse, Richard A Register, Douglas H Adamson, Abishai Daniel, E Huang, P Mansky, TP Russell, Craig J Hawker, et al. Reducing substrate pinning of block copolymer microdomains with a buffer layer of polymer brushes. *Macromolecules*, 33(3):857–865, 2000.

[23] Ion Bita, Joel KW Yang, Yeon Sik Jung, Caroline A Ross, Edwin L Thomas, and Karl K Berggren. Graphoepitaxy of self-assembled block copolymers on two-dimensional

periodic patterned templates. *Science*, 321(5891):939–943, 2008.

[24] Claudia M Duffy, Jens W Andreasen, Dag W Breiby, Martin M Nielsen, Masahiko Ando, Takashi Minakata, and Henning Sirringhaus. High-mobility aligned pentacene films grown by zone-casting. *Chemistry of Materials*, 20(23):7252–7259, 2008.

[25] Karl Amundson, Eugene Helfand, Don D Davis, Xina Quan, Sanjay S Patel, and Steven D Smith. Effect of an electric field on block copolymer microstructure. *Macromolecules*, 24(24):6546–6548, 1991.

[26] Karl Amundson, Eugene Helfand, XN Quan, Steven D Hudson, Steven D Smith, et al. Alignment of lamellar block-copolymer microstructure in an electric-field. 2. mechanisms of alignment. *Macromolecules*, 27(22):6559–6570, 1994.

[27] TL Morkved, M Lu, AM Urbas, EE Ehrichs, et al. Local control of microdomain orientation in diblock copolymer thin films with electric fields. *Science*, 273(5277):931, 1996.

[28] T Thurn-Albrecht, J DeRouchey, TP Russell, and HM Jaeger. Overcoming interfacial interactions with electric fields. *Macromolecules*, 33(9):3250–3253, 2000.

[29] F Ferrarese Lupi, TJ Giammaria, M Ceresoli, G Seguini, K Sparnacci, D Antonioli, V Gianotti, M Laus, and M Perego. Rapid thermal processing of self-assembling block copolymer thin films. *Nanotechnology*, 24(31):315601, 2013.

[30] Hongdong Zhang, Jianwen Zhang, Yuliang Yang, and Xuedong Zhou. Microphase separation of diblock copolymer induced by directional quenching. *The Journal of Chemical Physics*, 106(2):784–792, 1997.

[31] Jeffrey Bodycomb, Yoshinori Funaki, Kohtaro Kimishima, and Takeji Hashimoto. Single-grain lamellar microdomain from a diblock copolymer. *Macromolecules*, 32(6): 2075–2077, 1999.

[32] Brian C Berry, August W Bosse, Jack F Douglas, Ronald L Jones, and Alamgir Karim. Orientational order in block copolymer films zone annealed below the order- disorder transition temperature. *Nano Letters*, 7(9):2789–2794, 2007.

[33] Gurpreet Singh, Kevin G Yager, Detlef-M Smilgies, Manish M Kulkarni, David G Bucknall, and Alamgir Karim. Tuning molecular relaxation for vertical orientation in cylindrical block copolymer films via sharp dynamic zone annealing. *Macromolecules*, 45 (17):7107–7117, 2012.

[34] Kevin G Yager, Nathaniel J Fredin, Xiaohua Zhang, Brian C Berry, Alamgir Karim, and Ronald L Jones. Evolution of block-copolymer order through a moving thermal zone. *Soft Matter*, 6(1):92–99, 2010.

[35] August W Bosse, Jack F Douglas, Brian C Berry, Ronald L Jones, and Alamgir Karim.

Block-copolymer ordering with a spatiotemporally heterogeneous mobility. *Physical Review Letters*, 99(21):216101, 2007.

[36] Changhuai Ye, Yan Sun, Alamgir Karim, and Bryan D Vogt. Extending dynamic range of block copolymer ordering with rotational cold zone annealing (rcza) and ionic liquids. *Macromolecules*, 48(20):7567–7573, 2015.

[37] Chuanbing Tang, Wei Wu, Detlef-M Smilgies, Krzysztof Matyjaszewski, and Tomasz Kowalewski. Robust control of microdomain orientation in thin films of block copolymers by zone casting. *Journal of the American Chemical Society*, 133(30):11802–11809, 2011.

[38] RG Petschek and Haria Metiu. A computer simulation of the time-dependent ginzburg–landau model for spinodal decomposition. *The Journal of Chemical Physics*, 79(7): 3443–3456, 1983.

[39] Takao Ohta and Kyozi Kawasaki. Equilibrium morphology of block copolymer melts. *Macromolecules*, 19(10):2621–2632, 1986.

[40] Takeji Hashimoto. Time-dependent ginzburg-landau approach for microphase-separation kinetics of block polymers. *Macromolecules*, 20(2):465–468, 1987.

[41] Long-Qing Chen. Phase-field models for microstructure evolution. *Annual Review of Materials Research*, 32(1):113–140, 2002.

[42] Adam F Hannon, Yi Ding, Wubin Bai, Caroline A Ross, and Alfredo Alexander-Katz. Optimizing topographical templates for directed self-assembly of block copolymers via inverse design simulations. *Nano Letters*, 14(1):318–325, 2013.

[43] Jae-Byum Chang, Jeong Gon Son, Adam F Hannon, Alfredo Alexander-Katz, Caroline A Ross, and Karl K Berggren. Aligned sub-10-nm block copolymer patterns templated by post arrays. *Acs Nano*, 6(3):2071–2077, 2012.

[44] QH Zeng, AB Yu, and GQ Lu. Multiscale modeling and simulation of polymer nanocomposites. *Progress in Polymer Science*, 33(2):191–269, 2008.

[45] Vinay Raman, Arijit Bose, Bradley D Olsen, and T Alan Hatton. Long-range ordering of symmetric block copolymer domains by chaining of superparamagnetic nanoparticles in external magnetic fields. *Macromolecules*, 45(23):9373–9382, 2012.

[46] Li-Tang Yan and Xu-Ming Xie. Computational modeling and simulation of nanoparticle self-assembly in polymeric systems: Structures, properties and external field effects. *Progress in Polymer Science*, 38(2):369–405, 2013.

[47] Zhinan Cong, Liangshun Zhang, Liquan Wang, and Jiaping Lin. Understanding the ordering mechanisms of self-assembled nanostructures of block copolymers during zone annealing. *The Journal of Chemical Physics*, 144(11):114901, 2016.

[48] Ian W Hamley. Cell dynamics simulations of block copolymers. *Macromolecular Theory and Simulations*, 9(7):363–380, 2000.

[49] Travis H Russell, Brian J Edwards, and Bamin Khomami. Characterization of the flory-huggins interaction parameter of polymer thermodynamics. *EPL (Europhysics Letters)*, 108(6):66003, 2015.

[50] Maria Serral, Marco Pinna, Andrei V Zvelindovsky, Josep Bonet Avalos, et al. Cell dynamics simulations of sphere-forming diblock copolymers in thin films on chemically patterned substrates. *Macromolecules*, 2016.

[51] Hiroshi Furukawa. Phase separation by directional quenching and morphological transition. *Physica A: Statistical Mechanics and its Applications*, 180(1-2):128–155, 1992.

[52] Jin Okinaka and Qui Tran-Cong. Directional phase separation of a binary polymer mixture driven by a temperature gradient. *Physica D: Nonlinear Phenomena*, 84(1-2):23–30, 1995.

[53] Brian C Berry, Gurpreet Singh, Ho-Cheol Kim, and Alamgir Karim. Highly aligned block copolymer thin films by synergistic coupling of static graphoepitaxy and dynamic thermal annealing fields. *ACS Macro Letters*, 2(4):346–350, 2013.

Chapter 5

Paper 2: Directed Self-Assembly in Diblock Copolymer Thin Films for Uniform Hemisphere Pattern Formation

Co-Author: Paul C. Millett

5.1 Abstract

Directed self-assembly of block copolymers has shown to be an effective bottom-up approach to creating periodic nano-scale surface patterns. This work offers a computational study of sphere-forming polystyrene-block-poly(methyl methacrylate) (PS-b-PMMA) block copolymer thin-film behavior. A temperature dependent optimized phase-field model is implemented for simulations. Directed self-assembly using a combination of cold-zone annealing and chemoepitaxial templating is performed. It is shown that synergy between these methods can enhance long-range order within the evolving system during micro-phase separation and that templated patterns can propagate indefinitely into untemplated regions when the system undergoes low-velocity cold-zone annealing.

5.2 Introduction

The continuing demand for smaller feature sizes in surface patterns requires constant refinement of existing and emerging technologies. Block copolymers (BCP) remain heavily studied due to their potential applications for creating desirable nano-scale surface features [1–5]. Most commonly studied are linear di-block copolymers which will spontaneously micro-phase separate and form a number of distinct periodic morphologies depending on their chain architecture and applied thermodynamic conditions [6]. Applied as thin films, these regular morphologies can be used as a sacrificial templating layer in the photolithography process [7]. However, defects occur during phase separation and a directing method is required to enhance ordering and to create long-range regular patterns. Block copolymer lithography has enabled long-range patterning of feature sizes that have not been available to traditional

photolithography [8, 9] and offers a number of advantages and challenges compared to other nanoscale patterning approaches [10, 11]. As a bottom-up process, the micro-phase separation of BCPs drives the patterning process as opposed to top-down approaches which rely on the resolution of the lithographic tools [12]. While the range of stable morphologies is somewhat limited, the benefit of low-cost high-throughput processing over large areas is very appealing to industry needs [8]. A variety of directed self-assembly (DSA) techniques have been applied to enhance long-range order in BCP systems [8, 9]. One group of these methods involves the application of a moving thermal gradient to induce order during directional annealing.

Application of a thermal gradient has been studied for some time and has shown to be a practical method to induce order within a BCP film. The concept of a moving front inducing phase separation within a BCP system was numerically studied in 1-dimension by Liu and Goldenfeld [13] and in 2- and 3-dimensions by Paquette [14]. Similarly, Furukawa numerically studied directional quenching in 2-dimensions [15]. Together, these studies suggest that enhanced ordering can be attained by such a thermal treatment. Two-dimensional simulations with a shifting quench boundary by Zhang et al. [16] support the previous results and furthermore reveal that lamellae orientation is dependent on the quench boundary velocity. From these initial numerical works, Hashimoto et al. [17] developed a zone annealing experimental method that involved passing a BCP thin film through a series of temperature zones at a constant velocity. This process was designed to raise the temperature of the BCP from below the order-disorder temperature, T_{OD}, to above T_{OD} and back below again in a sequential manner. In these experiments, the thermal gradient was on the order of $\nabla T \approx 30°C/mm$. The phase separation process occurred along the cooling edge of the thermal zone, as the temperature dropped back below T_{OD}. Hashimoto et al. showed that ∇T affects the orientation and ordering of lamellae-forming BCPs during the ordering process which agrees with the previous numerical work. Berry et al. [18] modified this process to limit the hot-zone temperature to a value below T_{OD}, dubbing the method "cold-zone

annealing" (CZA) [19–21], and re-terming the process by Hashimoto et al. as "hot-zone annealing" (HZA). During the CZA process, a similar ∇T was applied as temperatures were raised from below the glass transition temperature, T_g, to a value above T_g (but not above T_{OD}). Unlike with HZA, the phase separation process occurs at the heating edge of the thermal zone during CZA processing. Cold-zone annealing is also advantageous for some BCPs because it avoids potential material degradation that can occur at temperatures near or above T_{OD}. Computational modeling (including our previous work) of HZA and CZA has shown agreement with the close relationship between zone velocity and the orientation and ordering of BCP systems [22–26]. Majewski and Yager [27] increased ∇T with the implementation of laser zone annealing (LZA), which used a focused laser to produce sharp thermal gradients, $\nabla T \approx 3000°C/mm$, which are significantly sharper than those used in HZA and CZA [28].

Other DSA methods which rely on thermal gradients include zone casting [29, 30] and directional solidification [31–34]. Tang et al. introduced a BCP zone casting [29, 30] method which shapes heated BCP thin-films through extrusion onto a substrate. Similar to HZA, zone casting occurred at a constant velocity and ordering was enhanced along a long narrow region as cooling occurred where $\nabla T \approx 30°C/mm$. Directional solidification [31] has also proven beneficial as an alignment method by applying a lower thermal gradient, $\nabla T \approx 10°C/cm$, to solidify a heated BPC in a confined crystallizable solvent. Unlike unidirectional solvent methods [32–34], the thermal gradient induced a directional crystallization of the solvent layer during which BCP micro-domains were aligned with the direction of solidification. Combining thermal gradient treatments with other DSA strategies has shown synergistic improvements in the degree of BCP long-range ordering. Singh et al. [35] showed that the combination of CZA and shear alignment, termed "CZA-soft shear" could increase the viable velocities available compared to CZA alone. Epitaxial templating [36–43] is a method where physical or chemical features placed on the substrate guide BCP evolution during micro-phase separation. Berry et al. [44] and Xue et al. [45] have shown that synergy

exists between zone annealing and templating methods.

The effectiveness of CZA to enhance ordering for cylinder-forming [18–21] and lamellae-forming [23–26] BCPs has been considered in a number of studies, however, application of CZA on sphere-forming BCPs remains largely overlooked in favor of cylinder- and lamella-forming morphologies. By studying the behavior of these systems, new methods may be discovered to enhance the application of BCP lithography and extend the knowledge base as a whole. In our previous work [25], we have shown synergy between chemoepitaxial templating and CZA for generalized lamellar BCPs utilizing a 2-dimensional large-scale time-dependent Ginzburg-Landau model. In this paper, sphere-forming PS-b-PMMA BCP thin films are studied via a 3-dimensional optimized phase-field model. Chemoepitaxial templating and CZA are applied and it is shown that enhanced ordering can be achieved for sphere-forming PS-b-PMMA thin films through the combination of these processing methods. It is shown that film thickness, template spacing, zone velocity, and zone width all play a role in the ordering process and can affect the overall order and structure of the metastable final state of the system. It is also shown that epitaxial templating limited to one region of the system can initiate BCP ordering that can then be propagated into non-templated regions. For low-velocity CZA, order propagation can occur over relatively long distances.

5.3 Methods

The model implemented for this work considers an idealized AB diblock copolymer film where unequal volume fractions, ϕ, of the A and B monomers may be implemented (i.e. $\phi_A \neq \phi_B$). An Optimized Phase-Field (OPF) model, developed by Liu et al. [46] is implemented. This model converges commonly used phase-field [47–50] and self-consistent field theory [23, 51, 52] (SCFT) models. The OPF model uses a free energy functional obtained via a strategic mapping of the Ohta-Kawasaki [47] model with a more accurate, and computationally more expensive, SCFT model [53]. The OPF model is computationally less expensive than SCFT, but predicts similar morphologies and defect energetics. The OPF model has also been shown to not suffer nonphysical behavior near confining walls that other models have experienced

[54]. Our simulations are developed to mimic experiments in which a BCP thin film is spin-coated as a disordered layer between two parallel surfaces that confine the film. The system is assumed to be devoid of solvent and incompressible and, therefore, obeys the condition $\phi_A + \phi_B = 1$. Accordingly, we consider only one independent volume fraction, e.g. ϕ_A. The computational method represents non-isothermal conditions by calculating a local, temperature-dependent Flory-Huggins interaction parameter, χ:

$$\chi(T_i) = \beta + \frac{\alpha}{T_i} \tag{5.1}$$

where α and β are material properties which represent entropic and enthalpic contributions to χ respectively, and T_i is a local temperature. Kinetic evolution is captured by spatially and temporally updating ϕ_A using a Cahn-Hilliard-Cook equation:

$$\frac{\partial \phi_A}{\partial t} = \nabla \cdot \left(M_A \nabla \frac{\delta F(\phi_A)}{\delta \phi_A} \right) + \xi(\mathbf{r}, t), \tag{5.2}$$

where the mobility of monomer A is represented by M_A and is assumed to be equal to M_B (a reasonable assumption for materials such as PS-b-PMMA), $F(\phi_A)$ represents the free energy functional which describes the chemical energy of mixing between monomer species, and $\xi(\mathbf{r}, t)$ approximates normalized random noise which is spatially averaged to zero with a range of $\xi = \pm 0.001$ at each time step. Global conservation of ϕ_A is ensured by Eq. (5.2).

The free energy functional, $F(\phi_A)$, consists of both short- and long-range terms:

$$F(\phi_A) = F_S(\phi_A) + F_L(\phi_A), \tag{5.3}$$

where a polynomial expression combined with a gradient term describes the short-range

chemical mixing energy:

$$F_S(\phi_A) = \int [c_2(\delta\phi_A)^2 + c_3(\delta\phi_A)^3 + c_4(\delta\phi_A)^4$$
$$+ c_5|\nabla\phi_A|^2]d\mathbf{r} \tag{5.4}$$

where $\delta\phi_A = \phi_A - 0.5$. The first three terms represent a double-well potential curve that produces a miscibility gap within the range of $\phi_A = 0$ and $\phi_A = 1$. The fourth term penalizes gradients in ϕ_A that occur at A-B interfaces. The OPF model coefficients c_2, c_3, c_4, and c_5 influence the mixing energy, thus relating χ and the degree of polymerization, N, with the diffuse width of the A-B interface. The long-range term in the free energy functional penalizes domain growth and reflects limitations due to the physical attachment of the A and B chains, and is defined by:

$$F_L(\phi_A) = c_6 \int d\mathbf{r} \int d\mathbf{r}' G(\mathbf{r} - \mathbf{r}')\phi_A(\mathbf{r})\phi_A(\mathbf{r}') \tag{5.5}$$

where the Green function $G(\mathbf{r} - \mathbf{r}')$ satisfies $\nabla^2 G(\mathbf{r} - \mathbf{r}') = -\delta(\mathbf{r} - \mathbf{r}')$. While developed to describe bulk BCP systems, this version of the Green function does not show significant deviation near solid boundaries [55]. Coefficients $c_2 - c_6$ are defined in detail by Liu et al. [46] and they depend on the parameters χN and f (the fraction of A monomers on the BCP chain).

For CZA simulations, the directional annealing front is modeled by implementing a spatiotemporal local temperature, T_i, which transitions from T_{min} to T_{max} with a smooth transition numerically expressed as:

$$T_i = T_{min} + \frac{1}{2}\left[1 - tanh\left(\frac{6(x_i - x_f)}{w_{zone}}\right)\right] \cdot (\Delta T) \tag{5.6}$$

where x_i is the local x-position within the domain, w_{zone} describes the temperature transition zone width, $\Delta T = T_{max} - T_{min}$, and x_f represents the location of the center of the annealing

66

front tracked by

$$x_f = N_{steps} \cdot \Delta t \cdot v_{zone} - \frac{1}{2} w_{zone} \tag{5.7}$$

with N_{steps} representing the current simulation step number and v_{zone} representing the velocity of the moving thermal zone in the x-direction. It is worth noting that thermal diffusion is negligible at this scale and temperature is treated as only a function of the x-direction. As temperature transitions from below to above T_g of the BCP, local mobility, M_A, is modeled by the diffusion rate which scales linearly with temperature for a polymer melt by the Stokes-Einstein relation where $D \propto T$ [56, 57]. Because diffusive activity does not occur below T_g, it is only necessary to simulate temperatures at or above T_g, therefore $T_{min} \approx T_g$ is applied so that $M_A = 0$ when $T_i = T_{min}$ and $M_A = 1$ when $T_i = T_{max}$ modeled by:

$$M_A = \frac{1}{2} \left[1 - tanh \left(\frac{6(x_i - x_f)}{w_{zone}} \right) \right]. \tag{5.8}$$

In some results below, we simulate isothermal annealing in which case a constant mobility is used having a value of $M_A = 1$ at a constant temperature $T = T_{max}$.

In BCP morphologies, domain spacing L_0 is determined by χN and f. For sphere-forming BCPs, L_0 represents the separation distance between the centers of nearest-neighbor spheres. In our model, due to the confinement between the two parallel surfaces, the emerging morphology is a two-layer array of hemispheres in contact with the top and bottom surfaces, as shown in Fig. 1. To simulate chemoepitaxial templating, a periodic dot template is introduced on the lower substrate below the simulation domain. Circular templated areas are designated where the template diameter is smaller than the BCP spherical domain diameter which attracts the minority monomer species (in our case, A). Figure 5.1 shows a cross-sectional diagram of the BCP film with accompanying surfaces. In some of our simulations, slight discrepancies between the template spacing, L_s, and L_0 occur due to the fact that the lateral x- and y-dimensions are periodic. Gadelrab et al. [58] have shown that BCP systems are tolerant to variations below $|L_s - L_0| < 0.1 L_0$, which is true in the simulations presented
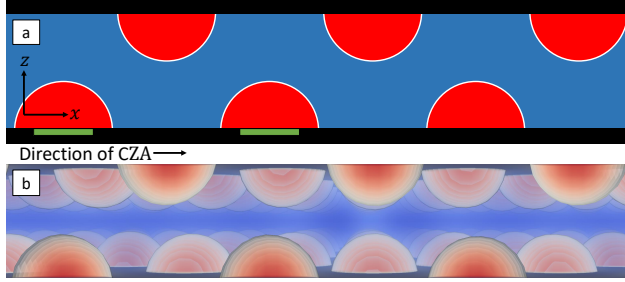
here.

Figure 5.1: a) A schematic illustrating a side-on view of the BCP film confined between upper and lower surfaces (black). Chemoepitaxial templating is applied on the bottom surface (green) as small patches with diameter less than the spherical domain diameter. The minority monomer A (red) is attracted to the templating patches. b) An example simulation showing the hemispherical arrays that form within the film. In this image, the majority monomer B (blue) is colored slightly transparent to show depth.

Simulations are executed by numerically solving Eq. (5.2) using standard explicit finite-difference approximations, with reduced units for time ($\tilde{t}$) and length ($\tilde{l}$). The domain is discretized with three-dimensional grids with uniform grid spacing of $\Delta x = \Delta y = \Delta z = 1\ \tilde{l}$. The time step size is fixed at $\Delta t = 0.00002\ \tilde{t}$. Simulations are initialized with a spatially-averaged polymer concentration $\bar{\phi}_A = 0.32$ with variability of ± 0.05. For PS-b-PMMA, $T_g \approx 378$K. In CZA experiments, temperature ranges of 313K$\leq T \leq$ 473K have been used [18]. In this work, the experimental upper temperature is repeated while lower temperature is just below T_g, i.e. temperatures for CZA simulations range between $T_{min} = 373$K and $T_{max} = 473$K as shown in Fig. 5.2. The translating thermal zone enters from the left side and transitions across the simulation domain until exiting, after which $M_A = 1$ and $T = T_{max}$ throughout and isothermal annealing occurs. The BCP is simulated with a degree of polymerization $N = 385$ and a Flory-Huggins parameter of $\chi = 0.036$ at $T = T_{max}$, consistent with sphere forming PS-b-PMMA where $\alpha = 3.9$ and $\beta = 0.028$ in Eq. (5.1) [59]. The average domain spacing for un-templated simulations is measured at $L_0 = 15.18\ \tilde{l}$ and a minimum template spacing of $L_s = 15\ \tilde{l}$ is applied and tested with results shown below. In the x-direction, periodic boundary conditions are applied for isothermal simulations, and a no-flux boundary is applied for CZA simulations. Periodic boundary conditions are used

in the y-direction and a no-flux boundary conditions are enforced in the z-direction. No-flux boundaries are treated as chemically neutral surfaces with regards to the A- and B-blocks of the copolymer except where templating is applied. Except where noted, $w_{zone} = 50 \ \tilde{l}$.
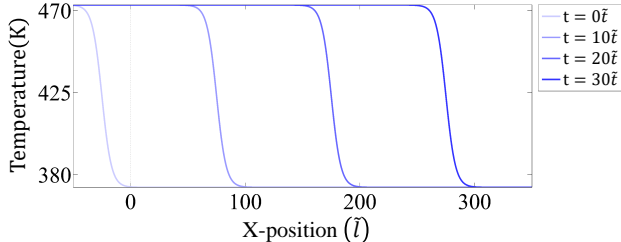

Figure 5.2: CZA simulations apply a spatiotemporal temperature expressed in Eq. (5.6). Shown, $v_{zone} = 10 \ \tilde{l}/\tilde{t}$ and $w_{zone} = 50 \ \tilde{l}$. Simulations are initialized with the thermal transition zone outside of the simulation domain. As time progresses, the thermal zone moves throughout the sample at a prescribed velocity.

For films where the film thickness is smaller than the domain spacing, small variations in thickness have a large impact on the stable morphologies. Figure 5.3 shows simulations of varying thickness which are isothermally annealed at $T = 473$K. As shown, the morphology is dependent on the film thickness. Films that are too thin such as Fig. 5.3(a) develop cylinder-shaped defects which align vertically and contact both surfaces, while films that are too thick such as Fig. 5.3(c,d) exhibit spheres formed between the surfaces. A film thickness of $z = 11 \ \tilde{l}$ (Fig. 5.3(b)) is selected for this study and is used throughout. The selected thickness allows for bi-layer hemisphere formation along the upper and lower surfaces where each layer directly impacts the evolution of the other. Thicker films where mid-plane sphere formation occurs prevents this and adversely affects the effectiveness of chemical templating. Also of note, due to thickness restrictions, hemispheres in this range of film thickness have a tendency to self-assemble into a square-array pattern rather than a hexagonal-array pattern that are found in thicker film or bulk systems. Similar results were also shown by Serral et al [55]. As shown in Fig. 5.4, orientation analysis of the BCP films was performed using Delaunay triangulation and a cell orientation algorithm on the top-surface of the domain.

For analysis purposes, data from only the upper surface of the simulation is considered.

Concentration is normalized to values between $\phi_A = 0$ and $\phi_A = 1$. Data below a set threshold are removed, for this work, threshold was set to $\phi_{A_{min}} = 0.85$ which reveals concentration clusters near the center of each upper hemisphere. Each cluster is analyzed to identify the local maxima which are recorded as grid points. To ensure that multiple clusters are not grouped together, the local maxima search is limited to a diameter equal to the BCP separation distance L_0. Delaunay triangulation [58, 60] is performed on the set of points to determine nearest neighbors. Finally, each set of delaunay neighbors are treated as a unit cell and the largest distance across the cell is calculated. This distance vector is compared to the direction of zone velocity and the angle between is calculated and assigned as θ to the node at the center of each cell where θ has values between $\theta = +90°$ and $\theta = -90°$. For visualization purposes, orientation is interpolated across the simulation space to create an orientation map using periodic bounds for θ.
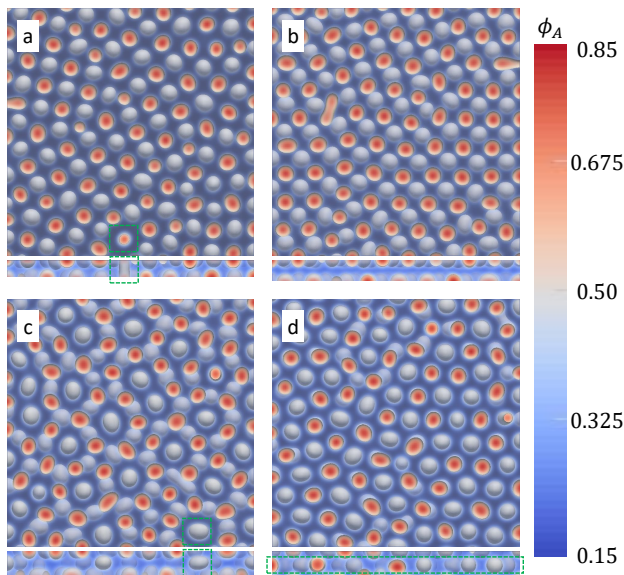

Figure 5.3: Comparison of thin-film morphologies with varying film thickness. Isothermal annealing is simulated at $T = 473K$ for a duration of $70\ \tilde{t}$. Simulation size $128\ \tilde{l} \times 128\ \tilde{l}$ with varying thicknesses: a) At $z = 9\ \tilde{l}$, vertical defects contact both surfaces. b) At $z = 11\ \tilde{l}$, hemispheres form on upper and lower surfaces with no through-thickness defects. c) At $z = 13\ \tilde{l}$, irregular sphere defects form between the upper and lower surfaces. d) At $z = 15\ \tilde{l}$, a regular layer of spheres form midway between the upper and lower surfaces.
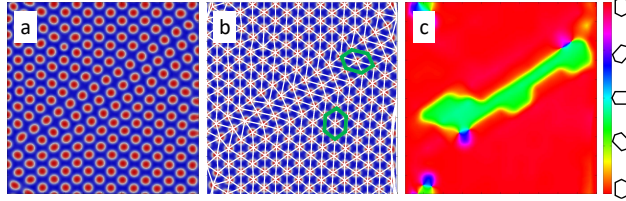
Figure 5.4: The orientation analysis method used to determine ordering within the BCP system. a) Only the upper (un-templated) surface of each simulation is analyzed for ordering. b) Local maxima are located and Delaunay triangulation is used to calculate nearest neighbors which determine the cell surrounding each maxima. Two representative cells are highlighted (green). c) Orientation of each cell is calculated and assigned. False color images are created by interpolating between orientations of the maxima.

5.4 Results

Large scale thin-film simulations, shown in Fig. 5.5, illustrate the phase separation process in an isothermally annealed BCP. The initial phase separation process involves a nucleation and growth mechanism, visible in Fig. 5.5(a), which is dependent on the randomly initialized concentration of ϕ_A and the random thermal noise, $\xi(\mathbf{r}, t)$. This initial phase separation leads to rapid development of short range order with grain boundaries and defects, Fig. 5.5(b,c). Over prohibitively long times, these defects can be removed with isothermal annealing. By applying chemoepitaxial templating, CZA, or a combination of both methods, long-range order may be induced much faster and with greater uniformity.

To determine an appropriate templating scheme, templating is applied in both square and rectangular patterns where spacing in the x- and y-directions are unequal, i.e. $L_{sx} \neq L_{sy}$. Shown in Fig. 5.6, the strong chemical preference induces rapid phase separation in templated areas on the substrate. Templated areas reinforce the desired architecture as the surrounding BCP thin-film undergoes spontaneous phase separation. Each templating scheme has a direct impact on the final morphology of the simulation and can affect the presence of grain defects in the system. For tested templating schemes defect-free ordering is observed in as little as $4.2\,\tilde{t}$ for some schemes while others did not produce defect-free results within reasonably long simulation times. In Fig. 5.6(a), the template spacing is equal to the natural sphere-sphere spacing L_0 which leads to a perfectly-ordered morphology. Various
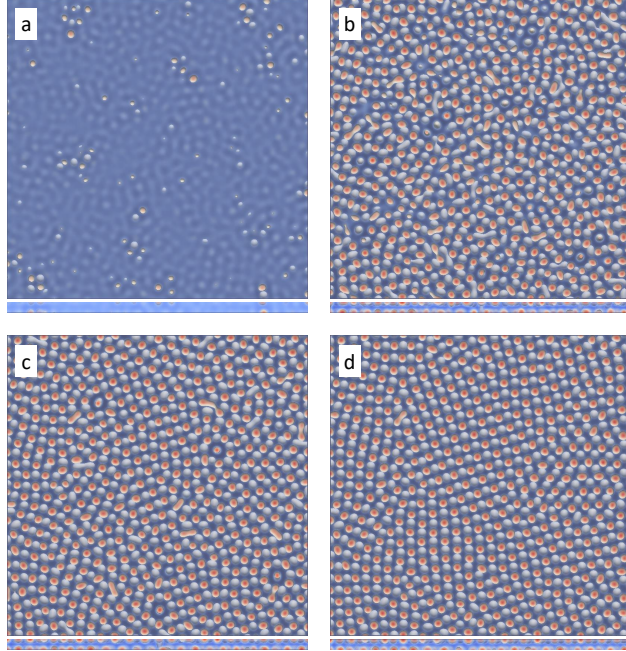
Figure 5.5: Time evolution of a simulated sphere-forming BCP thin film with untemplated isothermal annealing. Simulation size is $300\,\tilde{l} \times 300\,\tilde{l} \times 11\,\tilde{l}$. Isothermal annealing is simulated at $T = 473\text{K}$. Simulation space is initialized with $\phi_A = 0.32 \pm 0.05$. a) At $t = 2.10\,\tilde{t}$, unique phases appear as spontaneous phase separation occurs. b) $t = 3.50\,\tilde{t}$. c) $t = 17.5\,\tilde{t}$. d) At $t = 70.0\,\tilde{t}$, the presence of defined grains with grain boundaries and defects can be observed.

other template patterns with greater spacing in the x- and/or y-direction were tested, as shown in Fig. 5.6(b-f). In general, we observe that for good ordering to occur, the template spacing in at least one direction must be less than $2L_0$. Thus, as a DSA approach, templating alone would require a large number density of templating features to eliminate defects and control ordering.

We now investigate the effectiveness of CZA on BCP ordering in the absence of templating. Simulations implementing CZA are initialized with the moving thermal zone outside of the simulation domain such that the initial mobility is negligible throughout the simulation, i.e. $M_A \approx 0$ throughout. The moving thermal zone enters from the left side and transitions in the x-direction until exiting the simulation and isothermal annealing continues. Simulations implementing CZA using $v_{zone} = 10.0\,\tilde{l}/\tilde{t}$ are shown in Fig. 5.7. We observe an overall improvement in long-range order compared with the isothermally annealed results
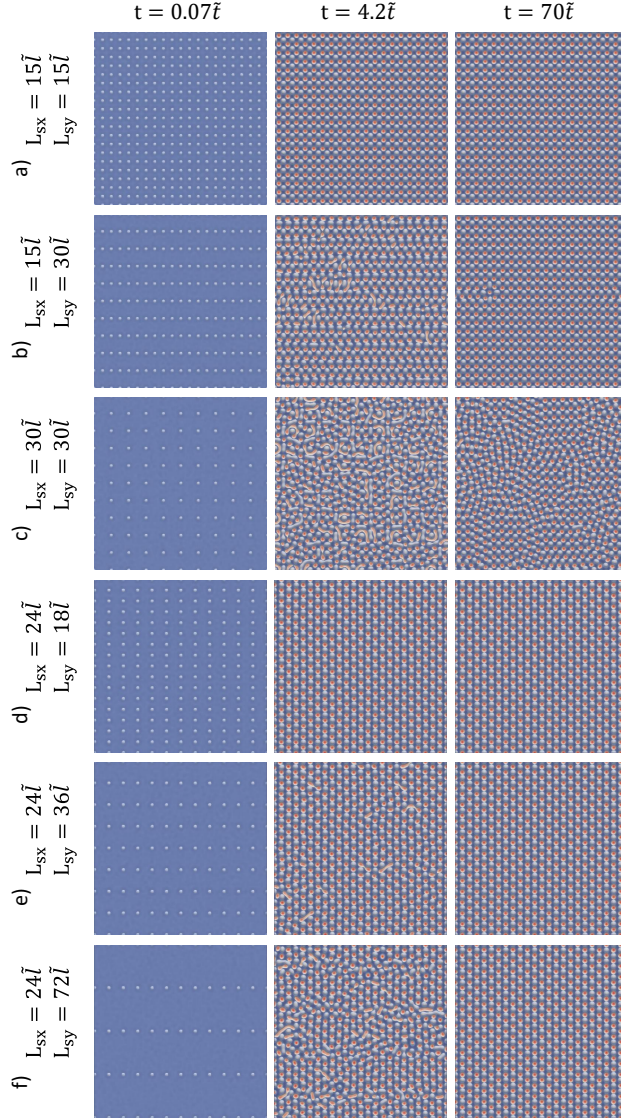
Figure 5.6: Time evolution of a simulated sphere-forming BCP thin-film with chemoepitaxial templating. Simulation sizes are: (a-c) 300 $\tilde{l} \times 300$ $\tilde{l}$ and (d-f) 288 $\tilde{l} \times 288$ $\tilde{l}$ with film thickness of 11 $\tilde{l}$. Templating occurs below the lower surface of the simulation with a template spacing of: a) $L_{sx} = 15$ $\tilde{l}$, $L_{sy} = 15$ $\tilde{l}$ b) $L_{sx} = 15$ $\tilde{l}$, $L_{sy} = 30$ $\tilde{l}$ c) $L_{sx} = 30$ $\tilde{l}$, $L_{sy} = 30$ $\tilde{l}$ d) $L_{sx} = 24$ $\tilde{l}$, $L_{sy} = 18$ $\tilde{l}$ e) $L_{sx} = 24$ $\tilde{l}$, $L_{sy} = 36$ $\tilde{l}$ f) $L_{sx} = 24$ $\tilde{l}$, $L_{sy} = 72$ $\tilde{l}$. Templating diameter is 4 $\tilde{l}$. At $t = 0.07$ $\tilde{t}$, templated regions are apparent as phase separation is induced. At $t = 4.2$ $\tilde{t}$: some template schemes (a and d) enforce rapid phase separation with perfect order while others show defect-laden or under-developed regions. At $t = 70.0$ $\tilde{t}$: stable equilibrium shows defect-free morphologies (a,d-f) while defects (b) and grain boundaries (c) can be seen in simulations where template spacing is too large.

(Fig. 5.5(d)) with an equivalent runtime of 70.0 $\tilde{t}$. However, some defects still remain in the system. Based on our observation, these defects typically develop at the left-hand side

of the domain where the thermal zone enters. As phase separation begins in this region, it does not occur uniformly. This can be seen in Fig. 5.7(a). Any non-uniformities that exist on this leading edge of the domain ultimately lead to some defect features further along the x-direction. This behavior has been observed for velocities as low as $1.0\ \tilde{l}/\tilde{t}$ and is attributed to the non-uniform phase separation at the leading edge and not a result of the zone velocity.
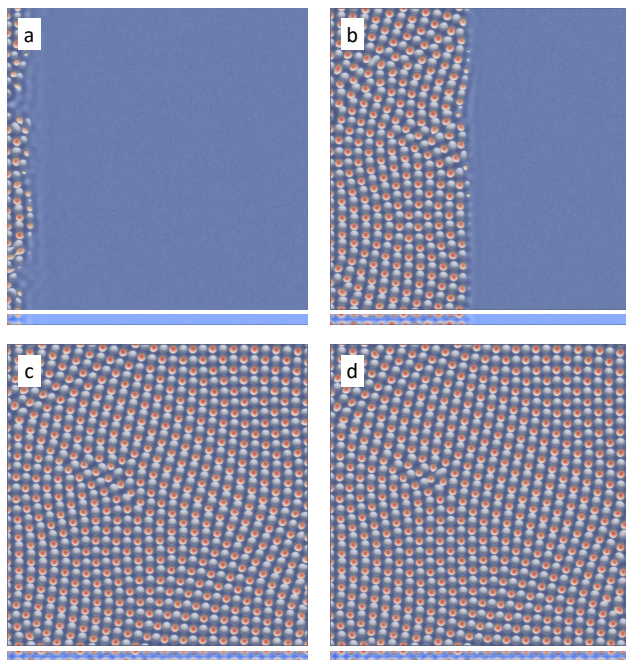

Figure 5.7: Time evolution of a simulated sphere-forming BCP thin-film with CZA. Simulation size is $300\ \tilde{l} \times 300\ \tilde{l} \times 11\ \tilde{l}$, $v_{zone} = 10\ \tilde{l}/\tilde{t}$, $w_{zone} = 50\ \tilde{l}$. a) At $t = 7.0\ \tilde{t}$, phase separation begins as the thermal zone moves into the simulation space. b) At $t = 17.5\ \tilde{t}$, phase separation occurs rapidly within a narrow region as the thermal zone moves through the simulation. c) At $t = 35.0\ \tilde{t}$, isothermal annealing occurs after the thermal zone has passed out of the simulation space. d) At $t = 70.0\ \tilde{t}$, some defects are relaxed during isothermal annealing.

Simulations combining both chemoepitaxial templating and CZA show significant improvement in the overall ordering of the system. Figure 5.6 shows that full-domain templating can quickly achieve perfect ordering of the BCP system. To test the enhancement of CZA by application of chemoepitaxial templating, only a minimal amount of templating is desired. Our previous work has shown that for lamellae-forming BCP, line templating perpendicular to the direction of CZA can optimally extend order within the system [25]. Based on our observation above that defects arise due to non-uniformities on the leading edge of

the simulation where the thermal zone enters, we strategically place only a minimal amount of templating at this location to test how far templating can extend order into un-templated regions during CZA. A double-column arrangement of templating patches are placed on the left-hand side of the domain to enforce the intended morphological orientation (a single-column arrangement of patches was not found to be as effective). Shown in Fig. 5.8(a), templated regions are placed in two regular columns with spacing in the x- and y-directions of $L_{sx} = 24\,\tilde{l}$ and $L_{sy} = 18\,\tilde{l}$ respectively. Under isothermal, full-domain template conditions this scheme offers rapid phase separation into a highly ordered morphology (shown in Fig. 5.6(d)). Applied as a narrow column along the edge of the simulations where the translating thermal zone enters, this templating scheme similarly produces rapid initial ordering of the system.

As the moving thermal zone transverses the simulation domain, previously evolved hemi-spheres act as a template for developing regions within the thermal zone. At low velocities, this regular pattern can propagate throughout the entire un-templated region of the simulation domain. At higher velocities, order does not establish rapidly enough causing a higher rate of defect formation. Once a defect has been established, the pattern propagation quickly breaks down and subsequent development within the system is disordered. After analysis, the orientation of each cell is compared with a vector in the y-direction, representative of perfect alignment. Cells with orientation to within a tolerance of $\pm 15°$ are considered to be well ordered, others are flagged as a defect location. Results from a series of simulations have been analyzed to compare the zone velocity and the defect-free CZA distance, which is the distance measured between the initial templating and the inception of defects within the system. Results are shown in Fig. 5.9. Simulations with different x- and y-dimensions are shown. As v_{zone} decreases, the defect-free CZA distance increases rapidly, therefore simulations of increasing length are necessary. Results where the defect-free CZA distance is equal
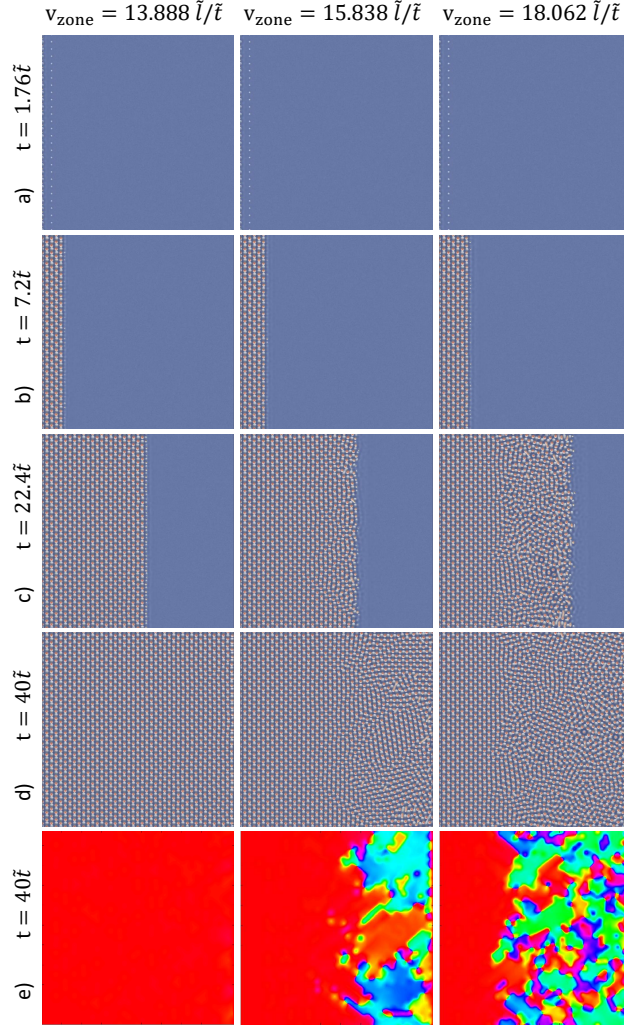
Figure 5.8: Time evolution of simulated BCP thin films with templating applied near the y-axis where the CZA thermal zone enters the simulation domain. Three velocities are compared; $v_{zone} = 13.888\ \tilde{l}/\tilde{t}$, $v_{zone} = 15.838\ \tilde{l}/\tilde{t}$, and $v_{zone} = 18.062\ \tilde{l}/\tilde{t}$. Simulation size is $480\ \tilde{l} \times 480\ \tilde{l} \times 11\ \tilde{l}$. Templating is applied only as two columns with $L_{sx} = 24\ \tilde{l}$ and $L_{sy} = 18\ \tilde{l}$. a) At $t = 1.76\ \tilde{t}$, the templated region induces rapid micro-phase separation as the thermal zone enters the simulation space. b) At $t = 7.2\ \tilde{t}$, the ordered area behind the thermal zone acts as a template for phase-separating region. c) At $t = 22.4\ \tilde{t}$, the self-templating behavior propagates throughout the entire system until defects appear. d-e) At $t = 40.0\ \tilde{t}$, defects within the system halt the self-templating behavior. e) Orientation mapping is used to visualize the defect-free CZA distance.

to the simulation width are omitted. Resultant data is fit to the asymptotic function

$$f(v_{zone}) = \frac{a \cdot v_{zone} + b}{v_{zone} + c} \tag{5.9}$$

in Fig. 5.9 which shows that the defect-free CZA distance approaches infinity as decreasing velocity approaches $v_{zone} \approx 13.4 \ \tilde{l}/\tilde{t}$. Previous CZA studies have shown that there is a correlation between zone velocity and the orientation and ordering of BCP systems [16–18, 22–26]. Here, the orientation is predetermined by the initial templating scheme that is applied. Similar to lamellae-forming BCP studies, a strong correlation exists between CZA zone velocity and long-range ordering, measured by the defect-free CZA distance. In comparison with the un-templated CZA results shown in Fig. 5.7 where $v_{zone} = 10 \ \tilde{l}/\tilde{t}$ is applied, perfect order can be achieved for the shown domain size at $v_{zone} \approx 15 \ \tilde{l}/\tilde{t}$ when minimal templating is applied.

Comparison between these results and our previous work [25] with lamella-forming BCPs show that in general, BCP self assembly can be directed via CZA and that process can be enhanced via epitaxial templating. Both systems are highly sensitive to changes in zone velocity and template spacing. Unlike with lamella-forming BCPs, there does not appear to be a shift in orientation with increasing zone velocity that have been noted by others [16, 18, 25]. There also appears to be a preferential elongation of template spacing that occurs in sphere-forming BCPs which tend to evolve into short-range square arrayed patterns under isothermal annealing [55].

For all results presented above, a zone width of $w_{zone} = 50 \ \tilde{l}$ is applied. The zone width directly corresponds to the temperature gradient, or rate of temperature increase per unit distance, which can vary greatly between experimental setups and type of DSA method used. Temperature gradients common to CZA are on the order of $10 - 70°C/mm$ while laser zone annealing can reach maximum temperature gradients of $4000°C/mm$ [27]. It is therefore important to compare how the defect-free CZA distance will change with increasing w_{zone} values. Figure 5.10 shows comparative results for zone widths of $50 \ \tilde{l}$, $100 \ \tilde{l}$, $150 \ \tilde{l}$, and $500 \ \tilde{l}$. As the thermal zone width increases, micro-phase separation occurs over a wider region within the thermal gradient zone. We see that increasing w_{zone} results in a decreasing defect-free CZA distance. The asymptotic velocity values are $v_{zone} = 11.84 \ \tilde{l}/\tilde{t}$, $11.55 \ \tilde{l}/\tilde{t}$,
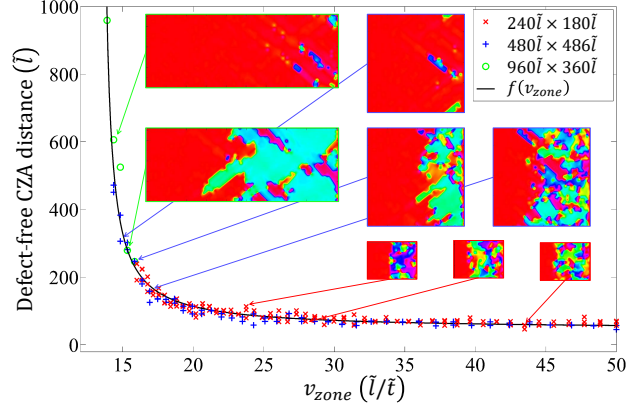
Figure 5.9: The defect-free CZA distance versus the CZA zone velocity for simulations such as the ones shown in Fig. 5.8. As indicated, three different domain sizes were utilized to collect data whereby the larger size was needed for smaller v_{zone}. Results where the defect-free CZA distance is equal to the simulation width (i.e., perfect order within the domain) are omitted. Representative false-color orientation maps are inset to show comparative sizes of simulations at varying values of defect-free CZA distances. Data is fit to the function $f(v_{zone}) = (a \cdot v_{zone} + b)/(v_{zone} + c)$ resulting in $a = 44.25$, $b = -180.4$, and $c = -13.37$ with a coefficient of determination $R^2 = 0.9978$.

and 7.836 $\tilde{l}/\tilde{t}$ respectively for $w_{zone} = 100$ $\tilde{l}$, 150 $\tilde{l}$, and 500 $\tilde{l}$.
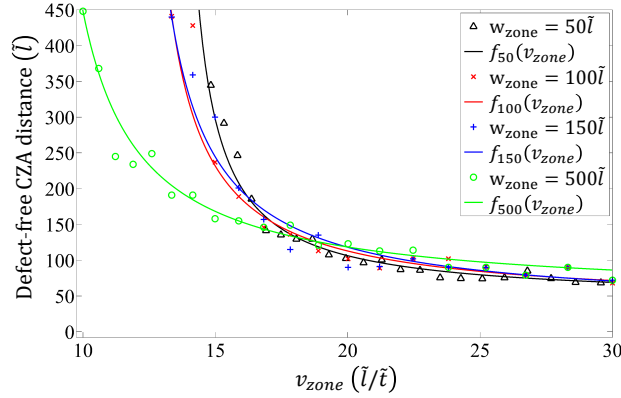

Figure 5.10: Comparison of defect-free CZA distance for varying zone widths. Data for each zone width is fit to Eqn. (5.9) and results are shown. As zone width increases, the asymptotic CZA velocity decreases. Resultant constants for each fit: For $w_{zone} = 100$; $a_{100} = 37.94$, $b_{100} = 162.2$, $c_{100} = -11.84$, $R^2_{100} = 0.9751$. For $w_{zone} = 150$; $a_{150} = 31.09$, $b_{150} = 376.3$, $c_{150} = -11.55$, $R^2_{150} = 0.9587$. For $w_{zone} = 500$; $a_{500} = 47.13$, $b_{500} = 498.2$, $c_{500} = -7.836$, $R^2_{500} = 0.9684$

78

5.5 Conclusions

In conclusion, we have implemented a temperature-dependent optimized phase-field model which has been tailored to simulate PS-b-PMMA block copolymers. The behaviors of sphere-forming PS-b-PMMA have been explored and we have found synergy between cold-zone annealing and chemoepitaxial templating such that the propagation of surface patterns, initially formed via minimal templating, is possible with the application of low-velocity cold-zone annealing. This propagation is possible over long distances. Applicable zone velocities to this method are dependent on the temperature gradient that is implemented.

Bibliography

[1] Gang Chen, Kyle J Gibson, Di Liu, Huw C Rees, Jung-Hoon Lee, Weiwei Xia, Ruoqian Lin, Huolin L Xin, Oleg Gang, and Yossi Weizmann. Regioselective surface encoding of nanoparticles for programmable self-assembly. *Nature Materials*, 18(2):169, 2019.

[2] Yin Ning, Lijuan Han, Matthew J Derry, Fiona C Meldrum, and Steven P Armes. Model anionic block copolymer vesicles provide important design rules for efficient nanoparticle occlusion within calcite. *Journal of the American Chemical Society*, 141(6):2557–2567, 2019.

[3] Bart Stel, Ilja Gunkel, Xiaodan Gu, Thomas P Russell, James J De Yoreo, and Magalí Lingenfelder. Contrasting chemistry of block copolymer films controls the dynamics of protein self-assembly at the nanoscale. *ACS Nano*, 13(4):4018–4027, 2019.

[4] Daniel H Yi, Chang-Yong Nam, Gregory S Doerk, Charles T Black, and Robert B Grubbs. Infiltration synthesis of diverse metal oxide nanostructures from epoxidized diene–styrene block copolymer templates. *ACS Applied Polymer Materials*, 1(4):672–683, 2019.

[5] Kuo Zhang, Hui-Min Gao, Duo Xu, and Zhong-Yuan Lu. Tethering solvophilic blocks to the ends of polymer brushes: an effective method for adjusting surface patterns. *Soft Matter*, 15(5):890–900, 2019.

[6] Hongbo Feng, Xinyi Lu, Weiyu Wang, Nam-Goo Kang, and Jimmy Mays. Block copolymers: Synthesis, self-assembly, and applications. *Polymers*, 9(10):494, 2017.

[7] Shengxiang Ji, Lei Wan, Chi-Chun Liu, and Paul F Nealey. Directed self-assembly of block copolymers on chemical patterns: A platform for nanofabrication. *Progress in Polymer Science*, 54:76–127, 2016.

[8] Mark Neisser. Patterning roadmap: 2017 prospects. *Advanced Optical Technologies*, 6 (3-4):143–148, 2017.

[9] Jouni Ahopelto, Gustavo Ardila, Livio Baldi, Francis Balestra, Didier Belot, Gíorgos Fagas, Stefan De Gendt, Danilo Demarchi, Montserrat Fernandez-Bolaños, David Holden, et al. Nanoelectronics roadmap for europe: From nanodevices and innovative materials to system integration. *Solid-State Electronics*, 155:7–19, 2019.

[10] Ming Luo and Thomas H Epps III. Directed block copolymer thin film self-assembly: emerging trends in nanopattern fabrication. *Macromolecules*, 46(19):7567–7579, 2013.

[11] Hanqiong Hu, Manesh Gopinadhan, and Chinedum O Osuji. Directed self-assembly of block copolymers: a tutorial review of strategies for enabling nanotechnology with soft matter. *Soft Matter*, 10(22):3867–3889, 2014.

[12] Craig J Hawker and Thomas P Russell. Block copolymer lithography: Merging "bottom-

up" with "top-down" processes. *MRS Bulletin*, 30(12):952–966, 2005.

[13] Fong Liu and Nigel Goldenfeld. Dynamics of phase separation in block copolymer melts. *Physical Review A*, 39(9):4805, 1989.

[14] Glenn C Paquette. Front propagation in a diblock copolymer melt. *Physical Review A*, 44(10):6577, 1991.

[15] Hiroshi Furukawa. Phase separation by directional quenching and morphological transition. *Physica A: Statistical Mechanics and its Applications*, 180(1-2):128–155, 1992.

[16] Hongdong Zhang, Jianwen Zhang, Yuliang Yang, and Xuedong Zhou. Microphase separation of diblock copolymer induced by directional quenching. *The Journal of Chemical Physics*, 106(2):784–792, 1997.

[17] Takeji Hashimoto, Jeffrey Bodycomb, Yoshinori Funaki, and Kohtaro Kimishima. The effect of temperature gradient on the microdomain orientation of diblock copolymers undergoing an order- disorder transition. *Macromolecules*, 32(3):952–954, 1999.

[18] Brian C Berry, August W Bosse, Jack F Douglas, Ronald L Jones, and Alamgir Karim. Orientational order in block copolymer films zone annealed below the order- disorder transition temperature. *Nano Letters*, 7(9):2789–2794, 2007.

[19] Kevin G Yager, Nathaniel J Fredin, Xiaohua Zhang, Brian C Berry, Alamgir Karim, and Ronald L Jones. Evolution of block-copolymer order through a moving thermal zone. *Soft Matter*, 6(1):92–99, 2010.

[20] Gurpreet Singh, Kevin G Yager, Detlef-M Smilgies, Manish M Kulkarni, David G Bucknall, and Alamgir Karim. Tuning molecular relaxation for vertical orientation in cylindrical block copolymer films via sharp dynamic zone annealing. *Macromolecules*, 45 (17):7107–7117, 2012.

[21] Changhuai Ye, Yan Sun, Alamgir Karim, and Bryan D Vogt. Extending dynamic range of block copolymer ordering with rotational cold zone annealing (rcza) and ionic liquids. *Macromolecules*, 48(20):7567–7573, 2015.

[22] August W Bosse, Jack F Douglas, Brian C Berry, Ronald L Jones, and Alamgir Karim. Block-copolymer ordering with a spatiotemporally heterogeneous mobility. *Physical Review Letters*, 99(21):216101, 2007.

[23] Zhinan Cong, Liangshun Zhang, Liquan Wang, and Jiaping Lin. Understanding the ordering mechanisms of self-assembled nanostructures of block copolymers during zone annealing. *The Journal of Chemical Physics*, 144(11):114901, 2016.

[24] Xiaomin Wan, Tong Gao, Liangshun Zhang, and Jiaping Lin. Ordering kinetics of lamella-forming block copolymers under the guidance of various external fields studied by dynamic self-consistent field theory. *Physical Chemistry Chemical Physics*, 19(9):

6707–6720, 2017.

[25] Joseph D Hill and Paul C Millett. Numerical simulations of directed self-assembly in diblock copolymer films using zone annealing and pattern templating. *Scientific Reports*, 7(1):5250, 2017.

[26] Liangshun Zhang, Lingling Liu, and Jiaping Lin. Well-ordered self-assembled nanostructures of block copolymer films via synergistic integration of chemoepitaxy and zone annealing. *Physical Chemistry Chemical Physics*, 20(1):498–508, 2018.

[27] Pawel W Majewski and Kevin G Yager. Millisecond ordering of block copolymer films via photothermal gradients. *ACS Nano*, 9(4):3896–3906, 2015.

[28] Daeseong Yong, Hyeong Min Jin, Sang Ouk Kim, and Jaeup U Kim. Laser-directed self-assembly of highly aligned lamellar and cylindrical block copolymer nanostructures: Experiment and simulation. *Macromolecules*, 51(4):1418–1426, 2018.

[29] Chuanbing Tang, Adam Tracz, Michal Kruk, Rui Zhang, Detlef-M Smilgies, Krzysztof Matyjaszewski, and Tomasz Kowalewski. Long-range ordered thin films of block copolymers prepared by zone-casting and their thermal conversion into ordered nanostructured carbon. *Journal of the American Chemical Society*, 127(19):6918–6919, 2005.

[30] Chuanbing Tang, Wei Wu, Detlef-M Smilgies, Krzysztof Matyjaszewski, and Tomasz Kowalewski. Robust control of microdomain orientation in thin films of block copolymers by zone casting. *Journal of the American Chemical Society*, 133(30):11802–11809, 2011.

[31] Claudio De Rosa, Cheolmin Park, Edwin L Thomas, and Bernard Lotz. Microdomain patterns from directional eutectic solidification and epitaxy. *Nature*, 405(6785):433, 2000.

[32] Seung Hyun Kim, Matthew J Misner, TING Xu, Masahiro Kimura, and Thomas P Russell. Highly oriented and ordered arrays from block copolymers via solvent evaporation. *Advanced Materials*, 16(3):226–231, 2004.

[33] Takehiro Seshimo, Rina Maeda, Rin Odashima, Yutaka Takenaka, Daisuke Kawana, Katsumi Ohmori, and Teruaki Hayakawa. Perpendicularly oriented sub-10-nm block copolymer lamellae by atmospheric thermal annealing for one minute. *Scientific Reports*, 6:19481, 2016.

[34] Gunnar Nelson, Chloe Drapes, Meagan Grant, Ryan Gnabasik, Jeffrey Wong, and Andrew Baruth. High-precision solvent vapor annealing for block copolymer thin films. *Micromachines*, 9(6):271, 2018.

[35] Gurpreet Singh, Kevin G Yager, Brian Berry, Ho-Cheol Kim, and Alamgir Karim. Dynamic thermal field-induced gradient soft-shear for highly oriented block copolymer thin films. *Acs Nano*, 6(11):10335–10342, 2012.

[36] Sang Ouk Kim, Harun H Solak, Mark P Stoykovich, Nicola J Ferrier, Juan J de Pablo, and Paul F Nealey. Epitaxial self-assembly of block copolymers on lithographically defined nanopatterned substrates. *Nature*, 424(6947):411, 2003.

[37] Joy Y Cheng, Caroline A Ross, Henry I Smith, and Edwin L Thomas. Templated self-assembly of block copolymers: top-down helps bottom-up. *Advanced Materials*, 18(19): 2505–2521, 2006.

[38] Seong-Jun Jeong, Hyoung-Seok Moon, Bong Hoon Kim, Ju Young Kim, Jaeho Yu, Sumi Lee, Moon Gyu Lee, HwanYoung Choi, and Sang Ouk Kim. Ultralarge-area block copolymer lithography enabled by disposable photoresist prepatterning. *ACS Nano*, 4 (9):5181–5186, 2010.

[39] Gregory S Doerk, Chi-Chun Liu, Joy Y Cheng, Charles T Rettner, Jed W Pitera, Leslie E Krupp, Teya Topuria, Noel Arellano, and Daniel P Sanders. Pattern placement accuracy in block copolymer directed self-assembly based on chemical epitaxy. *ACS Nano*, 7(1):276–285, 2012.

[40] Roel Gronheid, Jan Doise, Joost Bekaert, Boon Teik Chan, Ioannis Karageorgos, Julien Ryckaert, Geert Vandenberghe, Yi Cao, Guanyang Lin, Mark Somervell, et al. Implementation of templated dsa for via layer patterning at the 7nm node. In *Alternative Lithographic Technologies VII*, volume 9423, page 942305. International Society for Optics and Photonics, 2015.

[41] Gregory Blachut, Stephen M Sirard, Michael J Maher, Yusuke Asano, Yasunobu Someya, Austin P Lane, William J Durand, Christopher M Bates, Andrew M Dinhobl, Roel Gronheid, et al. A hybrid chemo-/grapho-epitaxial alignment strategy for defect reduction in sub-10 nm directed self-assembly of silicon-containing block copolymers. *Chemistry of Materials*, 28(24):8951–8961, 2016.

[42] Jaewon Choi, Yinyong Li, Paul Y Kim, Feng Liu, Hyeyoung Kim, Duk Man Yu, June Huh, Kenneth R Carter, and Thomas P Russell. Orthogonally aligned block copolymer line patterns on minimal topographic patterns. *ACS Applied Materials & Interfaces*, 10 (9):8324–8332, 2018.

[43] Ilja Gunkel. Directing block copolymer self-assembly on patterned substrates. *Small*, 14(46):1802872, 2018.

[44] Brian C Berry, Gurpreet Singh, Ho-Cheol Kim, and Alamgir Karim. Highly aligned block copolymer thin films by synergistic coupling of static graphoepitaxy and dynamic thermal annealing fields. *ACS Macro Letters*, 2(4):346–350, 2013.

[45] Jiachen Xue, Gurpreet Singh, Zhe Qiang, Alamgir Karim, and Bryan D Vogt. Unidirectional self-assembly of soft templated mesoporous carbons by zone annealing. *Nanoscale*, 5(17):7928–7935, 2013.

[46] Jimmy V Liu, Carlos J García-Cervera, Kris T Delaney, and Glenn H Fredrickson. Optimized phase field model for diblock copolymer melts. *Macromolecules*, 52(7):2878–2888, 2019.

[47] Takao Ohta and Kyozi Kawasaki. Equilibrium morphology of block copolymer melts. *Macromolecules*, 19(10):2621–2632, 1986.

[48] Takeji Hashimoto. Time-dependent ginzburg-landau approach for microphase-separation kinetics of block polymers. *Macromolecules*, 20(2):465–468, 1987.

[49] GJA Sevink and Andrei V Zvelindovsky. Block copolymers confined in a nanopore: Pathfinding in a curving and frustrating flatland. *The Journal of Chemical Physics*, 128 (8):084901, 2008.

[50] Paul C Millett. Time-dependent ginzburg-landau model for nonfrustrated linear a b c triblock terpolymers. *Physical Review E*, 92(2):022602, 2015.

[51] François Drolet and Glenn H Fredrickson. Combinatorial screening of complex block copolymer assembly with self-consistent field theory. *Physical Review Letters*, 83(21): 4317, 1999.

[52] Yuliang Yang, Feng Qiu, Ping Tang, and Hongdong Zhang. Applications of self-consistent field theory in polymer systems. *Science in China Series B*, 49(1):21–43, 2006.

[53] Jimmy Liu, Kris T Delaney, and Glenn H Fredrickson. Phase field mapping for accurate, ultrafast simulations of directed self-assembly. In *Advances in Patterning Materials and Processes XXXIII*, volume 9779, page 977920. International Society for Optics and Photonics, 2016.

[54] Jimmy Liu, Kris T Delaney, and Glenn H Fredrickson. Optimized phase field models in confinement: fast and accurate simulations of directed self-assembly. In *Advances in Patterning Materials and Processes XXXIV*, volume 10146, page 101460Z. International Society for Optics and Photonics, 2017.

[55] Maria Serral, Marco Pinna, Andrei V Zvelindovsky, Josep Bonet Avalos, et al. Cell dynamics simulations of sphere-forming diblock copolymers in thin films on chemically patterned substrates. *Macromolecules*, 49(3):1079–1092, 2016.

[56] Craig R Bartels, Buckley Crist, and William W Graessley. Self-diffusion coefficient in melts of linear polymers: chain length and temperature dependence for hydrogenated polybutadiene. *Macromolecules*, 17(12):2702–2708, 1984.

[57] Masao Doi and Samuel Frederick Edwards. *The theory of polymer dynamics*, volume 73. Oxford University Press, 1988.

[58] Karim R Gadelrab, Yi Ding, Ricardo Pablo-Pedro, Hsieh Chen, Kevin W Gotrik,

David G Tempel, Caroline A Ross, and Alfredo Alexander-Katz. Limits of directed self-assembly in block copolymers. *Nano Letters*, 18(6):3766–3772, 2018.

[59] Thomas P Russell, Rex P Hjelm Jr, and Phil A Seeger. Temperature dependence of the interaction parameter of polystyrene and poly (methyl methacrylate). *Macromolecules*, 23(3):890–893, 1990.

[60] Der-Tsai Lee and Arthur K Lin. Generalized delaunay triangulation for planar graphs. *Discrete & Computational Geometry*, 1(3):201–217, 1986.

Chapter 6

Conclusion

The objective of this dissertation is to numerically study and predict the behaviors of linear diblock copolymer systems using large scale numerical modeling and to enhance the scientific knowledge within the field. Multiple phase field methods have been used to simulate these systems. Directed self-assembly techniques implemented within the simulations predicted the enhanced behavior of these copolymer systems under various conditions. Post-processing analysis algorithms have been developed and applied to simulation results in order to quantify defect density and long range ordering within processed results. Orientation analysis of the evolved BCP structure is used as a metric to present these results qualitatively. The specific research objectives of this dissertation have been met and are presented in this work.

6.1 Conclusions

For generic block co-polymers that spontaneously phase-separate to form lamellar structures, the presented simulations in Chapter 4 agree with published works in showing that cold-zone annealing can enhance the long-range ordering of the structure by inducing linear orientation to the self-assembled formation. Also shown is that the direction of orientation corresponds with the velocity that cold-zone annealing is performed at, further agreeing with published experimental works. For very low velocities, the preferential orientation of the lamellar structures are perpendicular to the direction of zone velocity. As velocity is systematically increases, there is a narrow range of velocities where the preferential orientation shifts to being parallel to the direction of zone velocity. Above this range of velocities, orientation becomes disordered. Predisposing the preferential phase-separation at the lower substrate via the application of epitaxial templating to this process can further enhance the orientation and allow for a higher range of velocities where ideal lamellar formation occurs. For template spacing as small as five lamellar distances, the preferential alignment can be

strong enough that grain boundaries evolve such that templated and untemplated grains orient perpendicular to one another.

A material specific study of sphere forming PS-b-PMMA diblock copolymer in Chapter 5 has been completed. This study shows the behavior of sphere-forming thin-film PS-b-PMMA with the application of chemoepitaxial templating. It was shown that the rate at which highly-ordered structures form is dependent on the density of templated points and the architecture of those points on a 2-D surface. With the application of cold-zone annealing under the prescribed conditions, it has been shown that the initial order established in a narrow, templated region can self-propagate through untemplated regions as the moving thermal gradient sweeps across the film at a constant velocity. The relative distance of self-propagation appears to be inversely proportional to the velocity of the thermal zone.

6.2 Novel Contributions and Future Work

The numerical modeling of diblock copolymers presented in this dissertation have shown results which have yet to be tested experimentally. Experimental verification of the results presented in Chapter 5 could help establish the basis for a new method of creating long-range regular surface patterns. As of the time of publishing, there has been no experiment work on the application of Cold-Zone Annealing with Sphere forming diblock copolymers.

The Optimized Phase Field method used in Chapter 5 has proven to be an excellent tool for modeling block copolymers, however, there are some drawbacks where the model could be improved. Because the model is able to calculate χ based on material specific properties, it may be possible and relevant to incorporate other material properties such as molecular weight and thermal expansion into the model as well.

Areas for additional future research include identifying more viable templating patterns, inclusion of additional directed self-assembly techniques, application of the developed OPF model on additional specific materials, studies of cylinder and lamella forming block copolymer systems, and application of non-linear zone annealing. These are just a scratch on the surface of possible promising research directions which could be built on top of the established

computational model.

Appendix

Supplemental Information for Paper 1: Numerical Simulations of Directed Self-Assembly in Diblock Copolymer Films using Zone Annealing and Pattern Templating

Region Assessment

The transitions between regions are determined by considering the velocities where mean data crosses a horizontal line drawn at 97% orientation via linear interpolation between data points. In transitions from Region I to Region II and Region III to Region IV where the mean orientation transitions from above to below the threshold, the earliest transitions are selected to determine region boundaries where multiple transitions occur as a result of fluctuations in the data. In transitions from Region II to Region III, the last transition is selected. This method of determining boundaries minimizes the areas of Regions I and III and ensures that they only contain velocities where the mean is above the required threshold. Figure S1 depicts the transition velocities for data collected using a zone width of 160 $\tilde{l}$ where both instances described above occur. Shaded areas on Fig. 1 represent the standard error of the mean for the corresponding orientation data.

Transition Velocity as a Function of Zone Width

Figures 2 and 3 show parallel and perpendicular orientation data, respectively, for each zone width considered in this work, for the untemplated simulations. The alignment threshold (97% alignment) is marked with a horizontal dashed line. Vertical dashed lines corresponding to the same color of the data depict calculated transition velocities. In Fig. 2, arrows depict the area corresponding to Region I (note that for $w_{zone} = 1000\ \tilde{l}$, Region I does not present for the range of velocities simulated). In Fig. 3, double-headed arrows indicate the range of velocities associated with Region III. Each of these calculated boundary values are shown in Fig. 8 of the article.
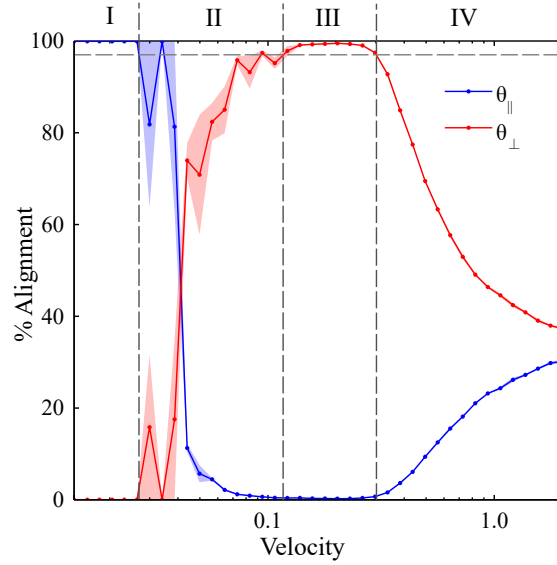
Figure 1: Orientation data for $w_{zone} = 160\ \tilde{l}$ with untemplated domains. The threshold alignment and transition velocities are marked with dashed lines.
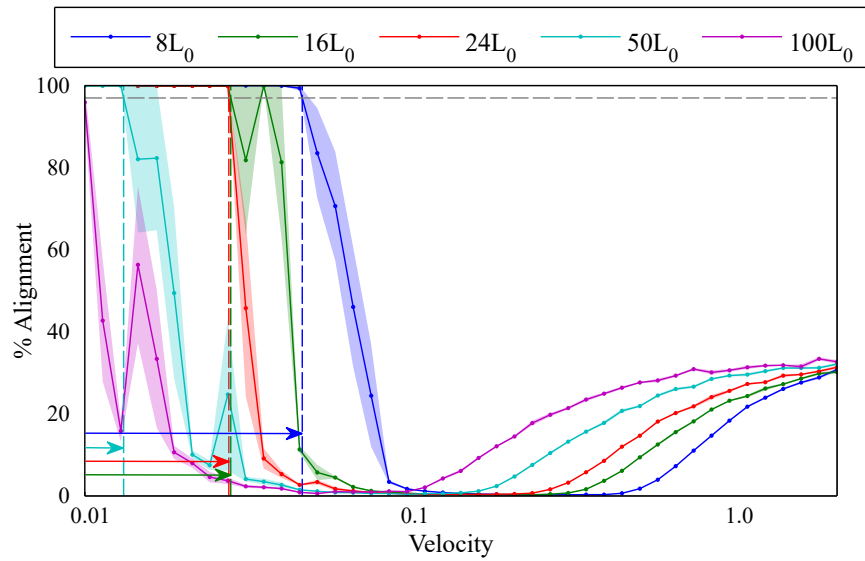

Figure 2: Parallel orientation data for tested values of w_{zone}. Dashed lines depict threshold alignment (grey) and transition velocities (colors correspond to w_{zone} data). Region I is depicted with arrows.
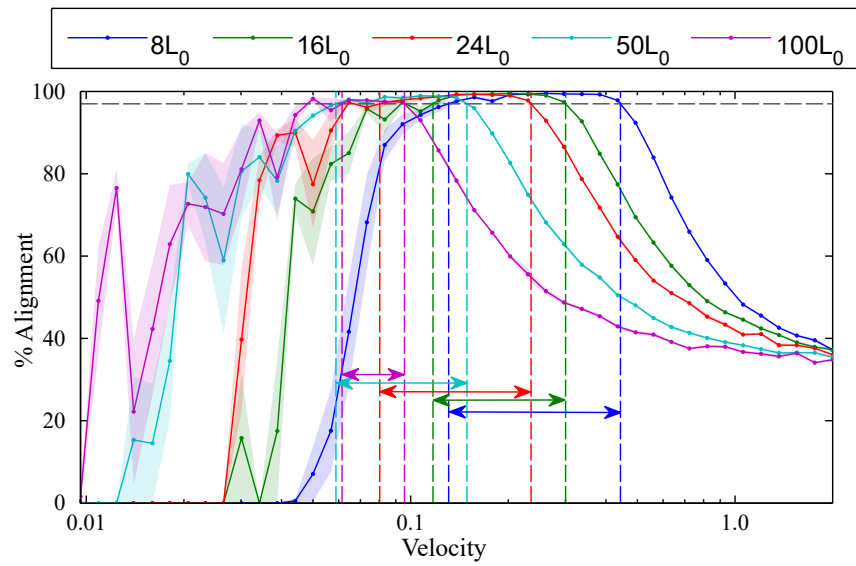
Figure 3: Perpendicular orientation data for tested values of w_{zone}. Dashed lines depict threshold alignment (grey) and transition velocities (colors correspond to w_{zone} data). Region III is depicted with double-headed arrows.